Characterization of the Interior Structure of Ganymede

Through Joint Bayesian Inversion of Gravity, Magnetic Induction, Tidal and Libration Observations

Alessandra Marzolini

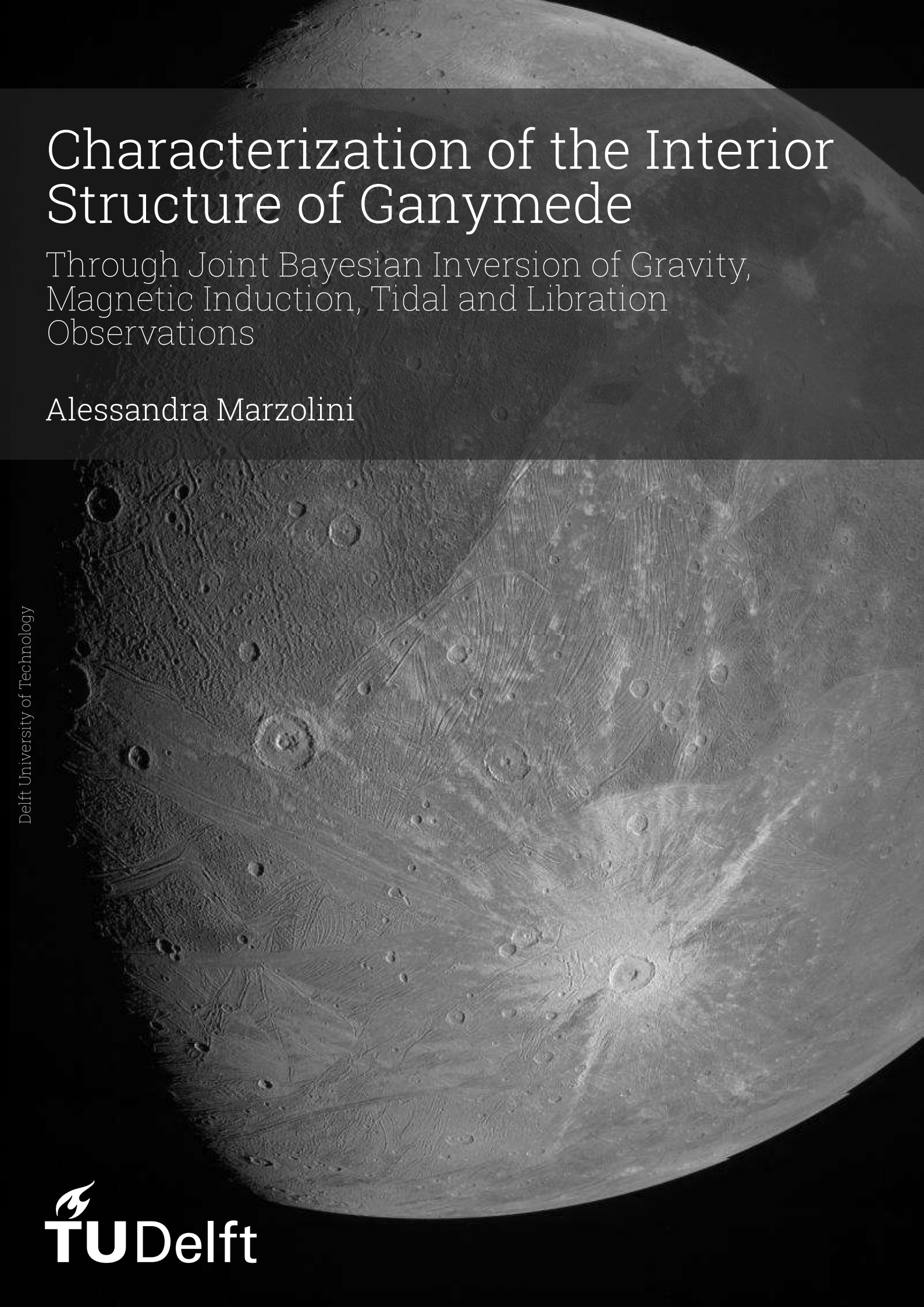

Delft University of Technology

TU Delft

Characterization of the Interior Structure of Ganymede

Through Joint Bayesian Inversion of Gravity, Magnetic Induction, Tidal and Libration Observations

by

Alessandra Marzolini

to obtain the degree of Master of Science
at the Delft University of Technology,
to be defended publicly on October 9, 2025.

Student number:	5938716	
Project duration:	January 20, 2025 – October 9, 2025	
Thesis supervisor:	Dr. ir. M. Rovira-Navarro,	TU Delft
Committee chair:	Dr. ir. W. van der Wal,	TU Delft
Committee external:	Dr. ir. D. Dirkx,	TU Delft

Cover: https://photojournal.jpl.nasa.gov/catalog/PIA24681

TU Delft

Preface

I have been staring at this blank page for the past week, promising myself I would not wait until the night before the deadline to write it. And yet, here I am, on the night before the deadline, trying to capture the learning, the growth, and the emotions of this extraordinary journey in just a few paragraphs.

This work marks an important milestone: the end of my student era and the beginning of adulthood. It may sound dramatic, but until today, I have more or less followed the path I was expected to take: be a good student, earn a bachelor's degree with high grades, begin a master's program and prepare for a future career. This is the point where that path ends, and where I can finally choose what the future will look like. And that is terrifying because, despite all the learning I have done inside and outside the classroom in these past twenty-four years, I have realized I will never truly feel ready for such big responsibilities. I have carried this feeling with me for a long time now, trying to convince myself that I was prepared. But eventually I had to accept that I was not, that I never will be, and that this is okay.

If there is one thing I have learned through this master's program and thesis project, it is that you never feel ready to take on the difficult challenge, to embark on the big project, to face the obstacle you've been avoiding. And yet, here you are, doing it anyway at the best of your abilities. You do not need to feel ready, you just do it. Because, as one of my favorite quotes always reminds me, *the only way out is through.* And before you know it, it is over, and you look back and think: "Wow, we made it".

I say *we*, not *I*, because no one takes on this journey alone. There are the people who sit beside us every day, carrying part of our weight when it feels too heavy; the people who live far away, yet feel as if they were right next to us; the people you rarely talk to, but who will always be there when you need them. There are those who shared a part of the journey and then left, as it was meant to be; those who would have loved to see this moment but cannot; and even those with whom things did not click, but who still taught you valuable lessons. There are also the people of the future – the ones I hope will stay forever, the ones who will slowly find their way into my life, the ones who will make me feel at home even when I am not, the ones who will surprise me unexpectedly.

To all of these people, I am deeply grateful. In their own ways, at their own times, they supported me through this journey, and I know they will continue to support me in whatever lies ahead.

Finally, I want to thank the long-braided little girl who used to sit on the balcony with her grandfather, inventing stories about planets and stars, for not getting lost in the seriousness of life. I want to thank the girl who faced the challenges of these past two years, for standing her ground and growing through them. And I want to thank the woman she will become, for never giving up on her dreams, whatever shape they might take.

Alessandra Marzolini
Delft, September 2025

Acknowledgments

I would first like to express my deepest gratitude to my family, whose constant love and support have brought me to this point. Without them, this journey would not have been possible.

I am grateful to my supervisor, Marc. Thank you for your guidance throughout these eight months, for our many insightful conversations, and for the passion, time, and energy you dedicated to this project. Your ability to always push me to go a little further, even when I felt I had reached the end, and your encouragement to present this work at the EPSC–DPS Joint Meeting 2025 truly enriched both this thesis and my personal growth.

I would also like to thank the Justus & Louise van Effen Excellence Scholarships, which made it possible for me to finance my Master's program. Their generous support not only enabled my studies but also gave me the freedom to fully dedicate myself to this experience.

Finally, I would like to thank Lars and Mattia, for your constant support both in the long days and late nights, for challenging me in every assignment, and for offering advice whenever I needed it. I learned so much from you, and I am grateful to have shared this journey together.

Alessandra Marzolini
Delft, September 2025

Summary

This thesis presents a comprehensive methodology to characterize the interior structure of Ganymede, Jupiter's largest moon, through a joint Bayesian inversion framework that integrates gravity, magnetic induction, tidal, and libration observations. The motivation behind this work comes from the increasing scientific interest in icy moons, which offer insights into the origins and potential habitability of the Solar System. These celestial bodies, such as Europa, Enceladus, and Ganymede, are characterized by vast subsurface oceans beneath their icy crusts, making them prime candidates for hosting life beyond Earth. In particular, Ganymede stands out as the largest moon in the Solar System and the only one known to possess its own intrinsic magnetic field. It is also believed to host a subsurface ocean beneath its icy crust, making it an interesting target for scientific exploration. Despite these findings, much about Ganymede's internal structure is still unknown. The upcoming ESA's Juice mission will carry out detailed observations of the moon through a series of flybys followed by an extended orbital tour, delivering high-precision data that will help constrain Ganymede's structure and improve our understanding of its interior.

This work addresses the challenge of constraining Ganymede's interior structure using multiple datasets – gravity, magnetic induction, tidal, and libration observations – each sensitive to different interior parameters and affected by parameter degeneracies. To tackle this, we first perform a global sensitivity analysis to understand how each observation relates to specific interior parameters. We then carry out a Bayesian inversion to combine the datasets into a single probabilistic model. Our analysis is based on a five-layer spherical model of Ganymede, consisting of a metallic core, a silicate mantle, a high-pressure ice layer, a liquid salty ocean, and an outer ice shell.

The sensitivity analysis reveals that magnetic induction is most sensitive to ocean thickness and composition, tidal displacement to the ice shell thickness and rigidity, and libration amplitude to shell rigidity. Degeneracies also become evident: for instance, the interplay between shell thickness, ocean density, and shear modulus makes it challenging to constrain all three parameters using tidal observations alone. However, other observables may help resolve these ambiguities. For example, libration data can better constrain the shell's shear modulus, while magnetic measurements can inform ocean thickness. This highlights the need for a joint inversion approach.

The Bayesian inversion is performed in successive steps, progressively incorporating additional observations. We begin with a simple inversion using Ganymede's moment of inertia as the only observable, which provides constraints on the core and mantle parameters, but leaves the hydrosphere parameters largely unconstrained. Next, we include magnetic induction data, which significantly improves the constraints on the ice shell and ocean thicknesses, and, to a lesser extent, on the ocean density. Adding the real part of the tidal Love number k_2 further refines the estimates of the ice shell and ocean densities, allowing to infer the ocean composition. It also provides constraints on the rigidity of the high-pressure ice and the compressibility of the layers. Finally, the inversion moment of inertia, magnetic induction amplitude and both the real and imaginary parts of k_2 provides additional constraints on the viscosities of the ice layers, related to the tidal dissipation within Ganymede.

Beyond advancing our understanding of Ganymede, this study demonstrates the effectiveness of joint Bayesian inference for the characterization of planetary interior. This framework contributes to the scientific preparation for the ESA's Juice mission, identifies the most critical measurements to break degeneracies in interior model parameters, and can be extended to other icy moons, such as Europa and Enceladus, where spacecraft data will provide similar observational constraints.

Contents

Nomenclature

List of Abbreviations

3GM Gravity and Geophysics of Jupiter and Galilean Moons
DE Differential Evolution
DSN Deep Space Network
ECSS European Cooperation for Space Standardization
EOS Equation-Of-State
ESA European Space Agency
GALA Ganymede Laser Altimeter
GRAIL Gravity Recovery and Interior Laboratory
HP High-pressure
J-MAG Juice magnetometer
Juice Jupiter Icy moons Explorer
LLR Lunar Laser Ranging
LOLA Lunar Orbiter Laser Altimeter
M-H Metropolis-Hastings
MC Monte Carlo
MCMC Markov-chain Monte Carlo
MoI Moment of Inertia
NASA National Aeronautics and Space Administration
OAT One-at-a-time
PRIDE Planetary Radio Interferometer and Doppler Experiment
RADEM Radiation monitor
RIME Radar for Icy Moon Exploration
WBS Work Breakdown Structure

List of Symbols

Notation	Description	Unit
e	Eccentricity	–
g	Gravitational acceleration	$\mathrm{m\,s^{-2}}$
h	Radial Love number of degree n (h_n)	–
i	Inclination	rad
j	Spherical Bessel functions of first kind	–
k	Gravitational Love number of degree n (k_n)	–
k_f	Fluid Love number	–
l	Poloidal Love number of degree n (l_n)	–
m	Order	–
n	Degree	–
p	Pressure	Pa
q_r	Rotational parameter	–
q_t	Tidal parameter	–
r	Radial distance	m
wt	Weight percent	%
y	Spherical Bessel functions of second kind	–
A	Normalized magnetic induction amplitude	–
$\bar{A}$	Equatorial moment of inertia (x axis)	$\mathrm{kg\,m^{-2}}$
A^e	Normalized complex magnetic induction response	–
B	Magnetic field	T
$\bar{B}$	Equatorial moment of inertia (y axis)	$\mathrm{kg\,m^{-2}}$
C	Unnormalized quadrupole field coefficient of degree n and order m (C_{nm})	–
D	Thickness	m
DEC	Declination	rad
$\bar{I}$	Polar moment of inertia	$\mathrm{kg\,m^{-2}}$
I/MR^2	Moment of inertia factor	–
J_2	Unnormalized quadrupole field coefficient ($-C_{20}$)	–
K	Bulk modulus	Pa
M	Mass	kg
$\bar{M}$	Model	–
P	Associated Legendre polynomial of degree n and order m (P_{nm})	–
P_o	Orbital period	s
Q	Quality factor	–
R	Equatorial radius	m
RA	Right ascension	rad
S	Unnormalized quadrupole field coefficient of degree n and order m (S_{nm})	–
T	Temperature	K
X	Model parameters	–
η	Viscosity	$\mathrm{Pa\,s}$
θ	Angular frequency of the oscillation of the driving field	$\mathrm{s^{-1}}$
κ	Electrical conductivity	$\mathrm{S\,m^{-1}}$
λ	Longitude	rad
μ_s	Shear modulus	Pa
ν	Phase lag	rad
ρ	Density	$\mathrm{kg\,m^{-3}}$
$\bar{\rho}$	Mean density	$\mathrm{kg\,m^{-3}}$
σ	Uncertainty	–
τ	Autocorrelation time	–

Notation	Description	Unit
υ	Poisson's ratio	–
ϕ	Latitude	rad
ψ	Obliquity	rad
ω	Rotation rate, Orbital frequency	$\mathrm{rad\,s^{-1}}$
Θ	Observed data	–
Φ	Gravitational potential	$\mathrm{m^2\,s^{-2}}$
Φ^T	Tidal potential	$\mathrm{m^2\,s^{-2}}$
Ψ	Libration amplitude	m

List of Constants

Notation	Description	Quantity
G	Universal gravitational constant	$6.672\,59 \times 10^{-11}\,\mathrm{m^3\,kg^{-1}\,s^{-2}}$
μ_0	Magnetic permeability in vacuum	$4\pi \times 10^{-7}\,\mathrm{N\,A^{-2}}$
π	Pi number	3.141 59

List of Subscripts

Notation	Description
b	Bottom
c	Core
hp	High-pressure ice
ice	Ice shell
ma	Mantle
o	Ocean
surf	Surface
triple	Triple point
G	Ganymede

1

Introduction

Space missions to icy satellites are of great scientific significance, offering insights into the origins and potential habitability of our Solar System. These celestial bodies, such as Europa, Enceladus, and Ganymede, are characterized by vast subsurface oceans beneath their icy crusts, making them prime candidates for hosting life beyond Earth.

This project aims to develop a methodology to characterize the interior structure of icy moons, with a focus on Ganymede, through joint inversion of gravity, magnetic induction, tidal, and libration measurements. This chapter is outlined as follows: the relevance of the project is explained in section 1.1, followed by a description of the current knowledge of Ganymede in section 1.2. The Bayesian framework for the joint inversion of different data sets is introduced in section 1.3, and the research questions are formulated in section 1.4. The chapter concludes with section 1.5, which provides an overview of the report's structure.

1.1. Relevance of the Project

The current interest in studying icy moons is driven by the discovery that several of these bodies in the outer Solar System harbor subsurface water oceans. Observations from the Galileo and Cassini missions revealed evidence of liquid water beneath the icy shells of Europa, Ganymede, Callisto, Enceladus, and Titan, making them prime candidates for astrobiological studies (Nimmo et al., 2016).

Icy moons are considered potential habitats for life because their subsurface oceans may provide favorable conditions for habitability. Liquid water, together with energy and nutrients, is a key ingredient for life as we know it, and interactions between the ocean and the rocky mantle could supply essential chemical elements and energy sources for biological activity (Hand et al., 2020).

Recognizing the scientific potential of these worlds, space agencies have prioritized their exploration. The search for habitable environments and the study of planetary system dynamics are key themes in long-term strategic road maps, such as NASA's Decadal Survey, ESA's Cosmic Vision, and ESA's Voyage 2050 (European Space Agency, 2005; European Space Agency, 2021; National Academies of Sciences et al., 2023). The first two themes in ESA's Cosmic Vision are (European Space Agency, 2005):

1. *Theme 1: What are the conditions for planet formation and the emergence of life?*
2. *Theme 2: How does the Solar System work?*

This framework emphasizes the need for in-situ investigations of icy moons and their subsurface oceans to advance our understanding of planetary habitability and Solar System evolution. In line with these priorities, several missions are planned or already on the way to explore these moons in greater detail. NASA's Europa Clipper, launched in October 2024, will conduct a detailed exploration of Europa's ice shell and subsurface ocean. Similarly, ESA's Juice mission, launched in April 2023, will investigate

Ganymede, Europa, and Callisto to better understand their internal structure, composition, and potential habitability.

In the context of this project, the focus is on Ganymede, the largest moon in the Solar System, and the only one known to have its own magnetic field (Grasset et al., 2013). Not only does its magnetic environment interact with Jupiter's magnetosphere in complex ways (Grasset et al., 2013; Kivelson et al., 2002), but Ganymede is also expected to harbor a liquid ocean beneath its icy crust (Kivelson et al., 2002; Vance et al., 2014), which makes it an interesting target for scientific exploration.

Previous missions have already contributed significantly to our understanding of these complex worlds. In particular, the Galileo mission detected an induced magnetic field at Ganymede, suggesting the existence of a subsurface ocean beneath the icy crust (Kivelson et al., 2002). This evidence is supported by acquired images of Ganymede's surface (Pappalardo et al., 2004) and thermal modeling of its evolution (Grasset et al., 2013; Spohn et al., 2003). However, many aspects of Ganymede's interior composition and magnetic field still remain poorly understood, which motivates further investigation.

The upcoming Juice mission will conduct detailed observations of Ganymede through a series of flybys and an extended orbital tour (Grasset et al., 2013). Equipped with a suite of advanced instruments, Juice is expected to provide valuable constraints for theoretical models, significantly improving our understanding of the structure, composition, and magnetic field of the moon. As new data of unprecedented precision become available, more accurate modeling methodologies will be essential to further investigate Ganymede's interior structure and its magnetic interactions.

1.2. Ganymede

Ganymede is the third and largest moon of Jupiter and the largest satellite in the Solar System. With a radius of $R_{\mathrm{G}} = 2631.2 \pm 1.7$ km, Ganymede is larger than Mercury but has a significantly lower density, indicating a composition rich in water ice and silicate rock. It is the only known moon to possess a significant intrinsic magnetic field, suggesting a dynamo action occurring in a partially liquid metallic core.

Gravitational field measurements, particularly the determination of the gravitational parameter GM and the quadrupole moment J_2 from spacecraft flybys, have provided crucial insights into Ganymede's internal mass distribution. The moment of inertia derived from these observations, under the assumption of hydrostatic equilibrium, confirms that the moon is highly differentiated, with a dense core, a silicate mantle, and an outer hydrosphere composed of multiple ice phases and a liquid ocean (Anderson et al., 1996; Kivelson et al., 2002; Vance et al., 2014). Evidence for a subsurface ocean comes from the detection of an induced magnetic field and auroral oscillations in Ganymede's magnetosphere, consistent with the presence of a conductive liquid layer beneath the icy shell (Kivelson et al., 2002; Saur et al., 2015), as illustrated in Figure 1.1.

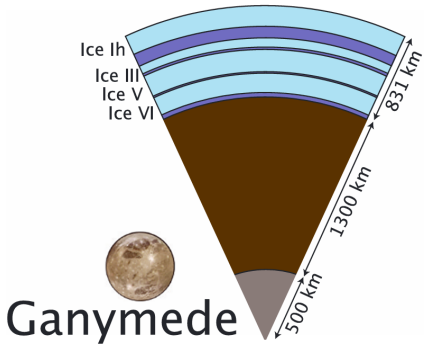

Figure 1.1: Schematic representation of Ganymede's interior model. Image credit: Vance et al. (2018, Figure 4).

1.2.1. Current View of Ganymede's Interior Structure

The understanding of Ganymede's interior structure has evolved significantly over the past several decades. From the analysis of gravitational data obtained with the Galileo mission, it was possible to infer a differentiated structure with a metallic core, a silicate mantle and an outer ice-liquid shell (Schubert et al., 2004). The detection of a magnetic field by the Galileo spacecraft supported the hypothesis of a subsurface ocean at a depth of about 150 km (Kivelson et al., 2002). Different models have been proposed to explain Ganymede's interior structure, from simple three-layer models (e. g., Anderson et al., 1996) to more complex ones, accounting for the presence of multiple ice phases and a liquid ocean (e. g., Vance et al., 2014).

Table 1.1 presents Ganymede's fundamental physical parameters, either measured or directly derived from spacecraft measurements, that are commonly used in studies to constrain interior structure models. Table 1.2 contains Ganymede's orbital parameters.

Table 1.1: Ganymede's physical parameters.

Symbol	Value	Uncertainty	Unit	Reference
M_G	1.48167	0.00020	10^{23} kg	Anderson et al. (1996)
I/MR^2	0.3115	0.0028	-	Schubert et al. (2004)
R_G	2631.2	1.7	km	Schubert et al. (2004)
$\bar{\rho}$	1942.0	4.8	$\mathrm{kg\,m^{-3}}$	Schubert et al. (2004)
J_2	127.53	2.9	10^{-6}	Schubert et al. (2004)

Table 1.2: Ganymede's orbital parameters. The values are taken from Rovira-Navarro et al. (2023).

P_o	e	i	ψ
7.16 d	$1.3e-3$	0.177°	0.033°

The lower moment of inertia factor for Ganymede compared to the other bodies in the Solar System suggests that the moon has a differentiated interior structure, with a stronger concentration of mass towards its center (Anderson et al., 1996). Comparison between the computed J_2 and calculations based on three-layer models suggests an essentially complete separation of ice, rock, and metal. This is supported by the detection of a magnetosphere and magnetic field at Ganymede, which implies the presence of a three-layer structure (Schubert et al., 2004; Schubert et al., 1996).

Anderson et al. (1996) used gravitational constraints to infer the internal structure of Ganymede. For the most likely three-layer structures, two analyses were performed for two different core densities: $5150\,\mathrm{kg\,m^{-3}}$ and $8000\,\mathrm{kg\,m^{-3}}$, corresponding to core compositions of Fe-FeS and pure Fe, respectively. The density of the silicate mantle was set to $3300\,\mathrm{kg\,m^{-3}}$. For a Fe-FeS core composition, the radius of the core could vary between $0.2R_G$ and $0.5R_G$, ice density ranged between $1000\,\mathrm{kg\,m^{-3}}$ and $1300\,\mathrm{kg\,m^{-3}}$, and the radius of the mantle-shell interface varied between $0.6R_G$ and $0.73R_G$ (Anderson et al., 1996). If an Fe core was considered, the ranges changed to $0.15R_G$ to $0.4R_G$ for the core radius, $0.53R_G$ to $0.73R_G$ for the mantle-shell interface, and 1000 to $1350\,\mathrm{kg\,m^{-3}}$ for the ice shell density (Anderson et al., 1996)

This study served as the foundation for future investigations, such as those of Sohl et al. (2002) and Schubert et al. (2004). After refining their analysis, they concluded that plausible core radii ranged from about $0.25R_G$ to $0.35R_G$, mantle thicknesses varied from 900 km to 1100 km, and that the ice shell, likely around 900 km thick, was further divided into phase transitions involving ice I, ice III, ice V, ice VI, and, most probably, a liquid ocean (Schubert et al., 2004; Sohl et al., 2002).

Vance et al. (2014) investigated the interior structure of Ganymede assuming a magnesium sulfate ocean with different concentrations and accounting for its thermodynamics, which allowed the authors to estimate the thickness of the ice shell, the ocean and the high pressure ice layers that form below the liquid layer. Their model assumed a core composition of Fe-FeS, with 25 $wt\%$ sulfur, and a liquid water containing $MgSO_4$. Assuming a spherical model with a surface temperature of $T_{surf} = 110\,\mathrm{K}$,

they calculated the density profiles and the corresponding depths of each ice layer from the equation of state of $MgSO_4$ and temperature profiles. By prescribing the density values of the core an mantle to $7030\,\mathrm{kg\,m^{-3}}$ and $3250\,\mathrm{kg\,m^{-3}}$ respectively, the total mass and moment of inertia were used to constrain the radii of the iron core and silicate mantle.

Different models were generated by varying the concentration of $MgSO_4$ and the bottom melting temperature of the ice I shell, leading to variations in the heat flux. The results showed the presence of a liquid ocean with thicknesses varying from 31 km to 753 km. The presence of high-pressure ice layers depends on both salinity and heat flux. For instance, the ice III phase forms only in models with low heat flow and salinity above 3 $wt\%$, whereas for higher salinity levels, ice III and VI phases may become buoyant. Total ice shell thicknesses (including the different ice phases and the liquid layer) ranged from 798 km to 1402 km, mantle thicknesses from 939 km to 1178 km, while core radii varied from 658 km to 799 km (Vance et al., 2014).

1.2.2. Magnetic Field

Ganymede is the only moon in the Solar System known to have its own magnetic field. Analysis of Galileo's radio emissions and plasma waves measurements suggests a strong intrinsic magnetic field (Gurnett et al., 1996; Kivelson et al., 1996) dominated by a dipole moment of 719 nT and tilted about 176° with respect to the rotation axis (Kivelson et al., 2002). Different scenarios can explain the presence of this magnetic field, such as dynamo action in a partially liquid core, a magneto-convection mechanism, or remanent magnetization.

Schubert et al. (1996) argued that the most likely explanation is dynamo action in a liquid or partially liquid metallic core. Remanent magnetization would imply the presence of a rock shell layer below the ice-rock interface. To obtain the required level of magnetization, the parameters that characterize this layer would exceed reasonable values. Dynamo action is more likely than magneto-convection because Ganymede's magnetic field is about six times larger than the ambient field caused by Jupiter. Since a magnetic field generated by magneto-convection would be of the same order of magnitude as the driving field and could not sustain without it, this mechanism is unlikely. Lastly, a dynamo action in a salty water ocean would require improbably large values of velocities, which leaves a liquid or partially liquid metallic core as the most probable explanation for Ganymede's permanent magnetic field (Schubert et al., 1996).

Kivelson et al. (2002) proposed two models to represent Ganymede's internal magnetic field. The first model included dipole and quadrupole components, while the second accounted for an induced magnetic dipole superimposed on the intrinsic dipole field. Although both models were consistent with the data acquired during multiple Galileo passes, Kivelson et al. (2002) favored the second, as it provided an equally good fit with fewer parameters. The presence of an induced dipole, reaching approximately 84 % of the theoretical maximum for a perfect conductor, suggests a conductive layer beneath the ice shell, likely a salty subsurface ocean within the first few hundred kilometers beneath the surface (Kivelson et al., 2002). Additionally, the weak quadrupole field implies that Ganymede's internal dynamo is deeply buried within its metallic core (Kivelson et al., 2002).

A recent study by Jia et al. (2024) presented an improved model of Ganymede's magnetic field by using magnetohydrodynamic simulations to subtract plasma and ionospheric current contributions from spacecraft measurements. Compared to the earlier analysis by Kivelson et al. (2002), they also incorporated data from two additional flybys of Ganymede – one by Galileo and one by Juno. Their refined analysis estimated an induction efficiency of $\sim 72\%$ (Jia et al., 2024), much lower than the value of 84% reported by Kivelson et al. (2002). This reduction could be explained by a deeper ocean, a lower ocean conductivity, or a combination of the two (Jia et al., 2024). However, since we were not aware of this updated estimate at the beginning of the project, we will use the older value in our analysis.

Studies of the moon's induction response, such as those of Vance et al. (2021), which will be further discussed in subsection 2.1.2, provide insight into ocean properties, including depth, conductivity, and composition. In this context, Ganymede's intrinsic magnetic field does not influence the induction response or the retrieval of ocean properties, as it remains static in its own reference frame and does not induce additional currents. Instead, it acts as a constant offset in magnetic field measurements. Therefore, given the significant scientific interest in the hydrosphere of icy moons and their properties, this work

will focus exclusively on modeling Ganymede's magnetic induction response, as further described in subsection 2.1.2.

The induced response is sensitive to the depth and conductivity of the ocean, as well as to the thickness of the overlying ice shell (Biersteker et al., 2023). Therefore, measurements at a single frequency can lead to degeneracies in interior parameters because they do not provide enough information to uniquely constrain the different properties of the interior. Continuous measurements of the magnetic field at multiple frequencies are thus required to investigate the liquid ocean layer and to constrain its thickness (Grasset et al., 2013).

The upcoming Juice mission will provide improved observations at multiple frequencies, allowing a more precise characterization of the induced response (Grasset et al., 2013). The Juice magnetometer (J-MAG) magnetometer on board Juice will measure the three-axis components of the magnetic field at frequencies ranging from 32 Hz to 128 Hz, enabling the characterization of Ganymede's magnetic field to an accuracy of less than 0.1 nT (European Space Agency, 2014). This approach will enable the study of both the regions near the moon and the boundaries of its magnetosphere.

1.2.3. Tides

Tidal forces cause a body to deform in response to gravitational interactions with other celestial bodies. Since no body is perfectly rigid, tides cause a distortion in the shape of the body, leading to the formation of tidal bulges. This process is not adiabatic and energy is dissipated as heat, driving the long-term evolution of planetary systems and influencing their internal structure, surface features, and orbital dynamics (Murray et al., 2000).

Ganymede experiences complex tidal effects as a result of Jupiter's gravitational influence and interactions with other moons. These tides can be divided into static and periodic tides. Static tidal bulges on Ganymede arise from the long-term forcing of Jupiter's gravitational pull, where the force is stronger on the side facing the planet and weaker on the opposite side, and they are characterized by the fluid Love number k_f. The resulting deformation aligns approximately with the axis connecting the two bodies, and its magnitude depends on the moon's interior properties, such as its density distribution (Murray et al., 2000).

The static tidal bulge generated by the planet not only deforms the satellite, but also alters its gravitational field. The deformation creates an asymmetry in the distribution of the moon's mass, which perturbs the gravitational potential. The non-central part of the potential can be expressed using spherical harmonics. In particular, the second-degree harmonic, linked to the quadrupole moment, is the primary contributor to the change in the moon's gravitational field due to the tidal bulge (Murray et al., 2000).

In contrast, periodic tides result from the short-term forcing of Jupiter on Ganymede caused by the relative motion of the satellite and planet. Ganymede's slightly eccentric orbit around Jupiter causes variations in the tidal forces it experiences throughout its orbit, while its inclination affects the symmetry of the tidal bulge relative to the equator. These periodic changes lead to oscillations in the tidal bulges and generate additional deformations that occur on much shorter timescales compared to the static tide. These time-dependent deformations continuously reshape the Ganymede's interior and surface, contributing to tidal heating and driving the long-term stability of the system (Murray et al., 2000).

Diurnal tides occur at the orbital frequency of Ganymede and they induce the largest deformations in the moon, which can be characterized by the potential and displacement Love numbers, respectively k_2 and h_2. Measurements of these numbers can provide estimates of the ice shell thickness but not the ocean thickness, due to the weak dependence of diurnal tides on ocean depth (Hay et al., 2022). In addition to Jupiter's gravitational influence, Ganymede also interacts with the other Galilean moons, particularly with Io and Europa through their Laplace resonance. These resonance-driven interactions cause the moons to induce high-frequency tides on one another. This type of tidal response is particularly sensitive to ocean thickness, with resonance effects occurring when the natural frequencies of the ocean align with the external tidal forcing (Hay et al., 2022).

Studies have investigated the sensitivity of Ganymede's tidal response to variations in interior parameters. Moore et al. (2003) hypothesized that the existence of a liquid ocean beneath the ice shell significantly

increases the tidal amplitude, decoupling the surface ice from the interior. The study used different viscoelastic models of Ganymede, incorporating parameters like ice shell thickness, rigidity, and viscosity, to compute the Love numbers k_2 and h_2. Both models with and without subsurface oceans were considered to compare the tidal responses. Results showed that the tidal amplitude in Ganymede can exceed 7 m if a subsurface ocean is present, while it drops to less than 0.5 m in models without an ocean (Moore et al., 2003). In addition, the presence of a subsurface ocean can be inferred through spacecraft altimetry and Doppler tracking if measurements of the tidal amplitude are accurate to approximately 1 m (Moore et al., 2003).

Kamata et al. (2016) employed a 1D viscoelastic model of Ganymede's interior and computed the Love numbers k_2 and h_2 under different scenarios, both with and without a subsurface ocean. The results showed that models without a subsurface ocean exhibit a wide range of Love number amplitudes, overlapping with those predicted by models that include an ocean. In contrast, smaller phase lags are observed only in models with a subsurface ocean. Therefore, the phase lag is a key indicator of the presence of a subsurface ocean, which cannot be inferred based solely on the amplitude of tidal deformation (Kamata et al., 2016). Furthermore, if a subsurface ocean exists, the thickness of the ice shell mainly influences the Love numbers, and accurate measurements of both k_2 and h_2 are necessary to reduce uncertainties in estimating the ice shell thickness.

Hussmann et al. (2016) used the tidal phase lag to investigate Ganymede's dissipation and better constrain the interior structure, while maintaining consistency with gravitational data from Galileo. Three nominal models were defined, each consisting of a liquid iron core of density $6500\,\mathrm{kg\,m^{-3}}$, a silicate mantle, a high-pressure ice layer of density $1400\,\mathrm{kg\,m^{-3}}$, and a liquid ocean and a ice I layer both with a density of $1000\,\mathrm{kg\,m^{-3}}$. These models were used to investigate the sensitivity of the tidal phase lag to the interior structure of the satellite. The results highlighted that the phase lag difference is dominated by dissipation in the high-pressure ice layer rather than the ice I shell.

1.2.4. Libration

Librations refer to oscillations in the rotational motion of a celestial body around its equilibrium spin state. As explained in subsection 1.2.3, tidal forces induce deformations in Ganymede's shape, leading to a tidal bulge oriented in the direction of Jupiter. Due to the moon's slightly eccentric orbit, this deformation is not always exactly aligned with the planet-moon line, leading to variations in the tidal forces that generate tidal torques, which affect the moon's rotation (Baland et al., 2010).

Physical libration can occur both in latitude and longitude. However, since Ganymede's obliquity is expected to be small, studies have mainly focused on the libration in longitude (Rambaux et al., 2011; Van Hoolst et al., 2013), which represents oscillations in the equatorial plane. This motion is characterized by a libration angle that depends on the satellite's rotation and mean anomaly.

Rambaux et al. (2011) analyzed the frequencies and amplitudes of the Galilean moons' librations. The primary libration occurs at the orbital frequency under the assumption of a Keplerian orbit. Additional librations at lower frequencies arise from orbital perturbations, with amplitudes equal to or greater than the primary libration (Rambaux et al., 2011). However, these long-period librations cannot be used to infer the interior structure of Ganymede, as they are mainly independent of the moon's interior properties (Rambaux et al., 2011).

Baland et al. (2010) investigated the influence of liquid layers on the Galilean moons' librations, and how libration observations can be used to infer interior properties. The study developed a methodology to analyze longitudinal librations of satellites with up to two liquid layers. The authors showed that the presence of a subsurface ocean significantly affects the libration amplitude of the ice shell, which mostly depends on the shell thickness and on the shell-ocean density contrast (Baland et al., 2010). On the other hand, the presence of a deeper liquid layer in Ganymede does not influence the libration amplitude.

Due to the coupling between tides and librations, Van Hoolst et al. (2013) developed a framework to include their mutual influence in the analysis of longitudinal librations, an aspect that had been neglected in earlier studies. As explained in subsection 1.2.3, two types of tides can be distinguished. Short-period tides, with timescales comparable to Ganymede's rotation period, are characterized by the dynamical Love number k_2, while long-period tides, with timescales on the order of the moon's

orbital evolution, are characterized by the fluid Love number k_f. Due to this distinction, the total tidal deformation does not point exactly towards Jupiter, leading to a net torque that influences libration (Van Hoolst et al., 2013). Additionally, Van Hoolst et al. (2013) showed that zonal tides modify the polar moment of inertia, further affecting rotational variations.

In a purely solid moon, periodic tidal deformations alter the gravitational torque exerted by Jupiter, causing changes in the orientation and amplitude of the tidal bulge and variations in the polar moment of inertia, thus influencing rotational dynamics. However, if Ganymede possesses a subsurface ocean, the tidal response becomes more complex, since each layer deforms differently under Jupiter's gravitational pull (Van Hoolst et al., 2013).

Further effects arise in the presence of an internal ocean. Inter-layer gravitational torques arise when different layers become misaligned. Pressure torques act at the interface between solid and fluid layers, and in the presence of an elastic shell, additional pressure torques emerge at its lower boundary due to periodic tidal deformations (Van Hoolst et al., 2013). Other torques may also arise if the static tidal bulge of one layer is misaligned with the periodic tidal bulge of another.

Van Hoolst et al. (2013) showed that periodic tidal deformations reduce libration amplitudes compared to rigid models. In addition, the presence of oceans amplifies libration amplitudes in rigid models, but elastic deformations counteract this effect, resulting in amplitudes similar to those of entirely solid satellites. Therefore, libration observations alone are not sufficient to confirm the presence of a subsurface ocean, but they can be used to constrain properties like ice shell density and rigidity (Van Hoolst et al., 2013).

1.2.5. Obliquity

Obliquity refers to the angle between a satellite's rotational axis and the normal to its orbital plane. For the Galilean satellites, this angle is generally small and is often neglected, but studies have shown that it can provide insights into their internal structure, especially in the case of Ganymede and Callisto (e. g., Baland et al., 2012).

A satellite experiences different types of precession due to the torques exerted by the planet and other perturbing bodies. Its spin axis precesses around the orbit normal because of the triaxial shape of the satellite, while the orbital plane precesses due to the planet's oblateness and other perturbing bodies (Downey et al., 2025). The satellite's mean orbital plane is defined as the Laplace plane. The spin geometry is characterized by three main angles: the obliquity (θ), between the spin axis and the orbit normal, the inclination (i), between the orbital plane and the Laplace plane, and the longitude of the ascending node (ϕ) of the equator on the orbit plane. Due to the orbital plane precession around the Laplace plane, the spin axis also undergoes a net precession about this plane (Downey et al., 2025).

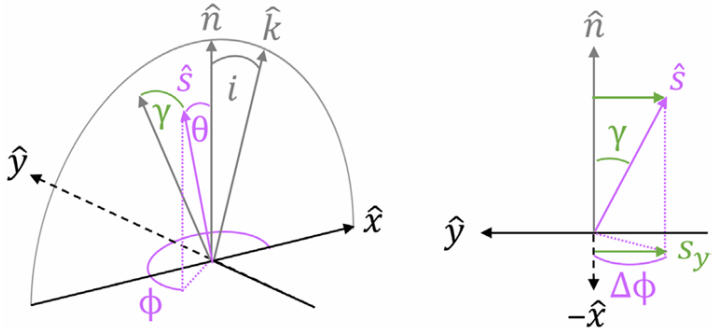

Figure 1.2: Schematic representation of the Cassini plane and its angles. **s** is the spin vector, **n** is the normal to the orbital plane, and **k** is the normal to the Laplace plane. The gray vectors and angles lie on the Cassini plane, which is the xz plane formed by **n** and **k**. θ is the obliquity, i is the inclination, and ϕ is the longitude of the ascending node. $\Delta\phi$ is the constant offset of the spin axis relative to the Cassini plane when dissipation occurs. Image credit: Downey et al. (2025, Figure 1).

The Cassini states represent the equilibrium states of the satellite's rotational evolution. They describe the equilibrium configurations of a satellite's spin axis relative to its orbit and the normal to the Laplace

plane. In a Cassini state, the spin axis and orbit normal precess synchronously around the Laplace plane normal, with the same or opposite phase (Downey et al., 2025). This precession prevents the spin axis from aligning with the orbital normal, resulting in a non-zero obliquity. In addition, during the precession cycle, the spin axis, orbit normal, and Laplace plane normal all lie within the same plane, the so-called Cassini plane.

Dissipation effects cause the system to evolve toward a Cassini state, but at the same time prevent the spin axis from aligning perfectly with the Cassini plane. This deviation from the Cassini plane is known as the Cassini plane offset and is directly related to the total amount of internal dissipation, including tidal effects and dissipation at the fluid-solid interface (Downey et al., 2025). Downey et al. (2025) showed that the Cassini plane offset can be expressed as a function of the satellite's tidal dissipation factor k_2/Q, which depends on the material properties of the different layers. Being able to measure the Cassini plane offset would allow the determination of the dissipation factor, which would otherwise be difficult to measure directly (Downey et al., 2025).

Baland et al. (2012) studied possible obliquity values for the Galilean satellites depending on their interior structure. For a solid Ganymede, obliquity values are expected to be in the range of 0.0085° to 0.0320°. When taking into account a subsurface ocean, resonant amplifications can occur, leading to higher values of obliquity, possibly reaching a few degrees (Baland et al., 2012). However, some interior models with an ocean predicted obliquity values that are consistent with a completely solid Ganymede. Therefore, multiple measurements over long periods of time are necessary to differentiate between the two cases (Baland et al., 2012).

Given the mutual influence of responses such as tidal deformation and libration, and the fact that different observables are sensitive to different interior properties, no single measurement can uniquely constrain Ganymede's internal structure. Therefore, a Bayesian framework that combines these complementary observations, as introduced in section 1.3, is necessary for a more comprehensive characterization of the moon's interior.

1.3. Bayesian Framework to Constrain Ganymede's Interior

Modeling the interior structure of a planetary body is intrinsically a non-unique process. Observations and satellite measurements can be used to constrain the parameters that characterize the interior. As an example, gravity measurements provide constraints on Ganymede's mass and moment of inertia, which can be linked to the distribution of mass within the body and, consequently, to its density profile. However, a similar density of ice and water leads to ambiguities in the inversions based solely on gravity data. On the other hand, analysis of magnetic induction data can provide insights into the hydrosphere properties of the satellite. However, the induction response depends on both the ocean's salinity and thickness, as well as the thickness of the overlying shell (Biersteker et al., 2023). Since Galileo's flybys were limited in number and timing, they could only measure magnetic responses at a single frequency, tied to Ganymede's synodic period. This results in degeneracies in the data, leaving the moon's interior structure poorly constrained.

So far, the different types of measurements have been mainly analyzed independently (e. g., Kamata et al. (2016), Kivelson et al. (2002), Schubert et al. (2004), and Sohl et al. (2002)). Studies typically assess the sensitivity of a single data set – such as magnetic induction data or tidal responses – to variations in interior parameters. Alternatively, existing measurements are used to constrain the interior structure of the satellite. For instance, Schubert et al. (2004) investigated Ganymede's interior structure using solely gravity data, while Kamata et al. (2016) analyzed the sensitivity of the satellite's tidal response to variations in interior parameters.

However, these analyses still present many uncertainties, since different measurements are sensitive to different interior model characteristics, and one data set alone is not enough to break the degeneracies between interior parameters. To overcome these limitations, a Bayesian inversion framework can be employed to improve estimates of the interior model parameters given the available observational data. For example, it has been used to constrain the Moon's interior structure using Lunar Laser Ranging (LLR) observations and data from Gravity Recovery and Interior Laboratory (GRAIL) and Lunar Orbiter Laser Altimeter (LOLA) missions (Matsuyama et al., 2016). Building on this foundation, Biersteker

et al. (2023) introduced a Bayesian approach to characterize the interiors of icy moons using magnetic induction data. Extending this work, Petricca et al. (2023) proposed a joint inversion of multiple data sets and applied it to Europa, combining gravity and magnetic field measurements within a Bayesian framework. They used a Markov-chain Monte Carlo (MCMC) algorithm to sample the parameter space of relevant interior properties and generate models consistent with both gravity and magnetic induction observations. The joint inversion allowed to simultaneously constrain the ice shell and ocean thickness. Petricca et al. (2023) showed that the combination of the data sets provided more robust estimates of Europa's hydrosphere properties with smaller uncertainties compared to previous studies, in which a single data type was considered.

The advantages of this approach are that it incorporates prior information and recovers the associated parameter uncertainties (Biersteker et al., 2023). Another advantage is the possibility to marginalize over nuisance parameters, which are parameters that are of no interest but are necessary in the model to generate the data. Marginalization consists of integrating the probability distribution over all the values of the nuisance parameters, so that the uncertainty about its value is propagated into the final result (Foreman-Mackey et al., 2013). This allows to focus only on the parameters of interest and to simplify the interpretation of the results. For more details on the theoretical background of Bayesian inference, the reader is referred to section B.3.

1.3.1. Measurement Uncertainties

In the context of Bayesian inversion, uncertainties are essential to quantify the reliability of the results: the uncertainties of the observations, which are given by measurement errors, are propagated through the model to estimate the uncertainties of the inferred parameters. In this work, we consider two distinct sources of observational uncertainties: existing measurements from the past Galileo mission and expected uncertainties from the upcoming Juice mission.

The moment of inertia and the magnetic induction amplitude have been derived from Galileo data, as explained in subsection 1.2.1 and subsection 1.2.2. These quantities, together with their associated uncertainties, are used in the analyses presented in chapter 4. Other quantities of interest, such as the tidal Love numbers and rotational parameters, have not yet been measured. For these, we rely on the expected performance of Juice, which has been quantified in several studies.

The spacecraft carries ten scientific instruments dedicated to remote sensing, geophysical studies, and in situ investigations, complemented by the radiation monitor (RADEM) and Planetary Radio Interferometer and Doppler Experiment (PRIDE) experiments (Van Hoolst et al., 2024). Among these, 3GM will provide range and Doppler data to investigate Ganymede's gravity field and constrain the presence and extent of subsurface oceans, while RIME will probe the subsurface structure of the moon down to depths of about 9 km (European Space Agency, 2023). GALA will measure topography and tidal deformation, while J-MAG will characterize the Jovian magnetic field and its interaction with Ganymede's intrinsic field (European Space Agency, 2023).

The expected uncertainties of Juice's gravity, tides, and rotational parameters have been estimated by Cappuccio et al. (2020) through a dedicated simulation of the 3GM radio science experiment, including dynamical models of Ganymede's interior response, its exosphere, and non-gravitational perturbations such as propellant sloshing. For further details on the simulation setup we refer to the original work. Table 1.3 summarizes the expected uncertainties for the tidal Love number k_2 and the rotational state parameters. For completeness, we also report the uncertainties in the gravity field coefficients in Table 1.4, although they are not used in this study.

Table 1.3: Expected uncertainties (1σ) of Ganymede's tidal Love number k_2 and rotational parameters from Juice radio science simulations (Cappuccio et al., 2020). Ψ denotes the libration amplitude and ψ the obliquity angle.

$\mathrm{Re}(k_2)$	$\mathrm{Im}(k_2)$	RA	DEC	ω	Ψ	ψ
1.0×10^{-4}	6.8×10^{-5}	2.5 µrad	1.4 µrad	8.0×10^{-14} rad s^{-1}	2.1 µrad	1.0 µrad

In addition to the uncertainties reported by Cappuccio et al. (2020), Steinbrügge et al. (2015) showed that GALA will measure the real part of Ganymede's h_2 with an absolute accuracy of approximately

Table 1.4: Expected uncertainties (1σ) of Ganymede's GM and quadrupole coefficients from Juice radio science simulations (Cappuccio et al., 2020). These are reported here for completeness, although not used in this study.

GM	J_2	C_{21}	S_{21}	C_{22}	S_{22}
$3.8 \times 10^{-4}\,\mathrm{km^3\,s^{-2}}$	8.6×10^{-10}	1.7×10^{-10}	7.2×10^{-11}	3.0×10^{-10}	5.1×10^{-9}

2.6×10^{-2}, considering an average height measurement error of 6-7 m, which includes uncertainties in pointing and orbit determination. In addition, GALA will measure the libration amplitude of the outer shell with an accuracy between 2.5 µrad and 6.6 µrad, which corresponds to a shell libration amplitude of 6.6 m to 17.5 m at the equator (Steinbrügge et al., 2019).

Finally, Juice will characterize the magnetic field continuously at multiple frequencies (Grasset et al., 2013). Specifically, it will measure the magnetic field with an accuracy of better than 0.1 nT at three characteristic timescales: Ganymede's orbital period (171 h), the rotation of Jupiter's magnetosphere rotation (10.5 h), and the solar rotation period (27 d) (European Space Agency, 2014).

1.4. Research Questions

From the background information provided in section 1.1, section 1.2 and section 1.3, the following research question is formulated:

How can the joint inversion of gravity, magnetic induction, tidal and libration observations improve the characterization of the interior structure of Ganymede?

The main research question can be further divided into four sub-questions that will guide the research process.

1. **[SQ1.1] What is the sensitivity of the different observations to variations in Ganymede's interior structure?**
   Before investigating the Bayesian inversion of combined data sets, it is important to conduct a sensitivity analysis to evaluate how variations in the model parameters influence the different measurements. By examining the impact of parameters such as the ice shell thickness, ocean salinity, and ocean thickness, one can identify which parameters most influence the observations. This understanding helps to define the parameters of interest and the range of values that should be considered in the inversion. This ensures that the inversion process captures the most relevant parameters and is robust to variations in input data.
2. **[SQ1.2] To what extent can the joint inversion of available data – static gravity and magnetic induction – constrain Ganymede's interior structure?**
   Following the promising results obtained by Petricca et al. (2023) for Europa, the methodology is applied here to Ganymede. A first inversion of gravity and magnetic data will be performed to constrain Ganymede's interior parameters. This sub-question aims to assess the impact of combining these two data sets and compare the results to previous studies.
3. **[SQ1.3] How can the addition of tidal and libration observations to the inversion improve the characterization of Ganymede's interior structure?**
   Tidal and libration measurements provide additional constraints on Ganymede's interior structure, specifically on the hydrosphere properties. This sub-question aims to evaluate the performance of the inversion process when additional observations are included.
4. **[SQ1.4] To what extent do the uncertainties in the input data affect the reliability of the inversion results?**
   Parameter uncertainties play a crucial role in the Bayesian inversion process, as they directly impact the posterior distributions of model parameters. This sub-question aims to identify thresholds in observation uncertainties beyond which the credible intervals of the inferred parameters become too wide to be scientifically useful. Understanding these thresholds helps define acceptable bounds for data precision to maintain valuable inversion results.

1.5. Report Outline

The structure of the report is as follows. Chapter 2 describes the methodology used in this project, including the interior modeling of Ganymede, the computation of the observables, the sensitivity analysis of the model parameters, and the Bayesian inversion framework. Chapter 3 presents the results of the Monte Carlo (MC) analysis, in which parameters are varied simultaneously and the corresponding observables are computed for each interior model. This analysis provides insight into the sensitivity of the observables to different parameters and helps identify which parameters can be constrained by the available data. Chapter 4 describes the setup and results of the Bayesian inversion used to retrieve the interior parameters of Ganymede. Multiple inversions are performed, each using a different set of observations. Chapter 5 concludes the main body of the report by summarizing the results and suggesting possible future research directions.

Appendix A presents the planning of the project; Appendix B provides the theoretical background on some of the observables considered in the project and on the Bayesian inversion framework; Appendix C describes the validation and verification process; Appendix D and Appendix E contain additional results from the sensitivity analysis and Bayesian inversion, respectively.

2

Methodology

The main research objective of this project is to improve the understanding of Ganymede's interior structure by combining different observational datasets to better constrain the moon's interior properties. To achieve this goal, the project is divided into two main parts: a sensitivity analysis and a Bayesian inversion. The sensitivity analysis provides insights into how the different parameters affect the observables, while the Bayesian inversion is used to retrieve a set of interior models that best fit the data. This chapter outlines the methodology used to address the research questions and its sub-questions presented in section 1.4.

This work employs the scientific color maps vik and batlow (Crameri, 2023) for the visualization of the results, avoiding visual distortion of the data for individuals with color-vision deficiencies (Crameri et al., 2020).

2.1. Sensitivity Analysis

Sensitivity analysis is a technique used to assess how variations in model parameters influence the resulting observables. By systematically varying interior parameters within a defined range, we can determine which factors have the strongest impact on modeled responses. This process helps to identify the most influential parameters and define plausible ranges of values for each parameter, refining our understanding of the moon's interior structure. In the context of this project, performing a sensitivity analysis will allow us to evaluate how changes in physical properties, such as layer thicknesses, densities, and composition, affect the gravity, magnetic induction, tidal, and libration response.

To perform this analysis, several steps are required. First, we must define Ganymede's interior model, specifying the number of layers, the relevant parameters for each layer, and their plausible ranges. Next, we generate synthetic data by computing the expected observables for the different interior models obtained by varying the parameters within their defined ranges. This requires building a forward model for each observable to describe how Ganymede's interior structure influences the measured signals. Finally, we analyze the sensitivity of the observables to variations in model parameters, identifying the most influential factors and assessing their impact on the data.

The key observables for this analysis are the gravity field, magnetic induction response, tidal deformation, and libration. Obliquity measurements are not considered because they are expected to be small, as mentioned in subsection 1.2.5. The gravitational field measured by the Galileo spacecraft yields Ganymede's mass and moment of inertia. These quantities are well constrained and have been extensively used to model the moon's interior structure, as discussed in subsection 1.2.1. For this reason, instead of generating synthetic gravity data, we use the observed values as constraints to ensure that our models remain consistent with existing gravity measurements. This approach is further detailed in subsection 2.1.1.

2.1.1. Ganymede's Interior Model

Ganymede's interior structure is characterized by a metallic core, a rocky mantle, and an ice shell, as described in subsection 1.2.1. The shell is likely to be composed of an ocean layer sandwiched between an ice I shell on top and a high-pressure (HP) ice layer on the bottom. Therefore, we consider a five-layer model of Ganymede's interior. Each layer is characterized by homogeneous density and mechanical properties, and no lateral variations are considered. The moon is assumed to be in hydrostatic equilibrium.

The parameters that define the interior model and that are varied in the sensitivity analysis are summarized in Table 2.1. The parameter ranges are based on values from the literature, although in some cases, broader ranges are considered to explore a wider parameter space. The ocean is assumed to be composed of water and magnesium sulfate ($MgSO_4$), since icy satellite oceans are generally believed to be rich in this compound. This assumption is based on equilibrium chemical models of water-rock interactions and is supported by infrared spectra obtained from Galileo's Near-Infrared Mapping Spectrometer (Vance et al., 2014).

Since only models that include an ocean layer are considered, the upper limit of the ice shell thickness is constrained by $MgSO_4$ phase diagrams. In fact, a liquid ocean can exist only if the pressure at the ice-ocean boundary does not exceed the triple point pressure. By computing the pressure profile within the ice shell, we determine the maximum thickness of the ice shell that allows for the existence of an ocean layer. Taking into account various ocean compositions and ice shell densities, the ocean depth is constrained to lie within 0–160 km, a range that includes the value of approximately 150 km inferred from magnetic observations (Kivelson et al., 2002). This scenario corresponds to the lowest ice density considered, while the composition does not affect the results. For the analysis, tabulated data of the phase diagrams are taken from the *PlanetProfile* software (Styczinski et al., 2023), an open-source software to model the interior structure of rocky and icy bodies. It derives radial profiles of mechanical, thermodynamic, and electrical properties in a self-consistent manner, integrating observed and measured properties with assumptions about material composition and laboratory equation-of-state data, using geophysical and thermodynamic models (Styczinski et al., 2023).

Table 2.1: Ganymede's interior parameters explored in the sensitivity analysis. For some of the variables, wider ranges are considered compared to the reported values in the literature.

Parameter	Units	Range	Reference
Core radius r_c	km	500 - 1000	Schubert et al. (2004) and Sohl et al. (2002)
Mantle radius r_{ma}	km	1550 - 2050	Schubert et al. (2004) and Sohl et al. (2002)
Mantle shear modulus $\mu_{s,ma}$	GPa	50 - 100	Hussmann et al. (2016) and Moore et al. (2003)
Mantle viscosity η_{ma}	Pa s	1×10^{18} - 1×10^{22}	Hussmann et al. (2016) and Moore et al. (2003)
HP ice density ρ_{hp}	kg m^{-3}	1100 - 1400	Hussmann et al. (2016) and Sohl et al. (2002)
HP ice shear modulus $\mu_{s,hp}$	GPa	1 - 10	Moore et al. (2003)
HP ice viscosity η_{hp}	Pa s	1×10^{12} - 1×10^{20}	Hussmann et al. (2016)
Weight percent of $MgSO_4$ in the ocean wt	%	0 - 10	Vance et al. (2014)
Ice shell thickness D_{ice}	km	1 - 160	Kivelson et al. (2002)
Ice shell density ρ_{ice}	kg m^{-3}	900 - 1300	Anderson et al. (1996) and Vance et al. (2014)
Ice shell shear modulus $\mu_{s,ice}$	GPa	0.1 - 10	Kamata et al. (2016)
Ice shell viscosity η_{ice}	Pa s	1×10^{12} - 1×10^{20}	Hussmann et al. (2016)
Poisson's ratio υ	-	0.3 - 0.49	Beuthe (2015)

Each layer is generally characterized by its thickness (or external radius) and density. However, not all of these parameters are listed in Table 2.1, since some interior properties can be derived directly from the sampled parameters, based on constraints such as Ganymede's total mass, Moment of Inertia (MoI), and Equation-Of-State (EOS) of $MgSO_4$ solutions. Once these constrained parameters are computed, the physical validity of an interior model is assessed by checking the conditions listed in Table 2.2. Models that do not meet these criteria are discarded.

Table 2.2: Constraints imposed on Ganymede's interior parameters derived from the free parameters.

Parameter	Units	Constraint	Rationale
Core density ρ_c	$kg\,m^{-3}$	5150 - 8000	Range of densities consistent with Fe–FeS to Fe compositions (Anderson et al., 1996)
Mantle density ρ_{ma}	$kg\,m^{-3}$	3000 - 4000	Range of densities representative of an olivine-rich silicate mantle (Sohl et al., 2002)
Hydrosphere densities ρ_{ice}, ρ_o, ρ_{hp}	$kg\,m^{-3}$	$\rho_{ice} < \rho_o < \rho_{hp}$	Condition for a gravitationally stable hydrosphere

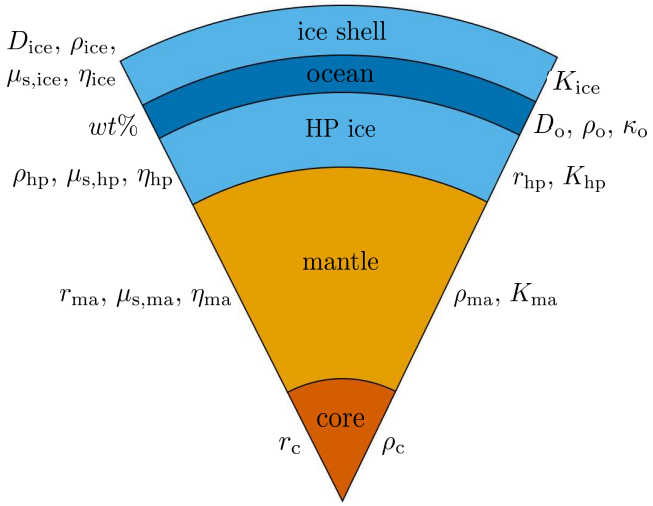

Figure 2.1: Schematic of Ganymede's interior model, illustrating the parameters that characterize each layer. The free parameters are listed on the left, while the constrained ones are on the right. An additional free parameter, the Poisson's ratio υ, is not shown in the figure.

The adopted interior model and its parameters are shown in Figure 2.1. In the following, we describe how the different interior parameters are computed.

Hydrosphere

Two key ocean parameters affecting the observations are the density and electrical conductivity, which can be derived from the ocean composition. The ocean conductivity is related to the concentration of dissolved $MgSO_4$ by (Hand et al., 2007):

$$C = c_3\kappa_o^3 + c_2\kappa_o^2 + c_1\kappa_o + c_0 \tag{2.1}$$

where $C = wt \times 10$ is the concentration converted to $g\,kg^{-1}$. The coefficients c_0 to c_3 are listed in Table 2.3.

The density of the $MgSO_4$-water solution is evaluated using parameterized data from *PlanetProfile* (Styczinski et al., 2023). Given pressure, temperature and salinity values, the EOS measurements can be interpolated to determine the ocean density. The valid ranges for these input parameters are provided in

Table 2.3: Constants values of Equation 2.1 (Hand et al., 2007).

c_0	c_1	c_2	c_3
-0.0129	15.2108	12.0161	-1.7268

Styczinski et al. (2023, Table 1). Specifically, the temperature must be within 253 K to 373 K. However, considering the possible thicknesses of the ice shell and salinity values of the ocean presented in Table 2.1, temperatures as low as 250 K can occur. Therefore, density values for temperatures below the lower limit are extrapolated from the available data. The pressure is assumed to be the mean pressure of the ocean layer.

Another key constraint comes from the phase diagram of water ice, which determines the depth at which the HP ice forms. A liquid ocean can exist due to the anomalous behavior of the melting temperature of ice I, which decreases with increasing pressure until it reaches a minimum at the triple point. For pure water, the triple point is located at $T_{\text{triple}} = 251.15\,\text{K}$ and $p_{\text{triple}} = 207\,\text{MPa}$ (Chizhov, 1993). Although the overall behavior remains the same, the triple point values vary depending on the composition of the ice.

As discussed in subsection 1.2.2, the presence of an induced magnetic field in Ganymede suggests the existence of a salty subsurface ocean. Following the study by Vance et al. (2014), we therefore consider a contamination of magnesium sulfate in the ocean. The authors used phase-equilibrium data and thermodynamic properties of $MgSO_4$ solutions to model the freezing behavior of water ice in Ganymede's subsurface ocean. Through least square fitting of experimental data, they obtained the Margules coefficients to reconstruct the phase diagram of $MgSO_4$ solutions. For more details on the methodology, the reader is referred to the original paper (Vance et al., 2014). The obtained phase diagrams for different aqueous $MgSO_4$ solutions are shown in Figure 2.2.

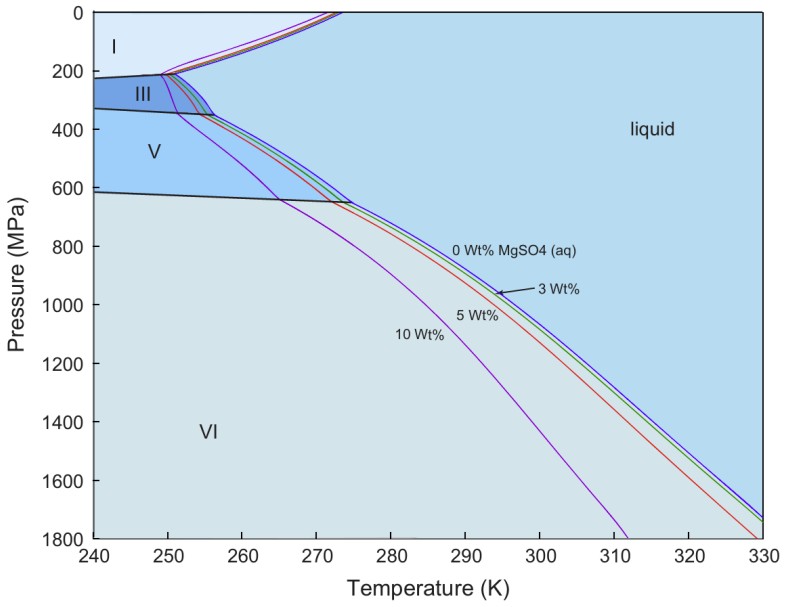

Figure 2.2: Water phase diagram for different (aq)$MgSO_4$ solutions. Image credit: Vance et al. (2014, Figure 1).

We use tabulated data from the *PlanetProfile* software (Styczinski et al., 2023) for the EOS of $MgSO_4$ solutions, derived from the work of Vance et al. (2014). The ice liquidus curves for different $MgSO_4$ concentrations are used to determine the depth of the ocean-HP ice boundary.

To compute the temperature at the bottom of Ganymede's ice shell, we first need to determine the pressure at the ice-ocean boundary. This requires calculating the radial profiles of mass and pressure in Ganymede's interior, which can be done using the principles of mass conservation and hydrostatic

equilibrium:

$$dM = 4\pi\rho r^2 dr \qquad\qquad dp = \rho g(r) dr \tag{2.2}$$

Here, $g(r)$ is the local gravitational acceleration at radius r, given by:

$$g(r) = \frac{GM(r)}{r^2} \tag{2.3}$$

By discretizing these equations, we compute the radial profiles of mass and pressure.

Typically, the mass profile is computed from the center outwards, integrating from the core to the surface. However, not all the layer boundaries and densities are yet defined, making it difficult to follow this approach for the entire interior structure. Since we are specifically interested in the pressure profile within the ice shell, we take a different approach:

- We integrate downward from the surface, where the total mass of Ganymede is known.
- The ice shell is divided into N layers, each with a thickness Δr.
- The mass profile of the ice shell is computed as:

$$M_{N-i} = M_{N-i+1} - \frac{dM}{dr}\Delta r \tag{2.4}$$

  Here, $i = 1 \dots N$, $M_N = M_\mathrm{G}$ and the density corresponds to the ice shell density.

With the mass profile determined, we can calculate the gravity profile using Equation 2.3 and then integrate the hydrostatic equilibrium equation to obtain the pressure profile within the ice shell as:

$$p_{N-i} = p_{N-i+1} + \frac{dp}{dr}\Delta r \tag{2.5}$$

where $i = 1 \dots N$ and $p_N = 0$. We therefore obtain the pressure at the bottom of the ice shell $p_{\mathrm{ice,b}} = p_0$. Finally, to determine the temperature at the ice-ocean boundary, we use the EOS of $MgSO_4$ solutions. Since the pressure at this boundary has been computed, we interpolate the temperature from the liquidus curves provided by the *PlanetProfile* software (Styczinski et al., 2023).

We assume a fully convective ocean. Thus, its temperature remains constant throughout this layer, while the pressure increases with depth. With the ocean temperature known, we use the phase diagram to identify the pressure at which the transition to HP ice occurs, again interpolating data from the *PlanetProfile* software (Styczinski et al., 2023). To determine the depth of the ocean-HP ice boundary, we compute the mass and pressure profiles within the ocean layer in the same way as for the outer shell. However, unlike the ice layer, whose thickness is known, the ocean thickness is not predefined. Therefore, we start from the base of the ice shell, where the pressure is $p_{\mathrm{ice,b}}$, and we integrate downward in discrete radial steps Δr, updating the mass and pressure at each step using Equation 2.4 and Equation 2.5. The integration continues until the pressure reaches the phase transition value at which HP ice forms, and the corresponding depth gives the location of the ocean-HP ice boundary. This defines the external radius of the HP ice layer, while the thickness of the ocean layer follows from the total radius of Ganymede and the radii of the other layers.

Deep Interior

Two additional constraints are derived from Ganymede's total mass and MoI, which depend on the interior parameters as described in Equation 2.6 and Equation 2.7:

$$M_\mathrm{G} = \frac{4}{3}\pi \sum_{i=1}^{5} \rho_i \left(r_i^3 - r_{i-1}^3\right) \tag{2.6}$$

$$I/MR^2 = \frac{1}{M_\mathrm{G} R_\mathrm{G}} \frac{8}{15}\pi \sum_{i=1}^{5} \rho_i \left(r_i^5 - r_{i-1}^5\right) \tag{2.7}$$

where $r_0 = 0$ and layers indices 1 to 5 correspond to the core, mantle, HP ice, ocean and ice shell, respectively. Rather than independently varying the thickness and density of each layer to compute these quantities, we use the total mass and MoI values obtained from the Galileo mission as constraints. This approach ensures that the generated models are consistent with gravitational observations. As a result, once the other interior parameters are defined, the remaining two parameters can be determined consistently with the gravity data. We choose to constrain the densities of the core and the mantle, which are therefore not explicitly listed in Table 2.1.

Each time a model is generated, the values of total mass and MoI are randomly sampled from a normal distribution centered in the expected value with a standard deviation equal to the corresponding uncertainty, as listed in Table 1.1. The values are then used to compute the core and mantle densities according to Equation 2.6 and Equation 2.7.

Compressibility

The ice shell, HP ice and mantle layers are considered to be compressible. Their bulk modulus is related to the shear modulus and Poisson's ratio by (Weijermars, 1997):

$$\frac{\mu_s}{K} = \frac{3(1-2\upsilon)}{2(1+\upsilon)} \tag{2.8}$$

From Equation 2.8, we can compute the bulk modulus of the ice shell, HP ice and mantle layers using their shear modulus and Poisson's ratio. For each model, υ is randomly sampled from a uniform distribution in the range specified in Table 2.1 and is considered equal for all layers.

By varying the free parameters within the ranges specified in Table 2.1, Ganymede's interior models are generated and the responses are computed according to the methodologies described in subsection 2.1.2, subsection 2.1.3, and subsection 2.1.4. A schematic of this process is presented in the flowchart shown in Figure 2.3.

2.1.2. Magnetic Induction Response Model

To investigate Ganymede's magnetic induction response, we adopt the methodology outlined by Petricca et al. (2023), who build upon the work of Vance et al. (2021). We remind the reader that the focus of this study is on the induced magnetic field response, and the intrinsic magnetic field of Ganymede is not considered in the inversion process, as explained in subsection 1.2.2. The induced response results from time-dependent variations in Jupiter's magnetospheric field, which interacts with Ganymede's conductive layers. Since Jupiter's magnetic dipole is tilted by 9.6° relative to its rotation axis and Ganymede's orbit is closely aligned with the planet's equatorial plane, periodic fluctuations in Jupiter's field drive the induction response (Vance et al., 2021).

Additional factors influencing the induced response include the depth-dependent electrical conductivity of the ocean, orbital perturbations from other Galilean moons, and motion-induced fields generated by ocean dynamics. All of these sources, characterized by different time scales, induce magnetic fields oscillating at their same frequencies.

Figure 2.4 shows the time series spectra of the induced magnetic field oscillations (Vance et al., 2021). Three main periods are visible: Ganymede's orbital period (171.57 h) and the Jovian synodic and half-synodic periods (10.53 h and 5.27 h, respectively). The plot was obtained by computing the time series spectra of the magnetic field variations experienced by Ganymede under specific assumptions. For more details, the reader is referred to Vance et al. (2021).

The frequency-dependent response to the excitation field A_n^e is a normalized, complex amplitude that indicates how well a body behaves as a perfect conductor (Vance et al., 2021, Supporting information), and it is characterized by an amplitude $A = |A_n^e|$ and a phase delay $\nu = -\arg(A_n^e)$. It is a dimensionless quantity whose amplitude ranges from 0 to 1, where 1 indicates a perfect conductor and 0 indicates no induction response.

Since Jupiter's magnetic field is almost uniform across Ganymede (Vance et al., 2021), for the purpose of this study, only degree $n = 1$ will be considered, and therefore the response will be noted as A^e.

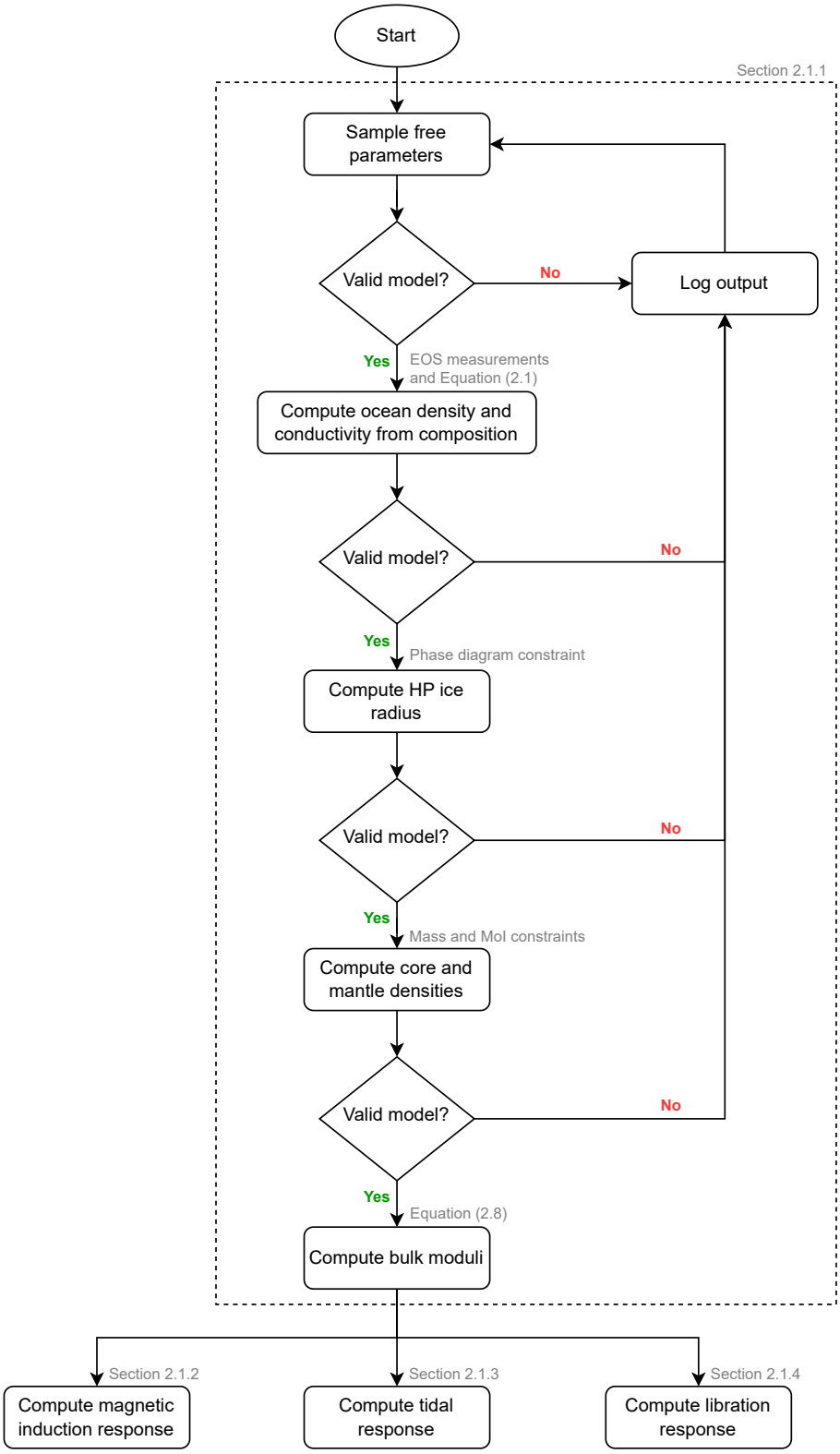

Figure 2.3: Flowchart showing the steps involved in generating Ganymede's interior models.

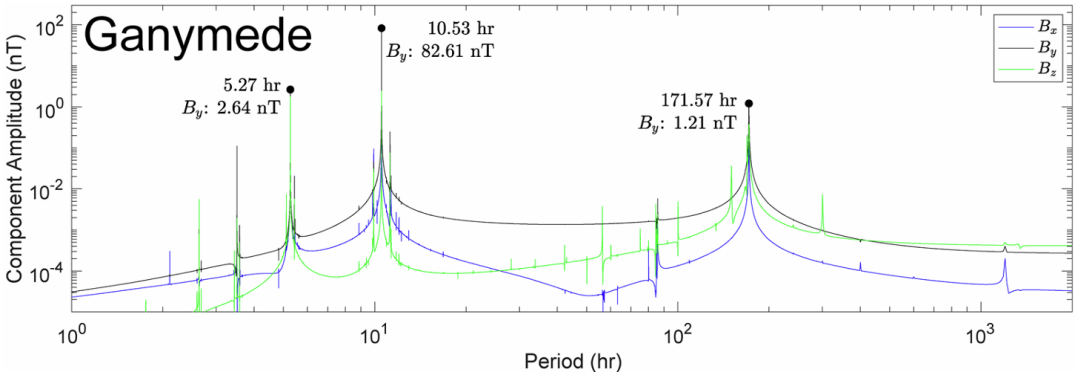

Figure 2.4: Time series spectra of the magnetic field fluctuations experienced by Ganymede. The three main periods and the corresponding peak values are reported. Image credit: Vance et al. (2021).

This assumption implies that the magnetic field is described only by the lowest degree of the spherical harmonic expansion, which represents a dipole field, and its strength is constant over the surface of the moon.

Following the work of Petricca et al. (2023), the complex amplitude of the induced magnetic field is defined as:

$$A^e = A\, e^{-i\,\nu} = \left(\frac{r_\mathrm{o}}{R}\right)^3 \frac{j_2\,(k\,r_\mathrm{hp})\,y_2\,(k\,r_\mathrm{o}) - j_2\,(k\,r_\mathrm{o})\,y_2\,(k\,r_\mathrm{hp})}{j_0\,(k\,r_\mathrm{o})\,y_2\,(k\,r_\mathrm{hp}) - j_0\,(k\,r_\mathrm{hp})\,y_2\,(k\,r_\mathrm{o})} \tag{2.9}$$

where

$$k = \sqrt{i\,\theta\,\mu_0\,\kappa} \tag{2.10}$$

A detailed derivation of this expression can be found in Vance et al. (2021, Supporting Information, Text S1). j_m and y_m are the spherical Bessel functions of the first and second kind, respectively, of order m. The wave number k depends on the ocean electrical conductivity κ, the magnetic permeability μ_0, and the driving field's angular frequency of oscillation θ. r_o is the radius of the ocean-ice shell interface, while r_hp is the radius of the HP ice-ocean interface. Even though magnetic field oscillations occur at multiple frequencies, including components from the synodic and orbital periods, along with their harmonics and beat frequencies, we focus solely on Jupiter's synodic period (10.53 h) to compute the induction response, as it provides the dominant contribution, as shown in Figure 2.4.

The expression in Equation 2.9 is valid only for a body with a single, uniform conducting layer. As discussed in subsection 1.2.2, Ganymede's intrinsic magnetic field is likely generated by dynamo action in a partially molten core. Due to its high electrical conductivity, the core could contribute to the induction response of the moon. Seufert et al. (2011) investigated the electromagnetic induction response of the Galilean moons to deduce information about their subsurface oceans and core layers. Their results showed that, although the core induces magnetic signals and interacts with the ocean through mutual induction effects, these contributions are expected to be significantly weaker than the strength of the ocean's response. We can therefore assume that the ocean is the only uniformly conducting layer in Ganymede and neglect the core's contribution to the induction response.

2.1.3. Tidal Response Model

To generate the tidal response of Ganymede, the LOV3D Matlab software (Rovira-Navarro et al., 2024) is used. This software implements a spectral method to compute the tidal response of bodies with a stratified interior, allowing for the inclusion of lateral variations. The output includes the Love number spectra and the corresponding radial functions.

The Love numbers h_n and k_n describe the body's response to tidal forces. These dimensionless quantities relate the external tidal potential to the radial displacement and gravitational potential perturbations at the surface:

$$h_n = -\frac{u_{\mathrm{r},n}\, g_\mathrm{surf}}{\Phi^T{}_n} \qquad\qquad k_n = -\frac{\Phi_{\mathrm{p},n}}{\Phi^T{}_n}, \tag{2.11}$$

where $u_{r,n}$ is the radial displacement, $\Phi_{p,n}$ is the perturbation in the gravitational potential, and ${\Phi^T}_n$ is the imposed tidal potential of degree n.

The governing equations that determine the tidal response of a self-gravitating body are the mass and momentum conservation equations and Poisson's equation. These equations are linearized around a state of hydrostatic equilibrium, characterized by gravitational potential Φ_0, pressure p_0, and density ρ_0 (Rovira-Navarro et al., 2024). Given the displacement vector $\mathbf{u}$ and local perturbations in the stress tensor $\boldsymbol{\sigma}'$, density ρ', and gravitational potential Φ', the linearized equations are (Rovira-Navarro et al., 2024):

$$\rho' = -\rho_0(\nabla \cdot \mathbf{u}) - \mathbf{u} \cdot \nabla\rho_0 \tag{2.12}$$

$$\nabla \cdot \boldsymbol{\sigma}' - \rho_0\nabla(g\,\mathbf{u} \cdot \mathbf{e_r}) + g\rho_0(\nabla \cdot \mathbf{u})\mathbf{e_r} - \rho_0\nabla\Phi' = 0 \tag{2.13}$$

$$\nabla^2\Phi' = 4\pi G\rho' \tag{2.14}$$

where $\mathbf{e_r}$ is the radial vector.

By expanding the relevant fields in the spectral domain, the original three-dimensional system of equations is reduced to a set of equations that depend only on the radial coordinate. The system of differential equations is integrated numerically from the core-mantle boundary to the surface using a Runge-Kutta scheme, and the solution is obtained by applying specific boundary conditions (Rovira-Navarro et al., 2024).

The inputs to the software are:

- Ganymede's interior model, including the number of layers, their radii, densities, and mechanical properties.
- The tidal potential, described by its period, amplitude, degree and order.
- Numeric parameters to define, e. g., radial discretization and code parallelization settings.

For the purpose of this study, we are interested in the real and imaginary parts of the k_2 and h_2 Love numbers. The real part represents the elastic response of Ganymede to tidal forces in terms of gravitational potential (k_2) and surface deformation (h_2). The imaginary parts account for the dissipative effects due to the viscoelastic properties of the layers, which cause internal friction and heat dissipation. For spherically symmetric bodies with no lateral variations, the response of the body to tidal forces is at the same degree as the tidal potential, and does not depend on its order (for more details, see section B.2). Therefore, we only consider a forcing of degree $n = 2$ and order $m = 0$, with a period of $P_o = 7.16\,\mathrm{d}$ and an amplitude of 1.

2.1.4. Libration Model

To compute Ganymede's librations, the work of Van Hoolst et al. (2013) is used. This study includes the effects of periodic tidal deformations on the libration of satellites with a subsurface ocean. They consider the gravitational torque exerted by the central planet, the torques between the periodic tidal bulges of different layers, and the zonal tides that periodically change the polar moment of inertia to compute the amplitudes of the longitudinal librations.

The governing equations are derived by considering the torques and changes in the polar moment of inertia due to periodic tidal deformations, and they include coupling terms that account for the interactions between the ice shell and the solid interior, as well as the effects of zonal tides (Van Hoolst et al., 2013). The equations account for both the free and forced librations of the satellite. The former describe the natural oscillation frequency of the satellite and are determined by the internal structure, while the latter is influenced by the periodic tidal deformations. For more details, the reader is referred to the methodology described by Van Hoolst et al. (2013, Section 3.4).

The longitudinal librations of an icy satellite with a subsurface ocean are governed by the following system of equations (Van Hoolst et al., 2013):

$$\bar{I}_s\ddot{c}_s + K_1c_s + K_2c_i = 4eK_3\sin M \tag{2.15}$$

$$\bar{I}_i\ddot{c}_i + K_4c_s + K_5c_i = 4eK_6\sin M \tag{2.16}$$

where M is the mean anomaly of Ganymede's orbit, c_s and c_i are the libration angles of the shell and solid interior, respectively, and $\bar{I}_\mathrm{s}$ and $\bar{I}_\mathrm{i}$ are their polar moments of inertia. The coefficients $K_1, K_2, \ldots, K_6$ describe the interaction between the ice shell and the solid interior.

At the orbital period, the amplitudes of the forced longitudinal librations are (Van Hoolst et al., 2013):

$$\Psi_\mathrm{s} = \frac{4e(K_3K_5 - K_2K_6 - n^2K_3\bar{I}_\mathrm{i})}{\bar{I}_\mathrm{i}\bar{I}_\mathrm{s}(n^2 - r_1^2)(n^2 - r_2^2)}, \tag{2.17}$$

$$\Psi_\mathrm{i} = \frac{4e(K_1K_6 - K_3K_4 - n^2K_6\bar{I}_\mathrm{s})}{\bar{I}_\mathrm{i}\bar{I}_\mathrm{s}(n^2 - r_1^2)(n^2 - r_2^2)}, \tag{2.18}$$

where n is the mean motion and the free libration frequencies f_1 and f_2 are given by:

$$f_{1,2}^2 = \frac{K_1\bar{I}_\mathrm{i} + K_5\bar{I}_\mathrm{s} \pm \sqrt{4(K_2K_4 - K_1K_5)\bar{I}_\mathrm{i}\bar{I}_\mathrm{s} + (K_1\bar{I}_\mathrm{i} + K_5\bar{I}_\mathrm{s})^2}}{2\bar{I}_\mathrm{i}\bar{I}_\mathrm{s}}. \tag{2.19}$$

These equations describe how the periodic tidal deformation of Ganymede influences its libration amplitude.

The inputs to the model are an interior model of Ganymede, characterized by the radii of the layers, their densities and mechanical properties, the orbital eccentricity and the forcing characteristics, analogous to the tidal forcing described in subsection 2.1.3. The outputs are the amplitude and frequency of the longitudinal libration, as expressed by Equation 2.17, Equation 2.18, and Equation 2.19.

2.2. Bayesian Inversion

Bayesian inversion is a probabilistic approach for estimating parameters that allows to integrate multiple datasets while accounting for uncertainties in both observations and model parameters. In this project, it is employed to characterize the interior structure of Ganymede given constraints from magnetic induction, tidal, and libration observations. As explained in section 1.3, this approach provides a robust framework for incorporating independent datasets and generating interior models of Ganymede that are consistent with all available observations.

The sensitivity analysis outlined in section 2.1 identifies the interior model parameters with the greatest influence on the different datasets. Estimates of these model parameters are now retrieved through the Bayesian inversion process, which consists of different steps:

- Prior distribution: Each parameter of interest is assigned a prior distribution, based on previous studies or physical constraints.
- Likelihood function: The likelihood function is defined as the probability of observing the data given the model parameters. It is used to update the prior distribution.
- Posterior distribution: The posterior distribution is obtained by combining the prior distribution and the likelihood function using Bayes' theorem.
- MCMC sampling: The posterior distribution is sampled using the MCMC algorithm, which generates models that are consistent with the different observables.
- Uncertainty estimation: A measure of the uncertainty for the estimated parameters is obtained from the posterior distribution.

To achieve this, retrieval models for magnetic induction, tidal response, and libration are fitted to spacecraft observations. Since some of these data are not yet available, we define a benchmark interior model and use it to generate synthetic observations with the forward models described in subsection 2.1.3 and subsection 2.1.4.

In Bayesian probability theory, the plausibility of certain hypotheses or model parameters is expressed as the probability of these quantities given observed data and prior information. The likelihood function is defined as the probability of observing the data given the model parameters (Gregory, 2005). With the assumption of uncorrelated observations $\boldsymbol{\Theta}$, i. e., independent, additive Gaussian uncertainties, and

given a certain model $\bar{M}_j$, the model parameters $\mathbf{X}$ and any prior information I, the likelihood function is computed as (Matsuyama et al., 2016, Supporting Information):

$$p(\mathbf{\Theta}|\mathbf{X}, \bar{M}_j, I) \propto \exp\left(-\frac{1}{2}\sum_{i=1}^{n_{\text{obs}}}\left(\frac{\Theta_i - \Theta_i^{\bar{M}_j}}{\sigma_i}\right)^2\right) \tag{2.20}$$

where σ_i is the uncertainty associated with the i-th observation. On the other hand, the prior probability distribution $p(\mathbf{X}|\bar{M}_j, I)$ represents the information available about the model parameters before observing the data. The model parameters are assumed to have a uniform prior distribution.

Bayes' theorem relates the likelihood function to the prior probability distribution of the model parameters to obtain the posterior probability distribution, which represents our knowledge about the model parameters after observing the data (Gregory, 2005):

$$p(\mathbf{X}|\mathbf{\Theta}, \bar{M}_j, I) = C \times p(\mathbf{\Theta}|\mathbf{X}, \bar{M}_j, I) \times p(\mathbf{X}|\bar{M}_j, I) \tag{2.21}$$

where C is a normalization constant (see section B.3 for more details). The posterior probability distribution is sampled using a MCMC algorithm to explore the parameter space and estimate the model parameters that best fit the data.

The `emcee` Python implementation of the MCMC algorithm (Foreman-Mackey et al., 2013) is used to sample the parameter space. It is an affine-invariant ensemble sampler that has the advantage of requiring hand-tuning of only one or two parameters. In addition, it allows for parallelization, which is useful when dealing with computationally expensive models.

The probability distributions of the model parameters are explored using an ensemble sampler with random walkers, following the Affine Invariant Stretch Move algorithm (Goodman et al., 2010). The process begins by selecting initial parameter values, assigned to different walkers, which are then updated at each iteration. At each step j, a walker proposes a new position by scaling its distance relative to another randomly chosen walker in the ensemble. The retrieval models compute the magnetic induction amplitude, Love numbers, and shell libration amplitude for the proposed model and the likelihood function of the new solution is evaluated using Equation 2.20. The new solution $j+1$ is accepted if the ratio p_{j+1}/p_j, multiplied by a scaling factor, is greater than a random number drawn uniformly between 0 and 1. Otherwise, the walker stays at the previous position and a new solution is proposed. This qualitative description of the algorithm is based on the explanation provided in Foreman-Mackey et al. (2013).

The Bayesian inversion process yields a posterior distribution for each model parameter. Statistical quantities, such as the posterior mean and posterior mode, can then be used to report parameter estimates in terms of best-fit values and associated uncertainties (Gregory, 2005).

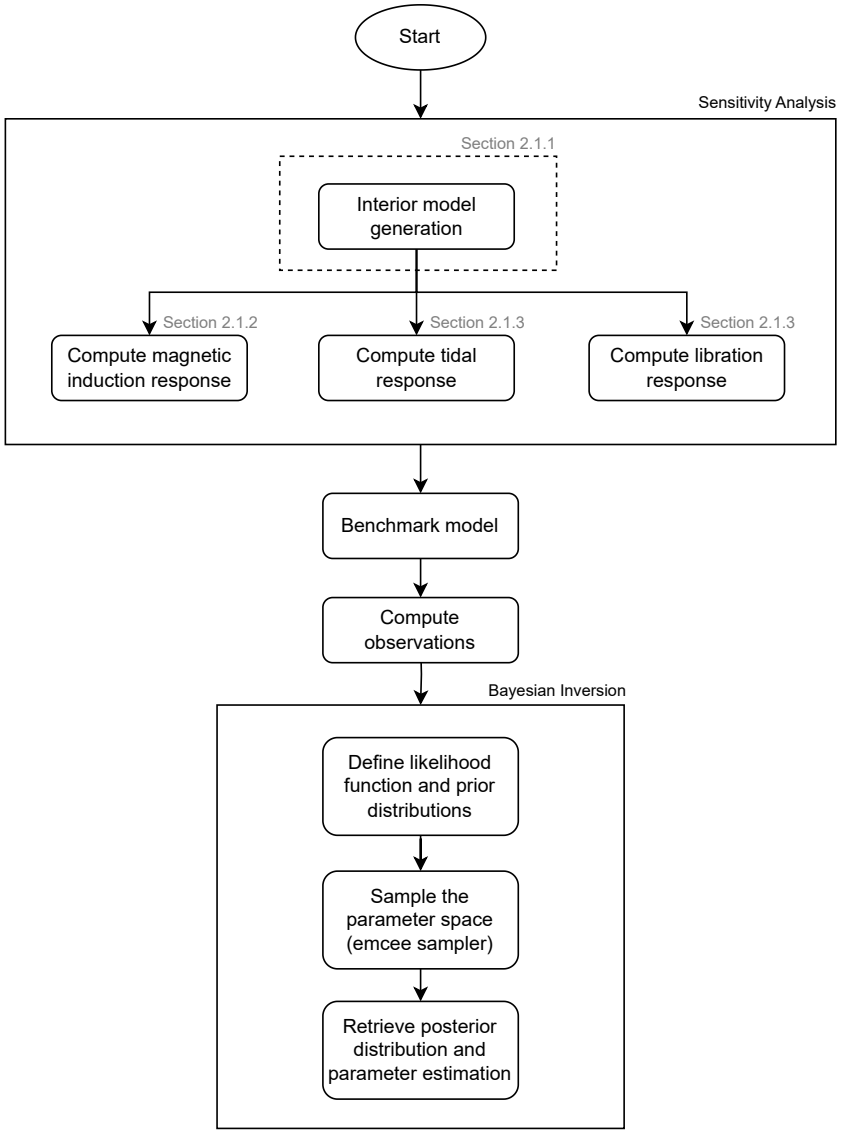

Figure 2.5: Flowchart showing methodology of the project.

3

Sensitivity Analysis

This chapter presents the results of the sensitivity analysis performed on the interior model parameters. We first perform a one-at-a-time (OAT) sensitivity analysis, where we vary one parameter at a time while keeping the others fixed. This allows us not only to understand how each parameter influences the different observations, but also how the applied constraints on the interior model influence the feasible ranges of the constrained parameters.

We then perform a full MC analysis, where we vary all the parameters simultaneously. This analysis shows the combined effects of all parameters on the model's response, and reveals the degeneracies between the interior parameters. Since the OAT analysis serves to illustrate simple underlying trends and produces results consistent with those of the full MC analysis, it is included in the appendix (section D.1) for completeness. In this chapter, we focus on the results of the MC analysis.

The general setup is described in section 2.1 and the parameters are sampled in the ranges defined in Table 2.1 from log-uniform distributions for the shear moduli and viscosities, and uniform distributions for the other parameters. The responses are computed for each valid interior model. Section 3.1 discusses the choice of sample size, section 3.2 examines the effect of the imposed constraints on Ganymede's interior model, and section 3.3 analyzes the influence of all parameters on the different observables.

3.1. Sample Size Analysis

In this section, we determine an appropriate sample size for the MC analysis. This is necessary to ensure that the simulation includes enough samples to capture the trends and properly explore the parameter space. The selection is performed in two steps. First, we analyze the number of samples needed to achieve a good sampling of each parameter if they were varied independently. Second, we analyze the discrepancy δ of the sampling, which is an indication of how well the samples fill the design space, when all parameters are varied concurrently.

The first step involves sampling the different parameters within their prescribed ranges. We vary the number of samples between 1×10^3 and 4×10^5, as illustrated on the x-axis of Figure 3.1. For each parameter and each sample size, we compute the mean η and standard deviation σ of the sampled values. Since the parameters are assumed to follow uniform distributions, these distributions have known theoretical mean η_{th} and standard deviation σ_{th}. The sample size is considered sufficient when the computed mean and standard deviation for each parameter approach their respective theoretical values.

For the parameters sampled from a log-uniform distribution, the sampling is performed uniformly over the range $[\log_{10}(a), \log_{10}(b)]$. Instead of converting the sampled values back to the original scale, we compute the mean and standard deviation of the sampled values, and then compare them to the theoretical mean and standard deviation of a uniform distribution in the logarithmic scale.

We define the acceptance interval as $\text{AI}_x = |0.01x - x|$, where x is either η_{th} or σ_{th}. We consider the number of samples to be sufficient if η and σ converge to the theoretical values within $\pm$AI. Since we

are not interested in the behavior of each decision variable specifically, η and σ are normalized according to Equation 3.1 and plotted together with the same color in Figure 3.1.

$$\bar{\eta} = \frac{\eta - \eta_{\text{th}}}{\text{AI}_\eta} \qquad \bar{\sigma} = \frac{\sigma - \sigma_{\text{th}}}{\text{AI}_\sigma} \tag{3.1}$$

From Figure 3.1, all the values enter the AI at around 1×10^4 samples, which we consider sufficient to achieve a good sampling of the design space for each parameter independently.

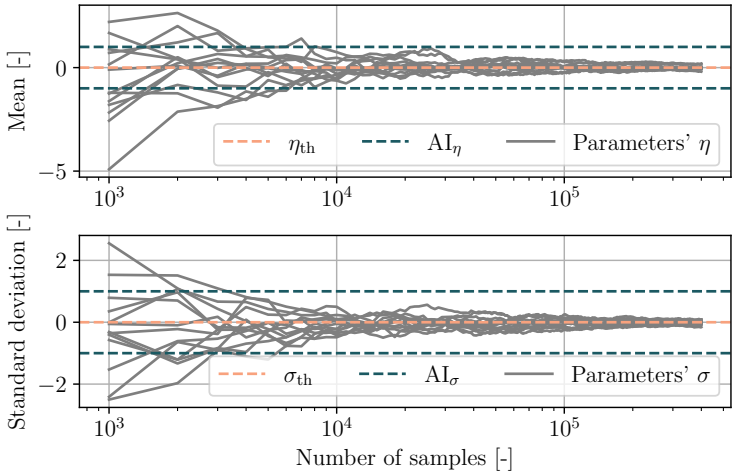

Figure 3.1: Normalized η and σ for all the sampled parameters. The values are normalized according to Equation 3.1.

The second step is performed by analyzing the discrepancy δ of the sampling. To achieve this, the `scipy.stats` Python package is used (Virtanen et al., 2020). 40×10^4 samples are generated. Then, for different numbers of samples, the discrepancy is computed. The results are shown in Figure 3.2. The lower the discrepancy is, the better the variables sample the design space. Since we have 13 decision variables, we consider the discrepancy of 1×10^4, 13×10^4, 26×10^4 and 39×10^4 samples, and the values of δ for specific sizes are reported in Table 3.1.

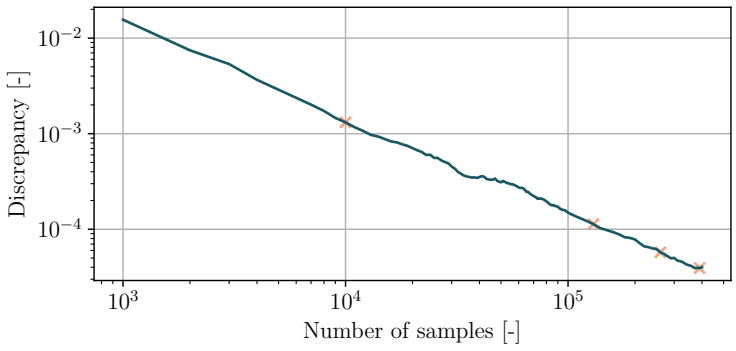

Figure 3.2: Discrepancy values for different sample sizes. The markers indicate the values of δ for the sample sizes of interest.

Table 3.1: Discrepancy values and variation in percent for different sample sizes.

δ_1	δ_{13}	δ_{26}	δ_{39}	$\frac{\lvert\delta_{13}-\delta_1\rvert}{\delta_1} \times 100$	$\frac{\lvert\delta_{26}-\delta_{13}\rvert}{\delta_{13}} \times 100$	$\frac{\lvert\delta_{39}-\delta_{26}\rvert}{\delta_{26}} \times 100$
1.3147×10^{-3}	1.1314×10^{-4}	5.7473×10^{-5}	3.9326×10^{-5}	256.36 %	49.20 %	31.57 %

The value obtained with 1×10^4 samples can be significantly improved with a sample size of 13×10^4. Further increasing it to 26×10^4 reduces the discrepancy by 49.20 %, and to 39×10^4 by an additional 31.57 %. However, the CPU time increases substantially with the number of samples. Therefore, we consider a sample size of 13×10^4 to be sufficient to achieve a good sampling of the design space. This number only includes the valid models for which the responses are computed.

3.2. Constrained Parameters

Due to the high number of parameters involved, it is important to analyze the interdependencies between variables to better understand their impact on the responses. This analysis ensures that the interior model behaves as expected and is internally consistent. A statistical correlation analysis is performed using the `pandas.DataFrame` Python package (The pandas development team, 2025). It allows to compute the correlation between different variables according to one of the available methods, which include the Pearson, Kendall and Spearman correlation methods. The Pearson method measures linear correlation between two variables, while the Kendall and Spearman methods are non-parametric methods that relate the rank values of the variables. The rank of a value refers to its position in the ordered list of all values of that variable, from smallest to largest. Specifically, the Spearman correlation measures how well two parameters follow a monotonic relationship. It is equivalent to using the Pearson correlation on the rank values of the variables. The Kendall method assesses the agreement between the rankings of variables by considering concordant and discordant pairs. A concordant (discordant) pair is a pair of observations where the ranks for both variables are in the same (different) order (The pandas development team, 2025). The Spearman and Kendall coefficients show the same behavior, but Spearman has usually higher values than Kendall for the same data set. In the following analysis, the Kendall method is used.

Figure 3.3 shows the correlation matrix between the free and constrained parameters. The MoI factor is added to the list of parameters even though it is not explicitly a free parameter because, in order to compute ρ_c and ρ_{ma} from Equation 2.6 and Equation 2.7, the mass and MoI of Ganymede are sampled from a Gaussian distribution. Therefore, different values of the MoI are used for each model, affecting the constrained parameters as well. The mass is not included in the matrix because it was seen to not have an influence on the parameters.

Values close to 1 or -1 indicate a strong correlation: positive values imply that the two parameters tend to increase or decrease together, while negative values suggest that one parameter increases as the other decreases. Values close to 0 indicate a weak correlation, meaning that the behavior of the two parameters is largely independent. It is important to note that correlation does not imply causation. Even if two parameters are correlated, this does not necessarily mean that one causes the other to change. These results should be interpreted alongside the imposed constraints described in subsection 2.1.1. For example, we know from Equation 2.1 that κ_o is directly derived from wt, which explains the coefficient of 1 between them. In contrast, it is not related to r_{ma}, even though they show a correlation of -0.22. This negative correlation can instead be interpreted as a tendency for models with a larger mantle radius to have a lower ocean density to satisfy Ganymede's mass and MoI constraints, which in turn leads to a lower ocean conductivity. This example highlights the hidden dependencies among the parameters, all of which contribute to the model responses.

We now analyze how the constrained parameters, computed according to subsection 2.1.1, vary with changes in the free parameters. As shown in Figure 3.3, the MoI factor affects the innermost layers, while the total mass has no significant influence, highlighting the importance of accounting for the MoI value. Figure 3.4 shows one-dimensional histograms of the deep interior parameters on the diagonal and two-dimensional joint distributions off-diagonal, with the MoI included to illustrate its influence. The two-dimensional histograms reflect the trends observed in the OAT sensitivity analysis (Figure D.1, Figure D.2). The most evident trends are the negative correlations between core radius and core density, core radius and mantle density, and mantle radius and mantle density, where one decreases as the other increases to satisfy the MoI constraint. In contrast, the positive correlation between core density and mantle radius is less pronounced than in the OAT analysis: for a given mantle radius, nearly all core density values remain plausible, as indicated by the uniform distribution of models along the corresponding vertical line.

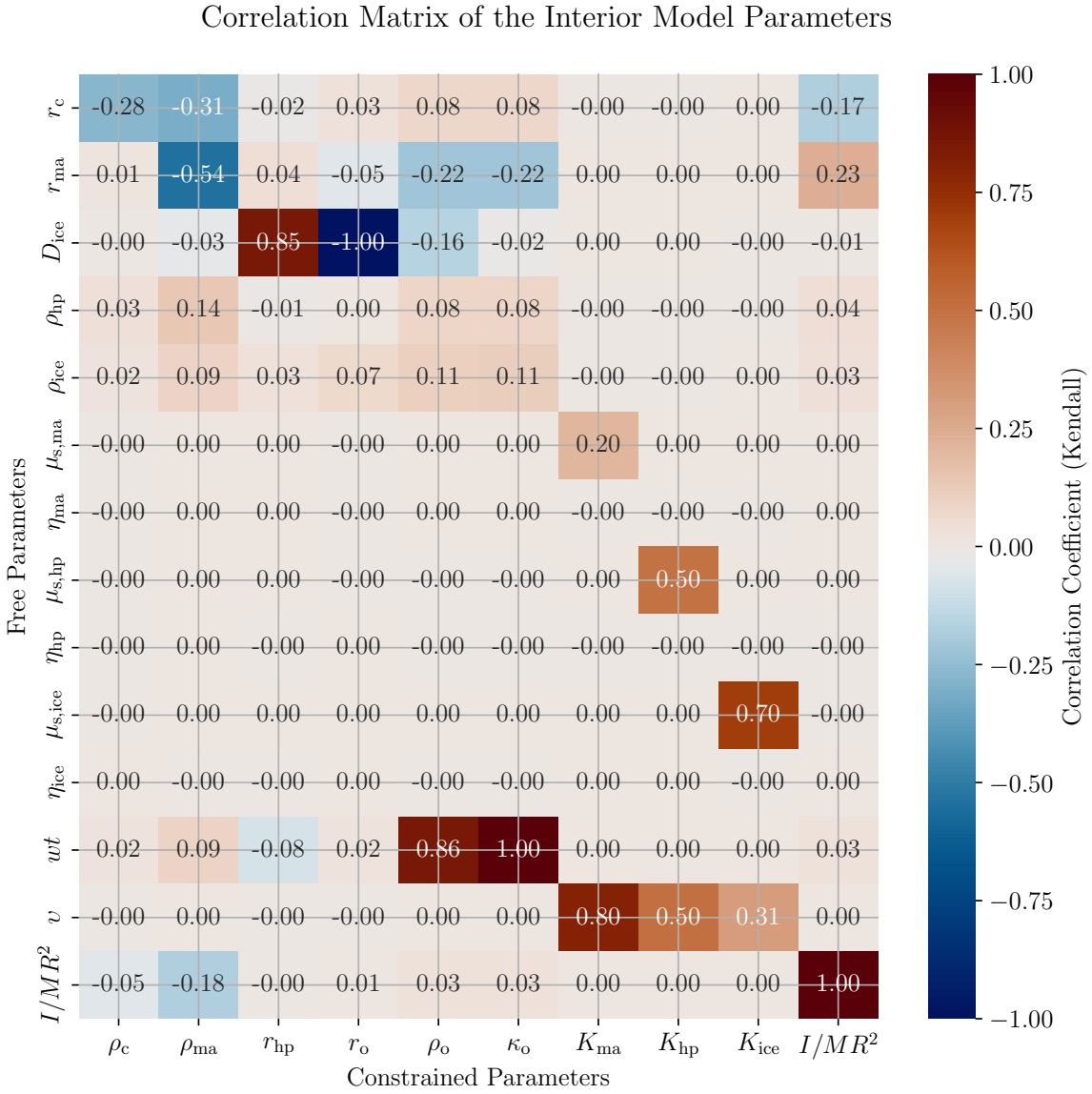

Figure 3.3: Kendall correlation coefficients between the free and constrained parameters. The MoI factor is added to visualize its effect of this constraint on the parameters.

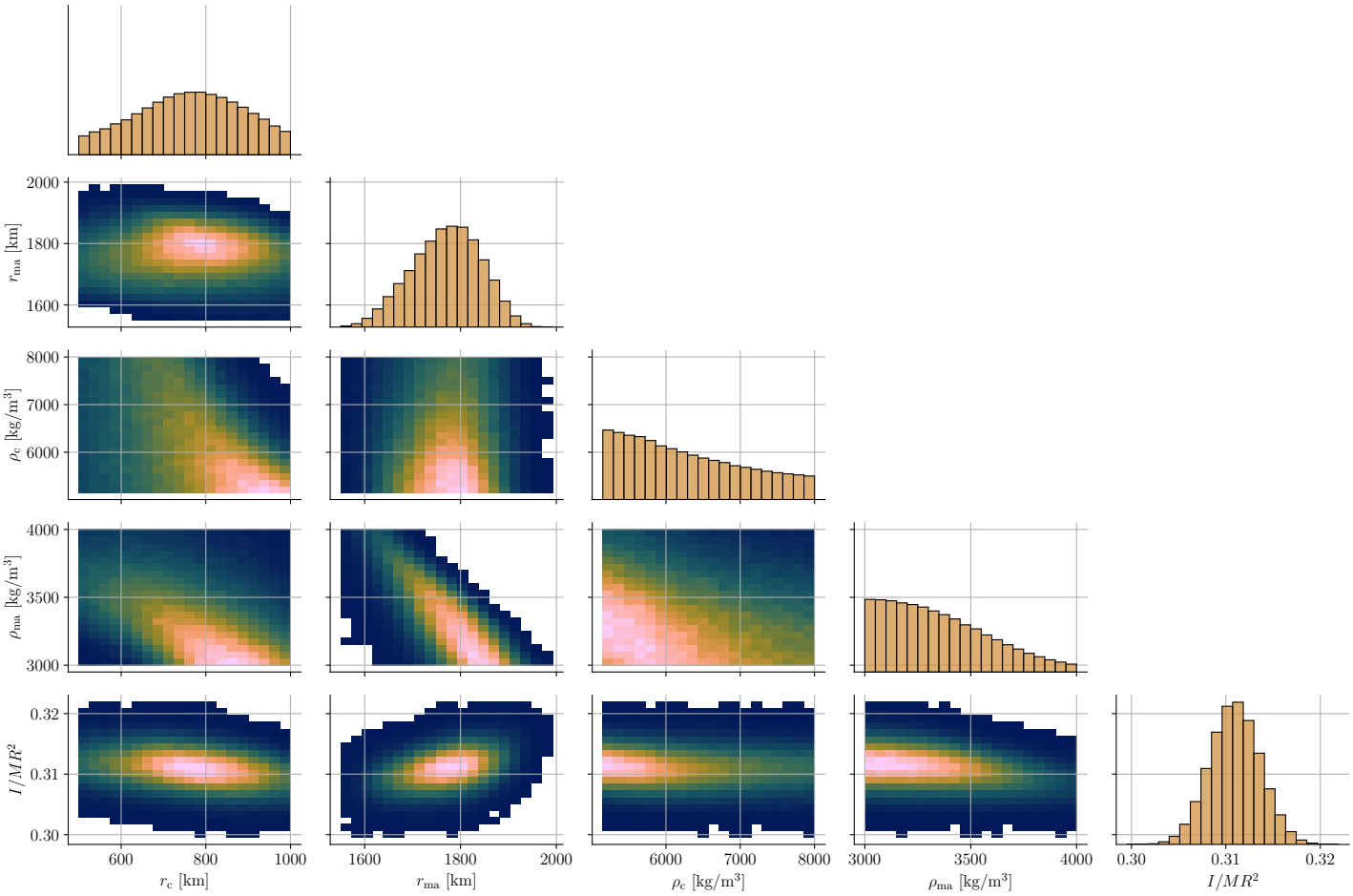

Figure 3.4: Corner plot showing the parameter distributions and correlations, with the MoI included to illustrate the influence of the static gravity constraint on the interior structure. The diagonal panels show one-dimensional histograms for each parameter, while the off-diagonal panels display the two-dimensional joint distributions. They do not represent posterior probability distributions, since no likelihood function or Bayesian inversion is applied. The color scale in the 2D plots reflects the density of the samples, with lighter colors indicating higher density regions.

Compared to the OAT sensitivity analysis, where the dependencies appeared as one-to-one correspondences between parameters, introducing MoI variations and varying all parameters simultaneously broadens the parameter distribution. This widens the range of valid models and reveals preferred parameter values. For instance, models with MoI values close to the nominal value typically have mantle radii in the range of approximately 1700 km to 1900 km. This highlights how observational constraints can help in the estimation of certain parameters. Thus, the MoI factor will be incorporated as an observational constraint in the Bayesian inversion.

Figure 3.5 shows the two-dimensional histograms of the hydrosphere parameters. The trends observed in the OAT sensitivity analysis are overall maintained, and the same considerations regarding the simultaneous variation of parameters apply here and explain the broad distributions. For example, for a given ice shell thickness, a wide range of ocean densities is possible depending on the composition. The

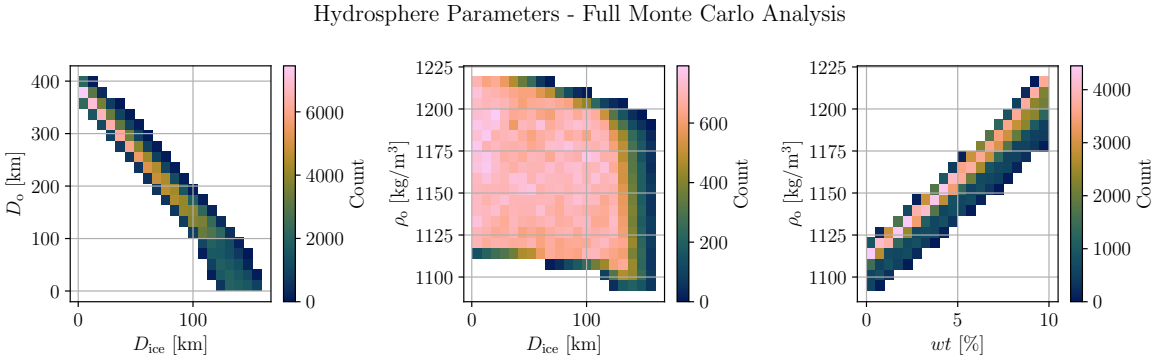

Figure 3.5: Two-dimensional histograms of the hydrosphere parameters. On the x axis the variables that show correlation are reported.

ocean thickness is determined from the phase diagram, and from Figure 2.2 it is clear that it decreases with increasing ice shell thickness (e. g., with increasing pressure at the ice-ocean interface). Since the ice shell thickness also defines the ocean's pressure profile, it influences the ocean density. However, the dominant factor controlling the ocean density is its composition, which directly affects the phase diagrams and, consequently, the ocean parameters.

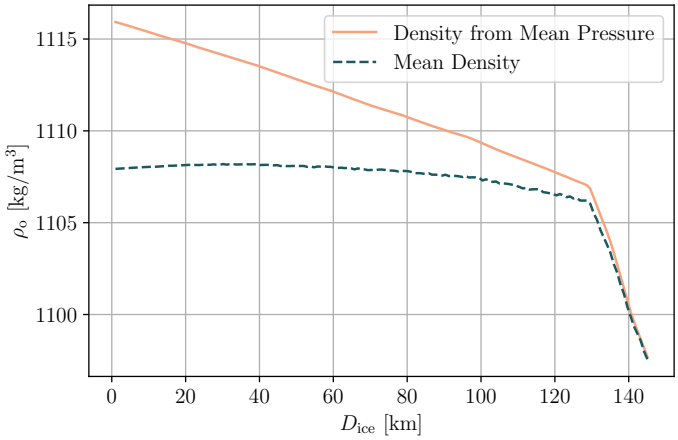

Figure 3.6: Ocean density as a function of the ocean thickness with $wt = 0\%$ for the two approaches: using the mean pressure and using the depth-dependent density.

The ocean density is defined by the EOS of the ocean, which depends on its composition, pressure and temperature. In this study, the temperature is assumed to remain constant within the ocean, while pressure varies with depth. However, we assume that each layer has a constant density, and we use the average pressure of the ocean to compute it. A more accurate approach would involve computing the ocean density as a function of depth, then using this depth-dependent density to compute the

mass and pressure profiles within the layer, and iterating the procedure until convergence. Figure 3.6 shows the ocean density as a function of ocean thickness for both approaches, using a composition of pure water, which yields the largest density difference between the two methods. The results indicate that the two approaches can differ by up to approximately $8\,\mathrm{kg\,m^{-3}}$, corresponding to about 0.7 % of the ocean density currently computed using the mean pressure. Although this difference is relatively small, ocean density is expected to influence the real part of the tidal Love numbers. Thus, even a minor change in density may lead to noticeable changes in the tidal response. However, computing the depth-dependent density requires interpolating pressure, temperature, and composition at each depth, which is computationally expensive. Additionally, we expect a thick ice shell from magnetic induction measurements (Kivelson et al., 2002), where the discrepancy between the two methods is less significant. Therefore, we choose to compute the ocean density using the mean pressure, as it is a good balance between accuracy and computational efficiency.

Figure 3.7 shows the two-dimensional histograms of the mechanical properties of the layers. These trends are expected, as their dependence is defined by Equation 2.8, and they are similar to those obtained in the OAT sensitivity analysis (Figure D.5).

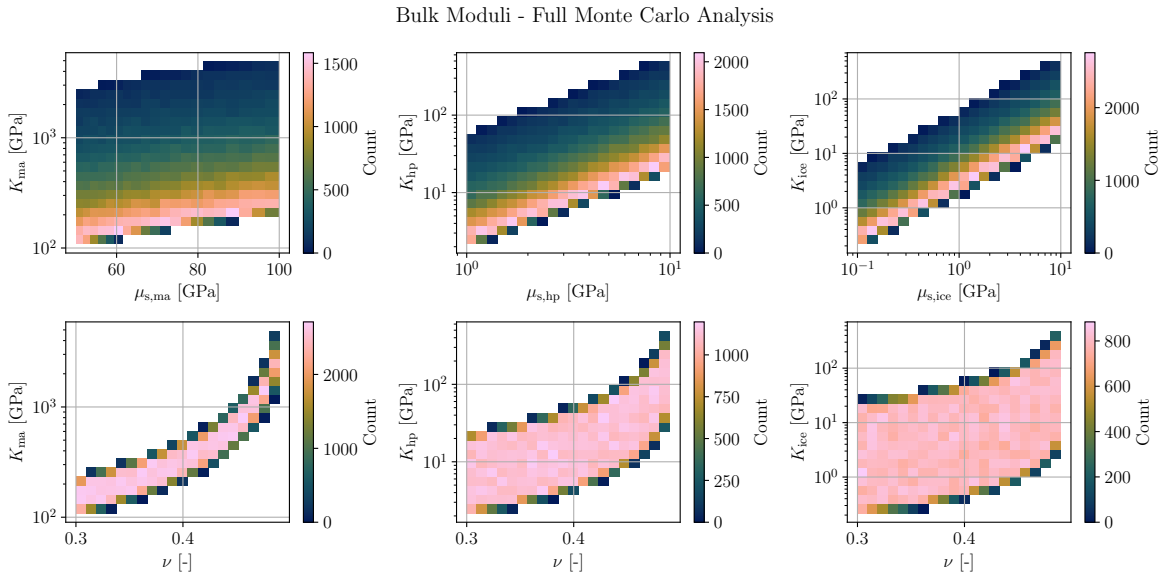

Figure 3.7: Two-dimensional histograms of the bulk moduli. On the x axis the variables that show correlation are reported.

All of the above-mentioned dependencies are important for interpreting the behavior of the resulting observations, as one trend may hide the influence of another parameter. Recognizing them can serve as a guide for better understanding how the responses change with interior parameters.

3.3. Observations

In this section, we analyze the magnetic induction, tidal and libration responses of the valid interior models. As explained in section 3.2, a correlation matrix between the model parameters and the responses is used to analyze the major contributors to the different observables. Figure 3.8 shows the Kendall correlation coefficients between the model parameters and the responses. This table is useful to identify the parameters that have the strongest influence on the responses and select the most relevant ones for further analysis.

3.3.1. Magnetic Induction Response

The magnetic induction amplitude is the most straightforward response to analyze, since it is defined by the analytical expression in Equation 2.9. In this study, we assume a uniform excitation field from

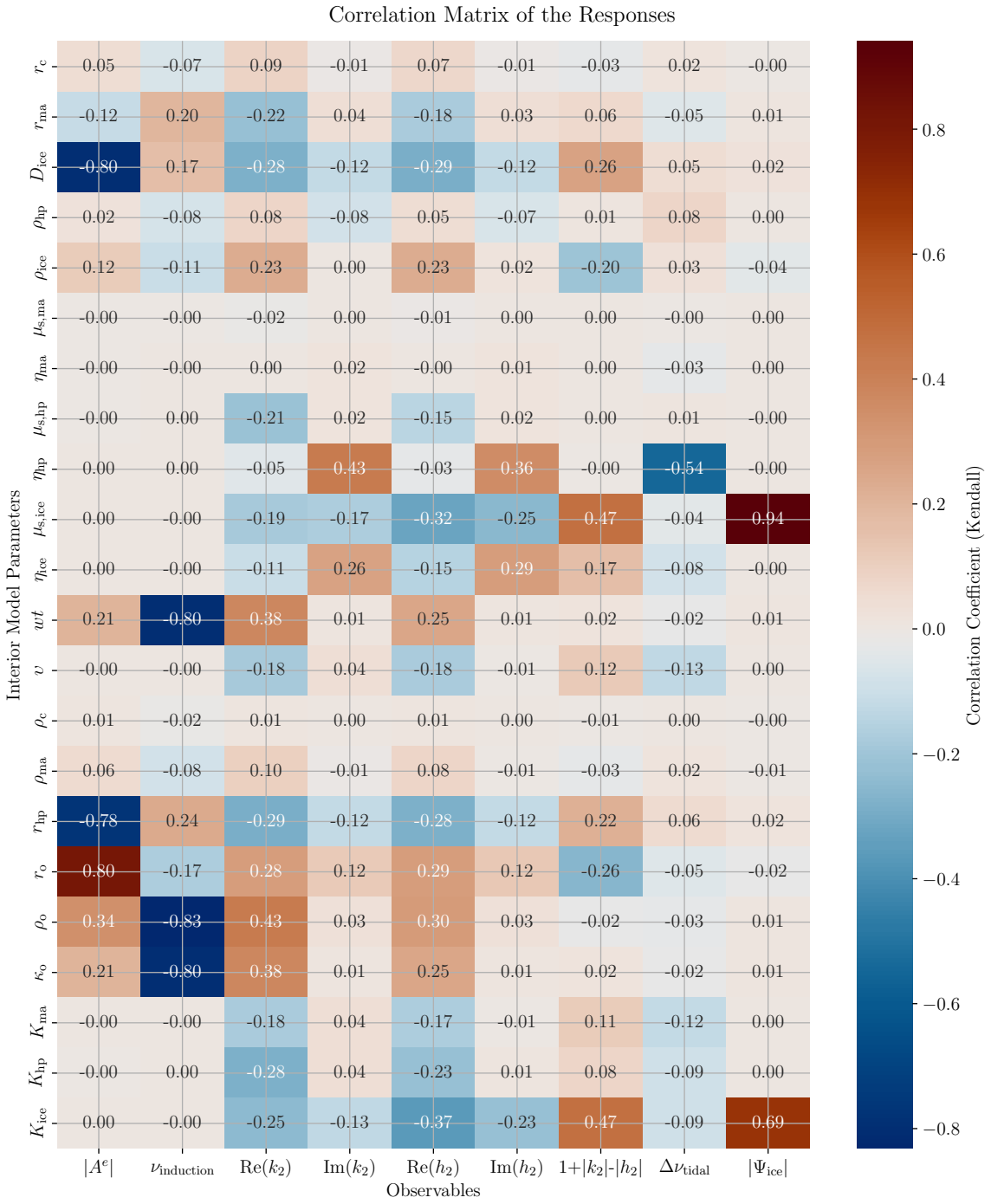

Figure 3.8: Kendall correlation coefficients between the model parameters and the responses. The responses that are shown on the horizontal axis are, from the left to the right: the amplitude and phase lag of the magnetic induction response, the real and imaginary parts of k_2 and h_2, a linear combination of k_2 and h_2, the difference of the tidal phase lag, and the libration amplitude of the shell.

Jupiter, a single, uniform, and spherically symmetric conducting layer inside Ganymede, and an inducing period of 10.53 h, corresponding to Jupiter's synodic period (Vance et al., 2021). The complex magnetic induction response can be analyzed in terms of amplitude and phase lag. Specifically, the normalized amplitude ranges from 0 to 1, with 0 indicating no induction and 1 indicating a perfectly conducting sphere. This parameter can then be used to obtain the internally induced magnetic field due to a time-varying external magnetic field (Vance et al., 2021, Supporting Information).

In the following analysis, only the magnetic induction amplitude is considered. The analysis of Galileo flybys performed by Kivelson et al. (2002) did not include the phase lag, as it was expected to be small and therefore undetectable with the available data. Additionally, according to Seufert et al. (2011) and Vance et al. (2021), the phase lag provides information similar to that of the amplitude. However, Seufert et al. (2011) analyzed the magnetic induction response of the Galilean moons using a more comprehensive model that incorporated not only Jupiter's magnetic field, but also the current sheet and magnetopause fields. Their model also accounted for mutual induction between different conducting layers, such as the ocean and the core. In this context, Seufert et al. (2011) showed that the phase lag can reveal interactions between the conducting layers, highlighting the importance of future phase lag measurements.

From the analytical formulation (Equation 2.9) and the OAT sensitivity analysis (subsection D.1.3), we expect it to vary with the ocean thickness and composition, which is indeed seen in Figure 3.8, with a stronger contribution from the ocean thickness. Vance et al. (2021) showed that the role of ocean conductivity becomes more significant at longer induction periods. Additionally, other parameters show a correlation with the magnetic induction response. Although the ice shell density is not directly involved in the analytical formulation, it influences ocean thickness through Equation 2.2. Instead, the correlation with the ocean density can be traced back to both the ocean composition and the ice shell thickness, which determines the pressure profile within the ocean and, consequently, its mean pressure used to compute the density. The magnetic induction response could therefore help constrain the ocean density.

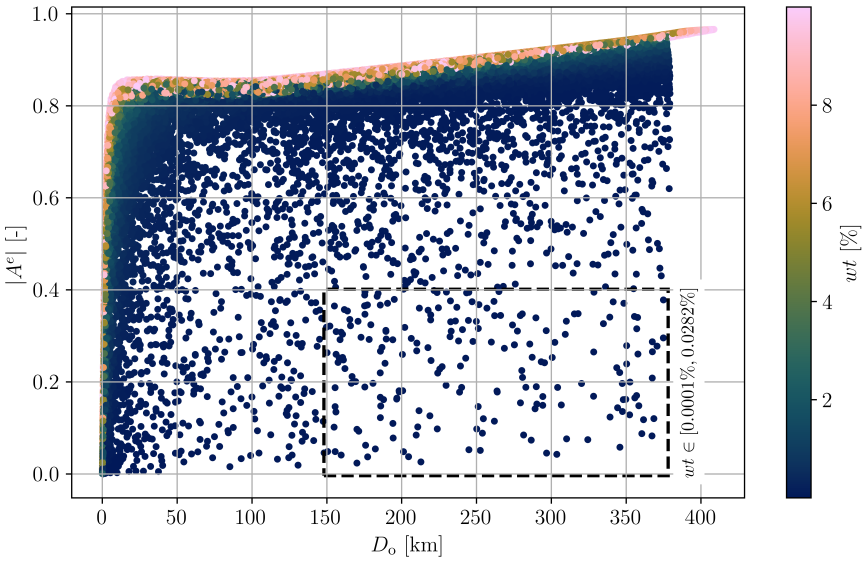

Figure 3.9: Amplitude of the magnetic induction response as a function of the ocean thickness and composition. The range of wt of $MgSO_4$ in the ocean is indicated for the models within the area bounded by the dashed lines.

Figure 3.9 shows the magnetic induction response as a function of the ocean thickness for different ocean compositions. The general trend is in agreement with the OAT analysis shown in Figure D.6, but for a fixed ice shell thickness, the magnetic induction amplitude increases with increasing wt of $MgSO_4$ in the ocean, due to a higher ocean conductivity. Thin oceans can have a strong magnetic induction response if they contain a high wt of $MgSO_4$, which leads to high ocean conductivities. On the other hand, the same induction response can be achieved with a thicker ocean if the wt is low, highlighting the

trade-off between these two parameters. As shown in the highlighted region of Figure 3.9, low induction amplitudes at high ocean thicknesses correspond to ocean compositions close to pure water, where wt falls within the annotated range.

Figure 3.10 illustrates the number of models sampled for each ice shell thickness that results in a given magnetic induction amplitude. A higher model count indicates that the corresponding combination of ice shell thickness and induction amplitude is more frequently represented in the design space, suggesting a greater likelihood of occurrence. According to Figure 3.10, Ganymede's magnetic induction amplitude is most likely between 0.8 and 1.0, a range that includes the value of 0.84 reported by Kivelson et al. (2002) from the analysis of magnetic induction data.

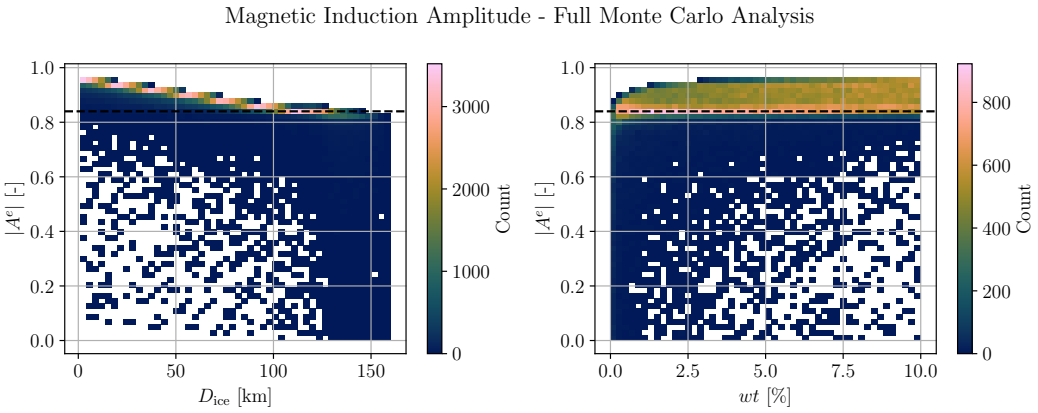

Figure 3.10: Two-dimensional histogram of the magnetic induction amplitude as a function of the ice shell thickness (left) and ocean composition (right). The black dotted line indicates the value of $|A^e| = 0.84$ found by Kivelson et al. (2002).

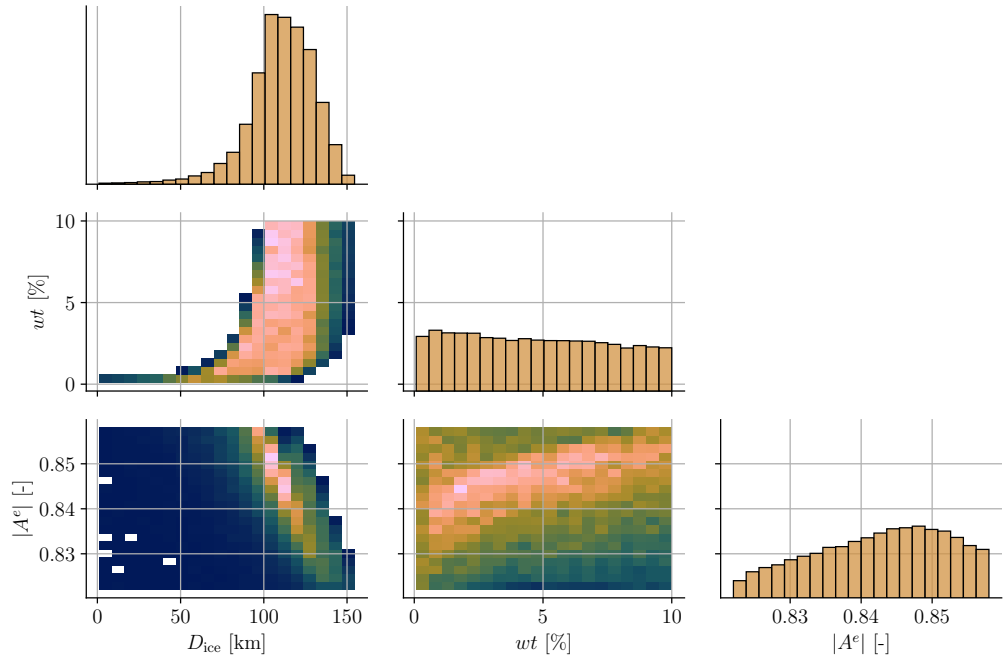

Figure 3.11: Corner plot showing the parameter distributions (diagonal panels) and correlations (off-diagonal panels) for the models consistent with a magnetic induction amplitude of 0.84 ± 0.018 (Kivelson et al., 2002). The distributions do not represent posterior probabilities, since no likelihood function or Bayesian inversion is applied. The color scale in the 2D plots reflects the density of the samples, with lighter colors indicating higher density regions.

Figure 3.11 shows two-dimensional histograms of the ice shell thickness and ocean composition for the models that are consistent with the magnetic induction response from Kivelson et al. (2002). Among all

the models, those consistent with the induction response tend to have a thicker ice shell. However, no particular trend is observed for the ocean composition. This suggests that a Bayesian inversion using the magnetic induction response could help constrain the ice shell thickness, but not the ocean composition.

3.3.2. Tidal Response

The tidal response is analyzed in terms of the Love numbers k_2 and h_2, and specifically their real and imaginary parts, which can provide constraints on Ganymede's hydrosphere (Van Hoolst et al., 2024). The real part of the Love numbers is related to elastic effects, while the imaginary part mirrors the viscous response of the body and its tidal dissipation. Therefore, the mechanical properties of the layers, such as rigidity and viscosity, play a crucial role in determining the tidal response.

The tidal response of Ganymede, which is expected to be stronger in the presence of a subsurface ocean, is primarily influenced by the ice shell thickness, ocean density, and ice shell density, and to a lesser extent by the deep interior parameters (Van Hoolst et al., 2024). Additionally, the rigidities and viscosities of the ice layers play a significant role in the tidal response, as the Love numbers are mostly sensitive to the viscoelastic properties of the external layers.

Figure 3.12 shows the two-dimensional histograms of the real part of k_2. Similar trends are observed for the real part of h_2, shown in Figure D.11, and the discussion applies to both Love numbers. The figures illustrate the sensitivity of the tidal Love numbers to key structural and rheological parameters. Overall, the trends are in agreement with the ones observed in the OAT sensitivity analysis, but this analysis offers a more comprehensive view of the interactions and degeneracies between the parameters.

The real part of k_2 is sensitive to the presence of a subsurface ocean and its properties (Jara-Orué et al., 2016; Moore et al., 2003), as well as to the thickness and mechanical properties of the overlying ice shell (Kamata et al., 2016; Moore et al., 2003). One of the most evident trends is the negative correlation between ice shell thickness and $\mathrm{Re}(k_2)$. Thicker shells lead to smaller deformations, and thus to lower values of k_2, as the shell becomes more resistant to tidal deformations and reduces the moon's ability to respond to tidal forces. This trend has already been confirmed by previous studies (Jara-Orué et al., 2016; Kamata et al., 2016; Steinbrügge et al., 2015; Wahr et al., 2006).

However, this dependence is not isolated from other parameters. Low values of $\mathrm{Re}(k_2)$ are observed only for thick ice shells, but high values can be found for both thin and thick shells, highlighting the influence of other parameters. As previous studies have pointed out, the tidal response of a decoupled ice shell is not governed by its thickness alone, but rather by the product of thickness and shear modulus (Steinbrügge et al., 2015; Wahr et al., 2006). This coupling introduces a significant degeneracy: a thin but rigid shell can produce a similar $\mathrm{Re}(k_2)$ as a thick but soft one. As a result, it is difficult to constrain ice thickness or rigidity independently based on k_2 alone.

To break these degeneracies, a promising approach is to combine measurements of k_2 with those of the radial displacement Love number h_2. In the case of a fully fluid response, the difference $h_2 - k_2$ equals 1, while in viscoelastic regimes this value decreases (Moore et al., 2000). Moreover, according to Moore et al. (2000), the amplitude of tidal deformations scales linearly with the thickness of the ice shells, with the slope of this relationship governed by its rigidity. However, Wahr et al. (2006) highlighted that due to uncertainties in the physical properties of the ocean and mantle, it is challenging to isolate this linear trend using measurements of k_2 or h_2 alone. Wahr et al. (2006) investigated Europa's tidal deformation and found that $1 + |k_2| - |h_2|$ varies linearly with the product of ice shell thickness and rigidity, a relationship later confirmed for Ganymede by Steinbrügge et al. (2015). This linear combination is particularly informative because it approaches zero as the ice shell tends to zero, while the Love numbers k_2 and h_2 considered individually do not (Wahr et al., 2006).

Kamata et al. (2016) also showed that $1 + |k_2| - |h_2|$ varies linearly with the thickness of the ice shells, with the slope of this relationship governed by its rigidity. This behavior can also be seen in Figure 3.13, which shows that varying the rigidity alters the value of $1 + |k_2| - |h_2|$ for a fixed value of the ice shell thickness. Therefore, the linear combination $1 + |k_2| - |h_2|$ might constrain the product of shell thickness and shear modulus (Steinbrügge et al., 2015; Wahr et al., 2006). Additionally, constraining the ice shell rigidity could help to narrow the uncertainty in the ice shell thickness through measurements of the Love numbers.

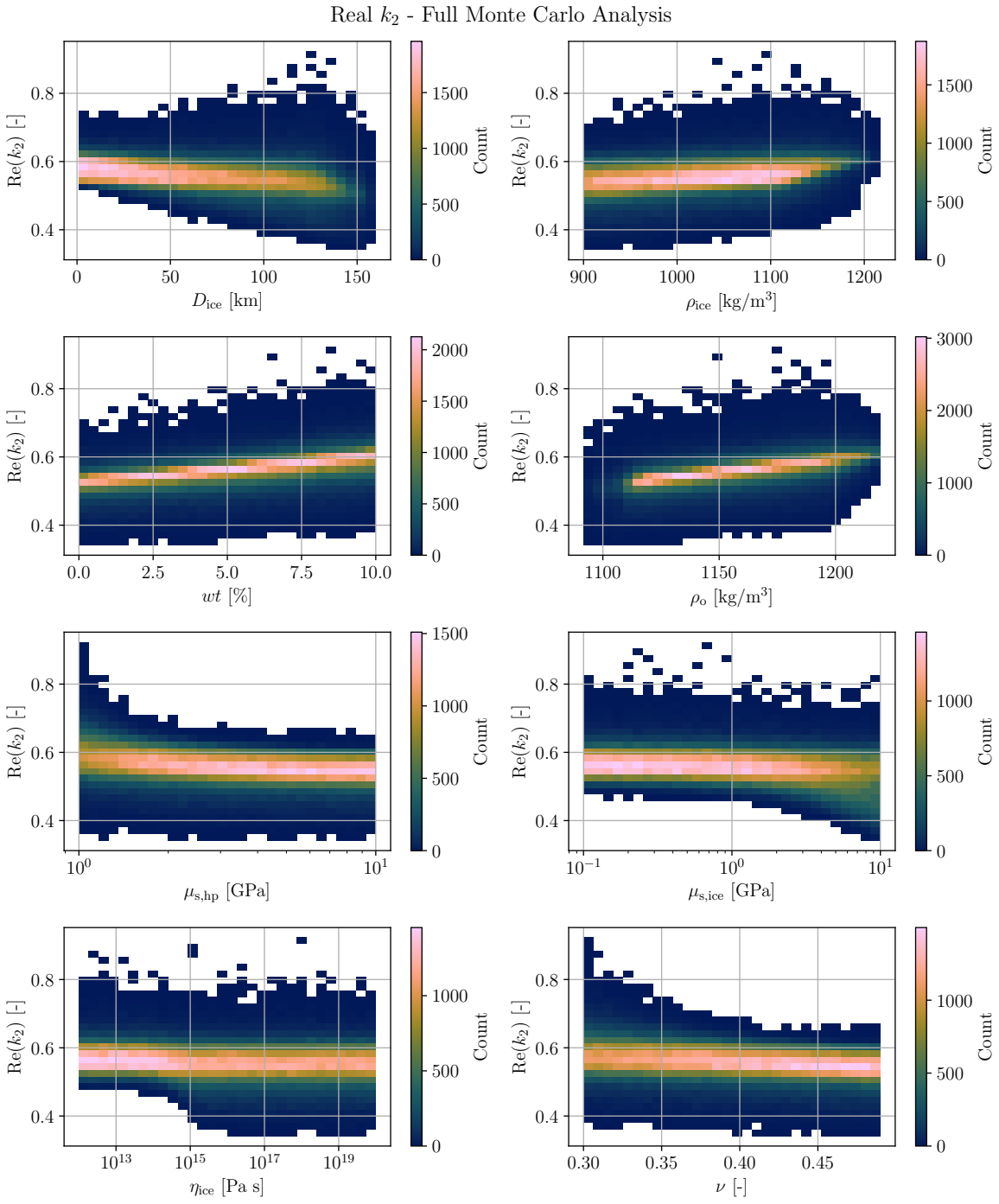

Figure 3.12: Two-dimensional histogram of the real part of k_2 as a function of the selected free parameters.

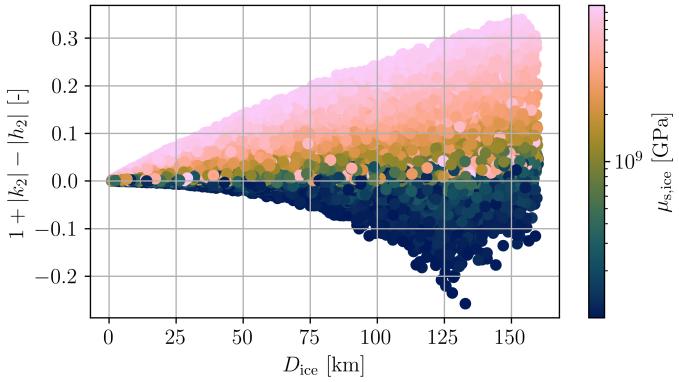

Figure 3.13: $1 + |k_2| - |h_2|$ as a function of the ice shell thickness and shear modulus.

Another key trend is the dependence of the $\text{Re}(k_2)$ on the ice shell viscosity, which resembles the transition from a fluid-like regime at low viscosities to an elastic regime at high viscosities (Moore et al., 2003), as also seen in the OAT sensitivity analysis. It is also worth highlighting the dependence of the Love numbers on the Poisson's ratio, and therefore on the bulk moduli of the layers. Figure 3.12 shows that $\text{Re}(k_2)$ decreases with decreasing compressibility of the layers. In the majority of studies, compressibility is neglected (e. g., Hussmann et al. (2016), Jara-Orué et al. (2016), and Moore et al. (2003)). However, Dobrovolskis (1990) showed that including compressibility in the computation of the stress tensor of a homogeneous and elastic sphere changes the internal stress distribution by several percent compared to incompressible models. Beuthe (2015) developed a "massive membrane approach" to include crust compressibility when modeling the tidal response of icy moons. The results showed that compressible models yield larger Love numbers than incompressible models, with the difference increasing with the ice shell thickness (Beuthe, 2015).

Lastly, ocean properties also play a noticeable role. Higher ocean densities, which result from higher salinity values, increase the density contrast between the ice shell and the ocean. When the body deforms, a larger density contrast leads to a more significant mass redistribution, which in turn produces a greater change in the gravitational field, and consequently a higher value of $\text{Re}(k_2)$.

Figure 3.14 shows the two-dimensional histograms of the imaginary part of k_2. Due to the similar behavior of the Love numbers, we will comment on k_2 only, but analogous conclusions can be drawn for h_2 (see Figure D.12). Similarly to $\text{Re}(k_2)$, the trends are in agreement with the ones observed in the OAT sensitivity analysis. The sensitivity of the imaginary part of k_2 to ice shell viscosity provides valuable insight into Ganymede's viscoelastic behavior, as illustrated in the bottom-left subplot of Figure 3.14. This behavior resembles the one observed in Figure D.9 and can be explained by the Maxwell rheological model, in which the material is idealized as a purely elastic spring with shear modulus μ_{s} and a purely viscous dashpot with viscosity η connected in series (Tobie et al., 2025). The characteristic timescale separating viscous and elastic behavior is the Maxwell time, defined as:

$$\tau_M = \frac{\mu_{\text{s}}}{\eta}. \tag{3.2}$$

When the tidal forcing period is much longer than the Maxwell time, the dashpot dominates and the shell deforms viscously. When the tidal forcing period is much smaller than the Maxwell time, the spring dominates and the response is elastic. For forcing periods comparable to the Maxwell time, the imaginary part of the Love numbers reaches a maximum, indicating peak energy dissipation (Tobie et al., 2025). The location and amplitude of this dissipation peak depend on both μ_{s} and η, and here occurs between $\eta_{\text{ice}} = 10^{13}$ Pa s and $\eta_{\text{ice}} = 10^{15}$ Pa s.

Figure 3.15 shows the tidal phase lag difference as a function of the HP ice and ice shell viscosities. The phase lag is defined as $\nu_{k_2} = \tan^{-1}(\text{Im}(k_2)/\text{Re}(k_2))$. Hussmann et al. (2016) used this quantity to investigate Ganymede's dissipation and showed that the phase lag difference is dominated by dissipation in the HP ice layer rather than the ice I shell (Hussmann et al., 2016, Figure 2(c) and Figure 3).

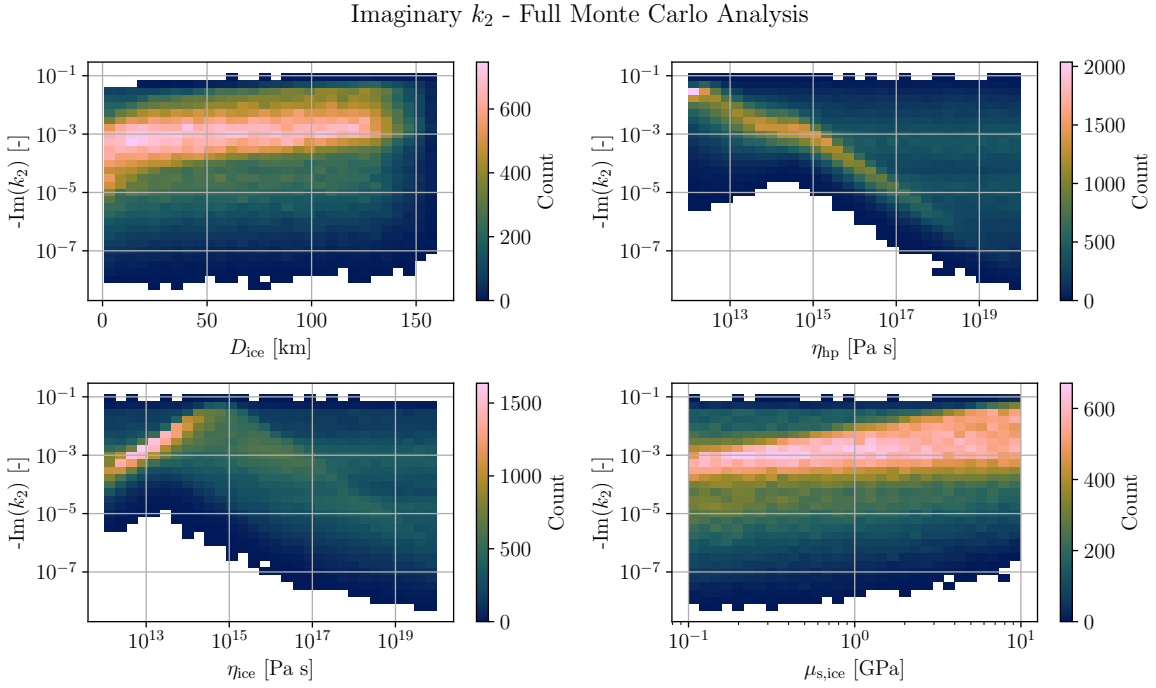

Figure 3.14: Two-dimensional histogram of the imaginary part of k_2 as a function of selected free parameters. A negative sign is applied to $\text{Im}(k_2)$ to allow plotting on a logarithmic scale.

Depending on the model parameters, the phase lag difference peaks at a certain value of HP ice viscosity, which occurs here at below 1×10^{14} Pa s. The dependence on the ice shell viscosity is weaker, and two distinct regions can be identified: one for negative phase lag values, which are associated with very low η_{ice} values, and the other for $\eta_{\text{hp}} > 10^{15}$ Pa s, where an area of η_{ice} values around 10^{15} Pa s is visible in dark green. Phase lag measurements could therefore help constrain the viscosity of the HP ice layer.

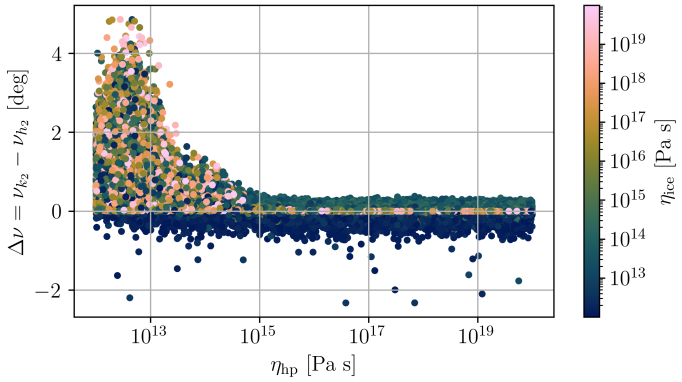

Figure 3.15: Tidal phase lag difference as a function of the high-pressure ice. The color scale indicates the ice shell viscosity.

3.3.3. Libration Response

The libration response is computed using the method described in subsection 2.1.4 and analyzed in terms of the libration amplitude of the ice shell, as it is expected to be the most significant (Baland et al., 2010; Van Hoolst et al., 2013). Additionally, the shell's libration is more easily observable, using instruments such as cameras, radar or laser altimeters, while the libration of interior could be inferred from measurements of the time-variable component of the C_{22} gravitational coefficient (Van Hoolst

et al., 2013).

The libration amplitude computed following the approach of Van Hoolst et al. (2013) is independent of the bulk moduli of the layers, and therefore the Poisson's ratio, since the method assumes incompressible layers. Additionally, this method assumes elastic layers and models the tidal response using frequency-independent Love numbers (Van Hoolst et al., 2013). Therefore, the libration amplitude is independent of the viscosity of the layers as well.

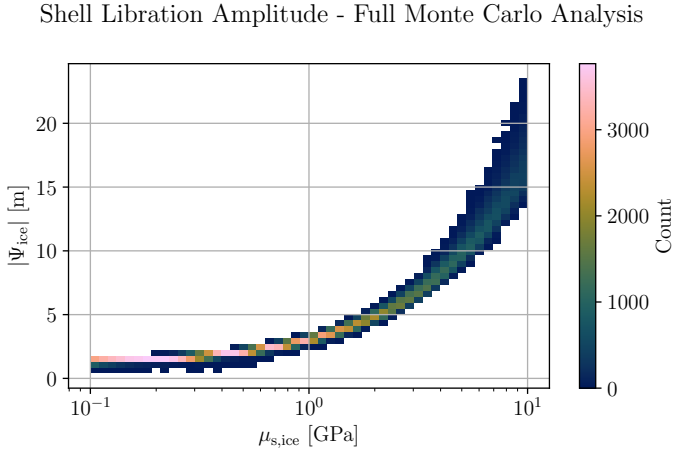

Figure 3.16: Two-dimensional histogram of the libration amplitude of the ice shell as a function of the ice shell shear modulus.

Figure 3.16 shows the two-dimensional histogram of the libration amplitude of the ice shell as a function of the ice shell shear modulus. This interior parameter is the major contributor to the libration response, as seen in the OAT sensitivity analysis, and no other parameter shows significant correlation with this observable. For low rigidities, the ice behaves like a fluid and is more easily deformed, decreasing the libration amplitude, while highly rigid shells increase the libration (Van Hoolst et al., 2013). The reduction in libration amplitude with increasing deformation can be explained considering how energy is stored in the body. Gravitational interactions cause Ganymede to both deform and wobble, resulting in energy being stored in two ways: as elastic energy due to the deformation of the shell, and as gravitational energy due to the change in orientation during libration (Van Hoolst et al., 2020). When the shell is flexible rather than rigid, it can deform in response to gravitational forces, storing more elastic energy and reducing the amount available for libration motion (Van Hoolst et al., 2020).

Measuring Ganymede's libration could provide a strong constraint on the ice shell rigidity. Constraining this parameter could, in turn, help to narrow the uncertainty in the ice shell thickness through measurements of both k_2 and h_2, as previously discussed. Pairing libration measurements with those of the tidal Love numbers could therefore provide constraints on two largely unconstrained parameters of Ganymede's interior.

However, Ganymede's libration amplitude is expected to be small (Van Hoolst et al., 2013), as shown in Figure 3.16. Additionally, the GALA instrument on board of Juice is expected to measure the shell libration amplitude with an uncertainty between 6.6 m and 17.5 m at the equator (Steinbrügge et al., 2019). Since the uncertainty is on the same order of magnitude as the libration amplitude itself, a high error in the measurements would hinder the ability to constrain the ice shell's rigidity. This highlights the importance of high-precision libration measurements to obtain meaningful constraints on both the rigidity and thickness of the ice shell.

4

Bayesian Inversion

Now that we understand the sensitivity of the observations to the model parameters, we perform a Bayesian inversion to retrieve the interior parameters of Ganymede. The general methodology and the theoretical background on Bayesian inversion are described in section 2.2 and section B.3, respectively. Here, we focus on the specific setup of the inversions, the parameters to be retrieved, and the results obtained.

We carry out four inversions, each using a different set of observations. These will be referred to as "Inversion 1" through "Inversion 4". The inversions progressively incorporate additional observational constraints. The first two use currently available spacecraft data – the MoI factor and the magnetic induction amplitude – while the last two include synthetic observations to improve the characterization of the moon's interior structure. Such measurements will be provided by the ESA's Juice mission. In addition to considering different observables, each inversion also involves different retrieved parameters and prior ranges. The rationale behind these choices is discussed in the respective section presenting each inversion. A summary of the characteristics and results of each inversion is provided in Table 4.1.

The chapter is structured as follows: section 4.1 describes the general setup of the Bayesian inversion, including the definition of the prior distributions and the likelihood function, as well as specific details on the sampling of the parameters; section 4.2 presents the results of the inversion using gravity and magnetic induction data, highlighting the current knowledge about Ganymede's interior structure; section 4.3 analyzes the potential impact of future measurements of Ganymede's tidal response on the inversion results, and how these measurements could improve our understanding of Ganymede's interior.

4.1. Bayesian Inversion Setup

We perform the Bayesian inversion using the `emcee` package for Python (Foreman-Mackey et al., 2013), which implements the affine-invariant MCMC ensemble sampler by Goodman et al. (2010), described in section 2.2. In addition to the standard "stretch move", the `emcee` sampler also implements different types of moves. Two of these are the Differential Evolution (DE) move (Nelson et al., 2013) and the DE snooker move (ter Braak et al., 2008), which are particularly useful in combination for high-dimensional problems. In the inversions described in section 4.2, we employ 32 walkers and a combination of the DE and snooker moves, with relative fractions of 0.8 and 0.2, respectively (Foreman-Mackey, 2022). This ensures an efficient exploration of the high-dimensional parameter space, while maintaining a good acceptance rate of the proposed samples.

In the inversions described in section 4.3, we instead use the standard Metropolis-Hastings (M-H) move. Due to the very small predicted uncertainty of future k_2 measurements, the acceptance rate of the sampler is significantly lower when using the DE and snooker moves. Foreman-Mackey et al. (2013) note that an acceptance fraction between 0.2 to 0.5 typically indicates proper sampler performance, while results from inversions with acceptance fractions outside this range might not reliably represent effective posterior distributions. Using the M-H move with a low-variance proposal distribution allows

Table 4.1: Summary of the different inversions performed. For each inversion, the table reports the corresponding section where it is described, the observables considered, the prior ranges of each variable, and the ranges of the constraint variables. The posterior estimates are listed as the median value (50th percentile) with uncertainties corresponding to the 16th and 84th percentiles. Empty cells indicate that the corresponding parameter is not retrieved in that inversion. Lightly shaded cells highlight parameters for which different ranges are considered across the various inversions.

		Inversion 1	Inversion 2	Inversion 3	Inversion 4
Corresponding section		Subsection 4.2.1	Subsection 4.2.2	Subsection 4.3.1	Subsection 4.3.2
Observations		MoI	MoI + induction	MoI + induction + Re(k_2)	MoI + induction + Re(k_2) + Im(k_2)
Priors	r_c [km]	$[200, 2100]$	$[200, 2100]$	$[200, 1500]$	$[200, 1500]$
	r_{ma} [km]	$[1000, 2100]$	$[1000, 2100]$	$[1400, 2000]$	$[1400, 2000]$
	D_{ice} [km]	$[1, 160]$	$[1, 160]$	$[1, 160]$	$[1, 160]$
	ρ_{ma} [kg m^{-3}]	$[2000, 8000]$	$[3000, 4000]$	$[3000, 4000]$	$[3000, 4000]$
	ρ_{hp} [kg m^{-3}]	$[1100, 1600]$	$[1100, 1400]$	$[1100, 1400]$	$[1100, 1400]$
	ρ_{ice} [kg m^{-3}]	$[900, 1300]$	$[900, 1300]$	$[900, 1300]$	$[900, 1300]$
	wt [%]	$[0, 10]$	$[0, 10]$	$[0, 10]$	$[0, 10]$
	$\log(\mu_{s,hp})$ [log(Pa)]			$[9, 10]$	$[9, 10]$
	$\log(\mu_{s,ice})$ [log(Pa)]			$[8, 10]$	$[8, 10]$
	$\log(\eta_{hp})$ [log(Pa s)]				$[12, 20]$
	$\log(\eta_{ice})$ [log(Pa s)]			$[12, 20]$	$[12, 20]$
	υ [-]			$[0.3, 0.49]$	$[0.3, 0.49]$
Constraints	ρ_c [kg m^{-3}]	$[2000, 8000]$	$[5150, 8000]$	$[5150, 8000]$	$[5150, 8000]$
Posterior estimates	r_c [km]	$1255.59^{+256.89}_{-291.51}$	$770.73^{+156.52}_{-169.20}$	$753.69^{+159.84}_{-176.38}$	$746.75^{+154.15}_{-176.86}$
	r_{ma} [km]	$1676.17^{+165.83}_{-190.92}$	$1756.67^{+77.34}_{-82.40}$	$1775.60^{+73.60}_{-85.75}$	$1787.72^{+72.12}_{-87.69}$
	ρ_c [kg m^{-3}]	$4747.03^{+1391.51}_{-730.42}$	$6060.49^{+1101.42}_{-664.07}$	$6058.99^{+1127.86}_{-677.78}$	$6082.71^{+1115.26}_{-703.40}$
	ρ_{ma} [kg m^{-3}]	$3091.09^{+836.68}_{-729.82}$	$3350.94^{+307.21}_{-237.94}$	$3323.68^{+311.14}_{-227.99}$	$3308.34^{+304.93}_{-216.52}$
	D_{ice} [km]	$70.48^{+46.43}_{-45.29}$	$110.47^{+17.21}_{-20.23}$	$106.88^{+21.46}_{-30.34}$	$102.81^{+23.08}_{-34.58}$
	r_{hp} [km]	$2339.10^{+68.50}_{-66.54}$	$2398.92^{+51.32}_{-32.63}$	$2387.47^{+56.63}_{-39.85}$	$2382.79^{+54.57}_{-45.57}$
	r_o [km]	$2560.72^{+45.29}_{-46.43}$	$2520.73^{+20.23}_{-17.21}$	$2524.32^{+30.34}_{-21.46}$	$2528.39^{+34.58}_{-23.08}$
	ρ_{hp} [kg m^{-3}]	$1432.78^{+115.05}_{-158.35}$	$1315.34^{+59.65}_{-89.91}$	$1311.73^{+65.45}_{-99.90}$	$1294.00^{+78.24}_{-103.53}$
	ρ_o [kg m^{-3}]	$1159.77^{+33.05}_{-32.68}$	$1149.90^{+31.00}_{-27.43}$	$1133.79^{+30.81}_{-17.29}$	$1132.85^{+33.62}_{-16.81}$
	ρ_{ice} [kg m^{-3}]	$1025.21^{+84.56}_{-82.37}$	$1031.11^{+74.01}_{-79.12}$	$1004.44^{+69.53}_{-66.80}$	$1008.23^{+69.42}_{-66.83}$
	wt [%]	$5.43^{+3.07}_{-3.42}$	$5.02^{+3.25}_{-3.17}$	$3.17^{+3.47}_{-2.30}$	$2.98^{+3.79}_{-2.31}$
	κ_o [S m^{-1}]	$1.75^{+0.72}_{-0.92}$	$1.65^{+0.77}_{-0.87}$	$1.18^{+0.86}_{-0.74}$	$1.12^{+0.95}_{-0.77}$
	$\log(\mu_{s,hp})$ [log(Pa)]			$9.63^{+0.26}_{-0.35}$	$9.63^{+0.26}_{-0.35}$
	$\log(\mu_{s,ice})$ [log(Pa)]			$8.91^{+0.58}_{-0.60}$	$8.78^{+0.56}_{-0.53}$
	$\log(\eta_{hp})$ [log(Pa s)]				$15.92^{+2.61}_{-1.12}$
	$\log(\eta_{ice})$ [log(Pa s)]			$15.94^{+2.76}_{-2.59}$	$16.48^{+2.19}_{-1.98}$
	υ [-]			$0.42^{+0.05}_{-0.07}$	$0.42^{+0.05}_{-0.07}$
Posterior distributions		Figure 4.3, Figure 4.4	Figure 4.5, Figure E.3	Figure 4.8, Figure E.4	Figure 4.9, Figure E.5, Figure E.6

the proposed samples to remain closer to the current state, increasing the likelihood of acceptance and achieving an acceptance fraction of around 0.2. Although this approach is less efficient and requires longer chains to ensure convergence, thorough exploration of the parameter space is still achieved thanks to the large number of samples and an increased number of walkers, set to 64. This setup provides more robust performance in the presence of likelihood functions dominated by observables with very low uncertainties.

The walkers start from a different point in the parameter space randomly selected from the prior distribution. The length of each chain is chosen to ensure convergence and depends on the inversion case. According to the `emcee` documentation (Foreman-Mackey, 2022), a chain has converged when its length is at least 50 times the autocorrelation time, $N > 50\tau$. Additionally, to avoid dependence on the initial conditions, a "burn-in" period of a few autocorrelation times is applied. Following the `emcee` documentation (Foreman-Mackey, 2022), we discard the first 2τ samples of each chain when analyzing the results.

We adopt uninformative priors for the interior parameters, meaning that their prior distribution is uniform within selected ranges, and zero outside. In general, we require:

$$\begin{cases} \rho_{\mathrm{c}} \in [5100\,\mathrm{kg\,m^{-3}}, 8000\,\mathrm{kg\,m^{-3}}] \\ \rho_{\mathrm{ice}} < \rho_{\mathrm{o}} < \rho_{\mathrm{hp}} \\ \rho_{\mathrm{ma}} < \rho_{\mathrm{c}} \\ r_{\mathrm{c}} < r_{\mathrm{ma}} < r_{\mathrm{hp}} \end{cases} \tag{4.1}$$

However, some analyses allow for a wider range of the core density, as explained in section 4.2. The specific prior ranges used in each inversion are detailed in the corresponding sections. The log-prior distribution of a model $\bar{M}_j$ is thus defined as:

$$\log\{p(\mathbf{X}|\bar{M}_j, I)\} = \begin{cases} 0 & \text{if the interior model complies with Equation 4.1} \\ -\inf & \text{otherwise} \end{cases} \tag{4.2}$$

Assuming independent, additive Gaussian uncertainties for the observations, the log-likelihood function is defined as follows:

$$\log\{p(\mathbf{\Theta}|\mathbf{X}, \bar{M}_j, I)\} = -\frac{1}{2}\sum_{i=1}^{n_{\mathrm{obs}}}\left(\frac{\Theta_i - \Theta_i^{\bar{M}_j}}{\sigma_i}\right)^2 \tag{4.3}$$

Lastly, the log-probability of the model is computed as the sum of the log-prior and the log-likelihood:

$$\log\{p(\mathbf{X}|\mathbf{\Theta}, \bar{M}_j, I)\} = \log\{p(\mathbf{\Theta}|\mathbf{X}, \bar{M}_j, I)\} + \log\{p(\mathbf{X}|\bar{M}_j, I)\} \tag{4.4}$$

Due to the large number of parameters and the diverse ranges of the physical values, we sample the free parameters in a unit hypercube. Before computing the constrained parameters and the observables, the samples are transformed from the unit hypercube to the physical values. For each variable X, given the lower and upper bounds X_{min} and X_{max}, the transformation from the unit variable u is performed as follows:

$$X = u\,(X_{\mathrm{max}} - X_{\mathrm{min}}) + X_{\mathrm{min}} \tag{4.5}$$

4.1.1. Observables and Uncertainties

The observables and their uncertainties are listed in Table 4.2, along with the inversions in which they are considered. Unlike in the sensitivity analysis presented in chapter 3, the MoI factor is included here as an observation. The uncertainties in MoI and magnetic induction amplitude correspond to the current uncertainties in the measurements from Galileo and they are taken from Schubert et al. (2004) and Kivelson et al. (2002), respectively. The uncertainties in the tidal Love numbers and in the ice shell libration are the expected uncertainties of the future Juice mission (Cappuccio et al., 2020; Van Hoolst et al., 2024).

We currently lack measurements for the tidal Love numbers k_2 and h_2, as well as for the libration amplitude of Ganymede's ice shell. Therefore, we compute the response of a specific interior model of

Table 4.2: Observables and their uncertainties used in the Bayesian inversion. If "Synthetic" is specified in the "Reference" column, the observable is synthetic and computed from the interior model parameters listed in Table 4.3. The last column indicates in which inversion(s) the corresponding observable is used.

Observable	Central Value	Uncertainty	Unit	Reference	Inversion number
I/MR^2	0.3115	0.0028	-	Schubert et al. (2004)	1, 2, 3, 4
$\|A^e\|$	0.84	0.018	-	Kivelson et al. (2002)	2, 3, 4
$\mathrm{Re}\{k_2\}$	0.5215	1×10^{-4}	-	Synthetic	3, 4
$\mathrm{Im}\{k_2\}$	-0.0002	6.8×10^{-5}	-	Synthetic	4
$\mathrm{Re}\{h_2\}$	1.4847	2.6×10^{-2}	-	Synthetic	
$\|\Psi_{\mathrm{ice}}\|$	3.0774	$6.6 - 17.4$	m	Synthetic	

Table 4.3: Interior model parameters used to compute the nominal values of the observables.

Parameter	Value	Unit	Parameter	Value	Unit
r_{c}	693.1291	km	$\log(\mu_{\mathrm{s,ma}})$	11.8751	log(Pa)
r_{ma}	1697.3503	km	$\log(\mu_{\mathrm{s,hp}})$	9.6990	log(Pa)
D_{ice}	114.6500	km	$\log(\mu_{\mathrm{s,ice}})$	9	log(Pa)
ρ_{ma}	3630.4849	$\mathrm{kg\,m^{-3}}$	$\log(\eta_{\mathrm{ma}})$	20	log(Pa s)
ρ_{hp}	1353.7375	$\mathrm{kg\,m^{-3}}$	$\log(\eta_{\mathrm{hp}})$	16	log(Pa s)
ρ_{ice}	1026.7033	$\mathrm{kg\,m^{-3}}$	$\log(\eta_{\mathrm{ice}})$	16	log(Pa s)
wt	4.3695	%	υ	0.3950	-

Ganymede and use the resulting values as the nominal values of the observables. The interior model used to generate these synthetic observations is selected as follows. The radii and densities of each layer are taken from the inversion constrained by gravity and magnetic induction data to ensure consistency with current observations. The mechanical properties of the layers are set to the central values of the parameter ranges considered in the inversion, following the approach adopted by Ermakov et al. (2021). The selected interior model parameters are listed in Table 4.3.

In our work, we assume Ganymede to be in hydrostatic equilibrium, and we use the MoI estimate from Schubert et al. (2004) obtained with the Darwin-Radau approximation. Gomez Casajus et al. (2022) more recently presented a refined gravity field model of Ganymede using Doppler tracking data from both the Galileo and Juno spacecraft flybys. The authors derived a gravity field solution up to degree and order 5 and revealed localized anomalies not previously resolved. The study confirms that Ganymede's degree-2 gravity field is consistent with hydrostatic equilibrium, but also identifies significant non-hydrostatic contributions. Taking into account these anomalies, the inferred MoI and its related uncertainty are slightly higher than earlier estimates ($I/MR^2 = 0.3159 \pm 0.0052$), implying a less differentiated interior structure (Gomez Casajus et al., 2022).

Gao et al. (2013) evaluated the reliability of the Darwin-Radau approximation for icy satellites under the assumption of hydrostatic equilibrium, which implies that their shape and gravity field are governed by rotation and self-gravity only. The authors showed that non-hydrostaticity – manifested as deviations from equipotential surfaces – can introduce significant errors in MoI estimates, particularly for slowly rotating and/or small bodies like Titan and Callisto (Gao et al., 2013). However, Ganymede's relatively rapid rotation and larger size reduce its sensitivity to such effects, indicating that the hydrostatic assumption is a reasonable approximation and supporting our use of the MoI derived by Schubert et al. (2004) with the Darwin-Radau approximation.

4.2. Current Knowledge on Ganymede's Interior Structure

This section analyzes how the current measurements of Ganymede's gravity and magnetic induction can be used to retrieve information about its interior structure. Two inversions are performed, one using only static gravity data (Inversion 1) and the other using both static gravity and magnetic induction data (Inversion 2). The results are presented in subsection 4.2.1 and subsection 4.2.2, respectively.

In the sensitivity analysis presented in chapter 3, Ganymede's mass and moment of inertia were treated as constraints to generate interior models consistent with gravity data. As illustrated in Figure 3.3, the MoI factor is correlated with the size and densities of the core and mantle, while the mass, not included in the figure, shows no significant correlation with any parameter. Additionally, the uncertainty in the moment of inertia is significantly larger than that of the mass, as indicated in Table 1.1. Since the moment of inertia provides insights into the deep interior of Ganymede and its differentiation, and considering its higher uncertainty, it will be included as an observable in the Bayesian inversion. This change removes one constraint from the model and introduces an additional free parameter. Therefore, the mantle density will be treated as a free parameter, while the core density will be computed from the mass and the other parameters. Preliminary analysis reveal that incorporating the moment of inertia into the likelihood function, rather than treating it as a constraint, changes the posterior distributions of the parameters, especially those of the core and mantle radii.

A second difference with respect to the sensitivity analysis concerns the ranges of the free parameters. In fact, some histograms from the MC analysis (e. g., Figure 3.4) indicate that certain variables, especially those related to the deep interior, are pushed toward the boundaries of their ranges. Therefore, multiple inversion setups are considered to explore a broader parameter space. Additionally, depending on the observables included in the inversion, different sets of parameters are sampled as free variables. The setup of each inversion is detailed in the corresponding subsection.

4.2.1. Bayesian Inversion with Static Gravity Data (Inversion 1)

A first inversion is performed using only Ganymede's moment of inertia factor as an observable to analyze the effect of static gravity data alone on the interior model. The sampled parameters and the ranges considered in this setup are listed in Table 4.4a, while the applied constraints are reported in Table 4.4b. The constrained parameters are computed with the procedure described in subsection 2.1.1, except for the core and mantle densities. If a model does not satisfy these constraints, it is discarded. Since the tidal and libration observations are not included in this inversion, the mechanical properties of the layers do not influence the response of the model and therefore are not sampled as free parameters.

Table 4.4: Free and constrained parameters considered in "Inversion 1".

(a) Sampling ranges of the free parameters.

Parameter	Range	Unit
r_c	$[200, 2100]$	km
r_ma	$[1000, 2100]$	km
D_ice	$[1, 160]$	km
ρ_ma	$[2000, 8000]$	$\mathrm{kg\,m^{-3}}$
ρ_hp	$[1100, 1600]$	$\mathrm{kg\,m^{-3}}$
ρ_ice	$[900, 1300]$	$\mathrm{kg\,m^{-3}}$
wt	$[0, 10]$	%

(b) Constrained parameters and corresponding constraints.

Constrained parameter	Constraint
Core density ρ_c	$[2000, 8000]\ \mathrm{kg\,m^{-3}}$
Deep interior densities	$\rho_\mathrm{ma} < \rho_\mathrm{c}$
Deep interior radii	$r_\mathrm{c} < r_\mathrm{ma} < r_\mathrm{hp}$
Hydrosphere densities	$\rho_\mathrm{ice} < \rho_\mathrm{o} < \rho_\mathrm{hp}$

A differentiated interior structure with an iron core and a silicate mantle is supported by the presence of Ganymede's intrinsic magnetic field, which suggests the existence of a dynamo action in a partially liquid core (Schubert et al., 1996). However, Anderson et al. (1996) showed that two-layer models consisting of a rocky core and an ice mantle can also be consistent with the measured MoI factor. We perform a preliminary analysis of a simple two-layer model with an external radius of $R_\mathrm{G} = 2631.2\,\mathrm{km}$ and we vary the ice shell density between $900\,\mathrm{kg\,m^{-3}}$ and $1400\,\mathrm{kg\,m^{-3}}$. We compute the core radius and density from the ice shell density and the nominal values of mass and MoI listed in Table 1.1. The resulting core radius and density are shown in Figure 4.1 with a black dotted line, confirming the possibility of an undifferentiated core, either smaller and composed of Fe-FeS or larger and composed of silicate rock.

The first inversion is thus performed with broad parameter ranges for the innermost layers to remain agnostic about their compositions and to allow for undifferentiated models. The prior range of the HP ice density is also broadened to allow for a more comprehensive exploration of the parameter space. This choice was motivated by preliminary inversion results, which showed that the posterior distribution was

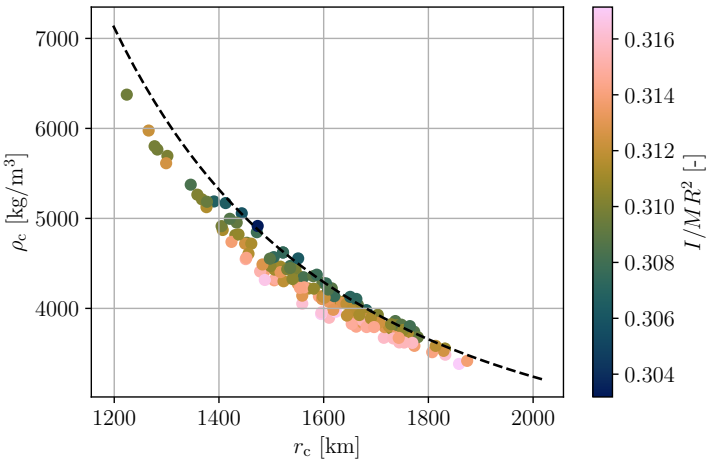

Figure 4.1: Size and density of the innermost layer of Ganymede, here referred to as "core", as obtained from "Inversion 1". Only undifferentiated models are shown, in which the core and mantle densities differ by less than 10 kg m^{-3}. The black dotted line represents the core size and density of a simple two-layer model, obtained by varying the outer layer density between 900 kg m^{-3} and 1400 kg m^{-3}, while constraining the core using the nominal mass and MoI values.

pushed toward the upper bound of 1400 kg m^{-3}. To assess whether this behavior was constrained by the prior limit, we extended the upper bound beyond physically plausible values. Although some of the resulting densities may not be realistic, this approach helps assess the sensitivity of the inversion to the prior assumptions.

The length of each chain is set to 100 000 samples, which is sufficient to ensure convergence of the chains. Figure 4.2 shows the estimated autocorrelation time τ as a function of the number of samples N for two different methods. The first one, originally used in `emcee`, is based on Goodman et al. (2010) and involves averaging the samples across all walkers to form a single, combined chain (Foreman-Mackey, 2022). The autocorrelation function is then computed for this mean chain. The second method, currently used in `emcee`, computes the autocorrelation time separately for each walker's chain and then averages these individual estimates (Foreman-Mackey, 2022). This method helps to reduce the variance of the final estimate. From Figure 4.2, we can confirm that the chains have converged.

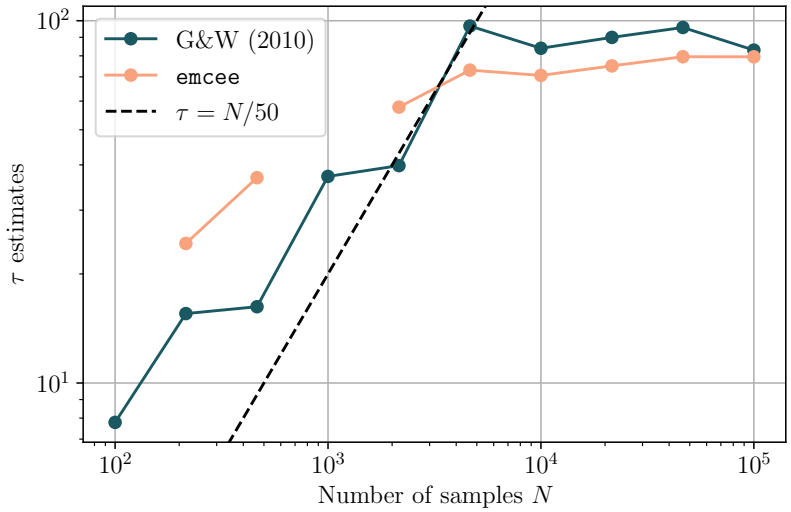

Figure 4.2: Autocorrelation time τ as a function of the number of samples N for the method suggested by Goodman et al. (2010) and the current method used in `emcee` (Foreman-Mackey, 2022). A black dashed line indicates the threshold for convergence, $\tau = N/50$.

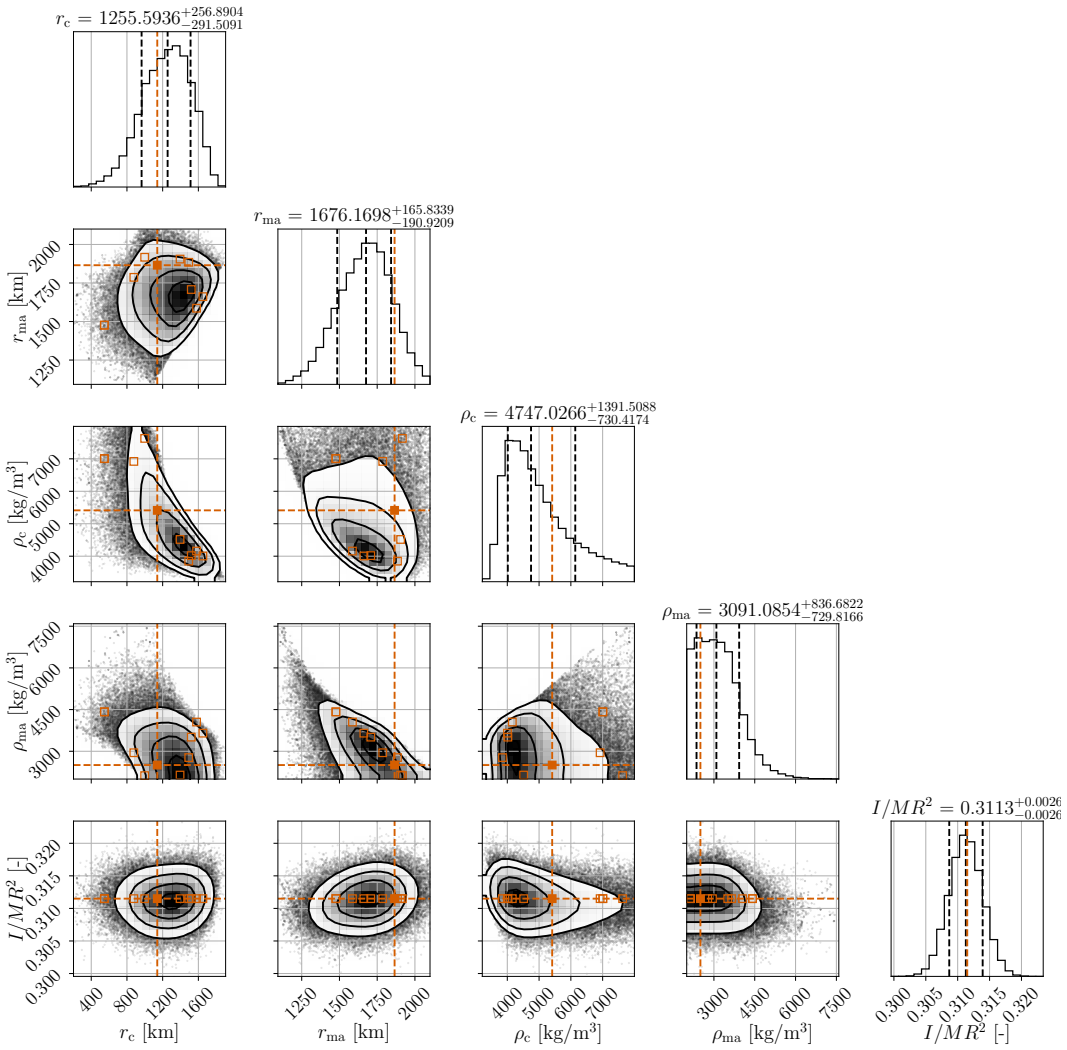

Figure 4.3: Posterior probability distributions of the core and mantle radii, r_c and r_{ma}, and their densities, ρ_c and ρ_{ma}, retrieved from "Inversion 1". The vertical dashed black lines and the annotations above the subplots indicate the 16th, 50th, and 84th percentiles. The full orange square and the orange dashed line indicate the parameters corresponding to the best-fitting sample, while the orange empty squares indicate the next nine best-fitting samples.

The posterior distributions of the core and mantle parameters retrieved from the inversion are shown in Figure 4.3 and the hydrosphere parameters are illustrated in Figure 4.4 using the Python package `corner.py` (Foreman-Mackey, 2016). These plots show the marginalized distributions of the parameters on the diagonal and the correlations between parameters on the off-diagonal with 2D contour plots. The value of the moment of inertia mainly constrains the innermost layers of Ganymede, as expected from the sensitivity analysis in chapter 3, and favors larger core and mantle radii, but lower densities for both layers (Figure 4.3).

Since the ranges of the core and mantle densities overlap, the results suggest the possibility of undifferentiated interior structures that are still consistent with the MoI value. We define a model to have an undifferentiated interior if the density difference between the core and the mantle is less than 10 kg m^{-3}. Models that satisfy this condition are shown in Figure 4.1. The trend agrees with that of the two-layer model (black dotted line), with differences arising from considering a single ice layer and using only the nominal MoI value to constrain the interior. Core sizes range from less than 1200 km to nearly 1900 km, with corresponding densities spanning from over 7000 kg m^{-3} down to below 4000 kg m^{-3}.

Regarding the hydrosphere parameters, the only one showing a trend in the posterior distribution is the HP ice density, which tends toward the upper end of the prior range. Additionally, the thickness of

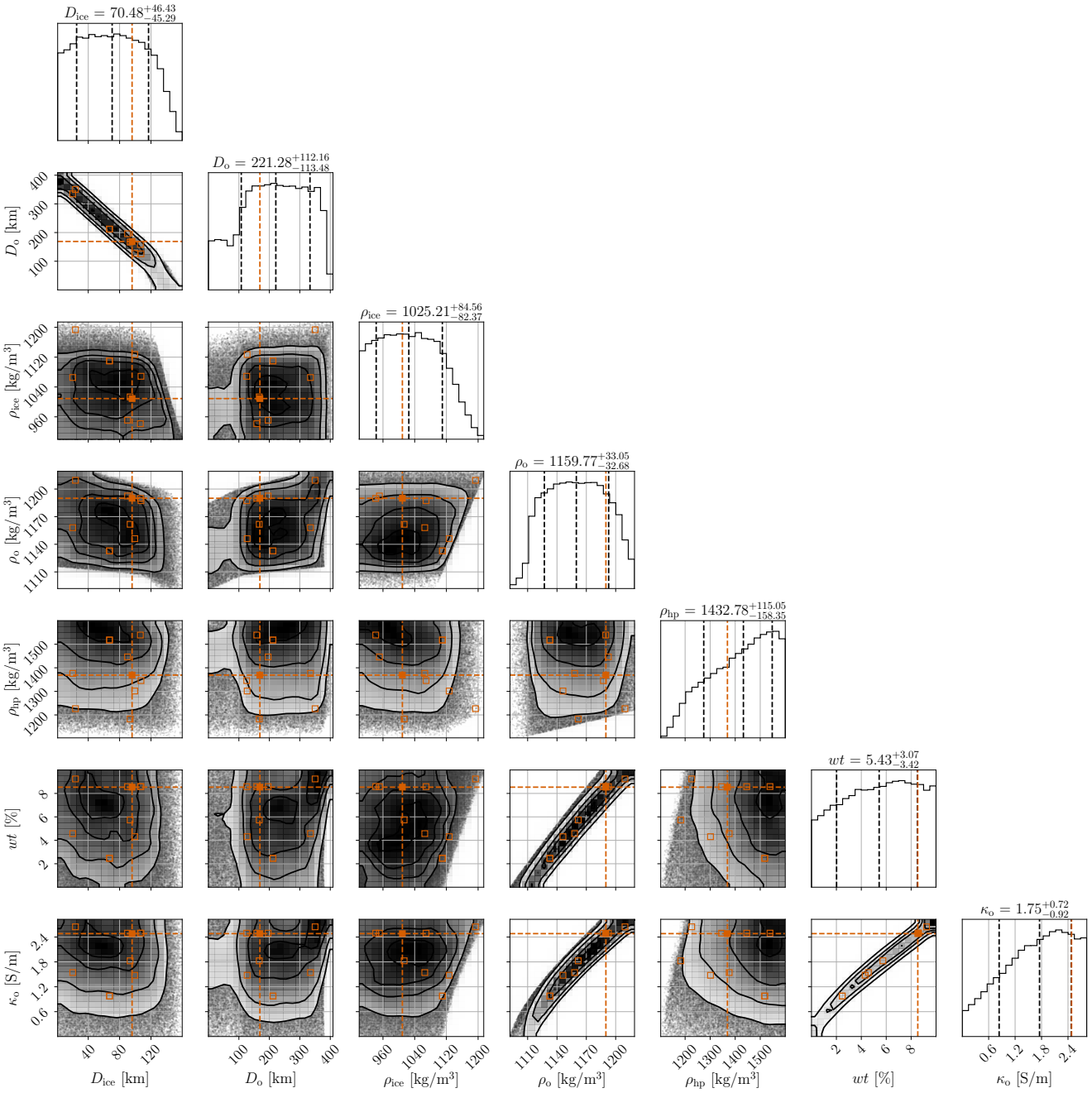

Figure 4.4: Posterior probability distributions of the hydrosphere parameters retrieved from "Inversion 1". The details are the same as described in Figure 4.3.

the ocean shows a drop in probability for thicknesses below 100 km. As discussed in subsection D.1.2, this region corresponds to the formation of ice III instead of ice V. For the remaining parameters, the distributions are relatively flat, confirming that the MoI alone can inform the deep interior structure, but does not constrain the outer layers' parameters of Ganymede. Including additional observations will help to better constrain some of these parameters.

This inversion is performed with fixed nominal values of the mass and radius of Ganymede, corresponding to their central values listed in Table 1.1. To assess the potential influence of these quantities on the posterior distributions of the parameters, two additional inversions are performed. In the first, the mass is allowed to vary within $M_{\mathrm{G}} \pm \sigma_M$ but it is not included in the likelihood function. In the second inversion, both the mass and total radius vary, and the mass is included in the likelihood function. Detailed plots are shown in Appendix E, and the parameter estimates of these inversions are reported in Table E.1 under "Additional Inversions". In both cases, the posterior distributions show no significant differences compared to the first inversion. Therefore, the mass and radius of Ganymede are kept fixed to their nominal values in all the following inversions.

4.2.2. Bayesian Inversion with Static Gravity and Magnetic Induction Data (Inversion 2)

Bayesian inversion with gravity data enables the estimation of core and mantle radii and densities. However, the hydrosphere parameters remain largely unconstrained. The sensitivity analysis revealed that different observables are sensitive to different interior parameters and highlighted the presence of parameter degeneracies. Specifically, the MoI factor is most sensitive to the core and mantle densities, magnetic induction to the ocean's thickness and conductivity, tidal displacement to the thickness and rigidity of the ice shell, and libration amplitude to shell's rigidity. Relying on a single observable is insufficient to break these degeneracies and constrain the full interior structure.

In this section, we therefore analyze the joint inversion of gravity and magnetic induction data. This approach has already proven successful in the case of Europa (Petricca et al., 2023), where magnetic induction data improved constraints on both the thickness of the ice shell and the ocean depth. We expect to achieve similar results for Ganymede, as the sensitivity analysis showed that the magnetic induction amplitude is strongly influenced by both the ice shell and ocean thickness.

In the previous inversion, we did not assume a specific composition for the core and mantle, leaving the densities of these layers largely unconstrained. However, given that intrinsic magnetic field observations support a differentiated interior structure, in this and the following inversions we assume a fully differentiated body. The core and mantle densities are therefore restricted to ranges consistent with plausible compositions – specifically, a metallic (Fe or Fe–FeS) core and a silicate mantle. Similarly, the HP ice density is limited to physically realistic values.

In this inversion, we use both the moment of inertia and the magnetic induction amplitude as observational constraints, and we adopt the parameter ranges reported in Table 4.5. The length of each chain is set to 100 000 samples, ensuring convergence according to the same approach described in subsection 4.2.1. Figure 4.5 shows the posterior probability distributions of the hydrosphere parameters.

Table 4.5: Free and constrained parameters considered in "Inversion 2".

(a) Sampling ranges of the free parameters.

Parameter	Range	Unit
r_{c}	$[200, 2100]$	km
r_{ma}	$[1000, 2100]$	km
D_{ice}	$[1, 160]$	km
ρ_{ma}	$[3000, 4000]$	$\mathrm{kg\,m^{-3}}$
ρ_{hp}	$[1100, 1400]$	$\mathrm{kg\,m^{-3}}$
ρ_{ice}	$[900, 1300]$	$\mathrm{kg\,m^{-3}}$
wt	$[0, 10]$	%

(b) Constrained parameters and corresponding constraints.

Constrained parameter	Constraint
Core density ρ_{c}	[5150, 8000] $\mathrm{kg\,m^{-3}}$
Deep interior radii	$r_{\mathrm{c}} < r_{\mathrm{ma}} < r_{\mathrm{hp}}$
Hydrosphere densities	$\rho_{\mathrm{ice}} < \rho_{\mathrm{o}} < \rho_{\mathrm{hp}}$

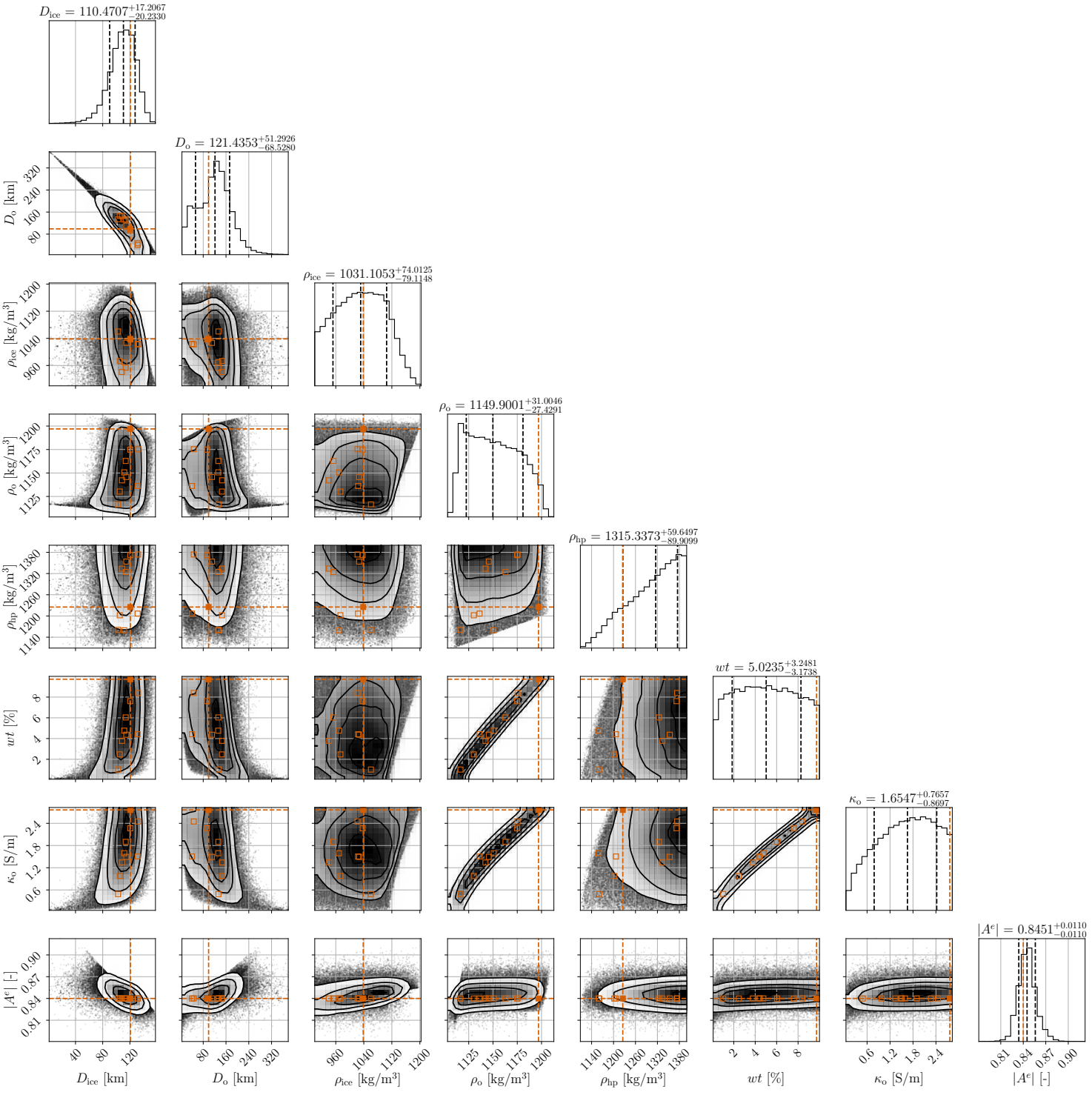

Figure 4.5: Posterior probability distributions of the hydrosphere parameters retrieved from "Inversion 2". The details are the same as described in Figure 4.3.

The inclusion of magnetic induction data has a clear impact on the posterior distributions of the ice shell thickness and the ocean thickness, computed as the difference between the outer radius of the ocean and that of the HP ice layer. While these parameters were previously largely unconstrained, their posteriors now show well-defined peaks around 110 km and 120 km, respectively. Our estimate of the ice shell thickness differs from the value of 150 km proposed by Kivelson et al. (2002) to match the observed magnetic induction amplitude. In their study, Kivelson et al. (2002) assumed that the strength of the magnetic induction amplitude decreases with the cube of the distance from the conducting surface and therefore used the simplified relation $r_o \sim \left(1 - (0.84)^{1/3}\right) R_G$ to estimate the depth of the conductive layer. This estimate should be considered as an order-of-magnitude indication of the ocean depth. The difference from our results likely arises from the more comprehensive model that we use to calculate the magnetic induction amplitude of a spherical conducting layer buried beneath the surface (Equation 2.9).

The distributions of the ice shell and ocean densities also exhibit changes. Even though they remain somewhat broad and less peaked compared to the layers' sizes, the 1-σ credible interval for the ice shell has narrowed, indicating a tighter constraint. Additionally, the posterior distribution of the ocean density has shifted toward lower values, suggesting that models with a less dense ocean are favored by the observables. The ocean composition, quantified by wt, is not constrained by the inversion. This outcome was expected based on the sensitivity analysis, which showed that all compositions within the range considered can produce a magnetic induction amplitude consistent with the observations (see Figure 3.11).

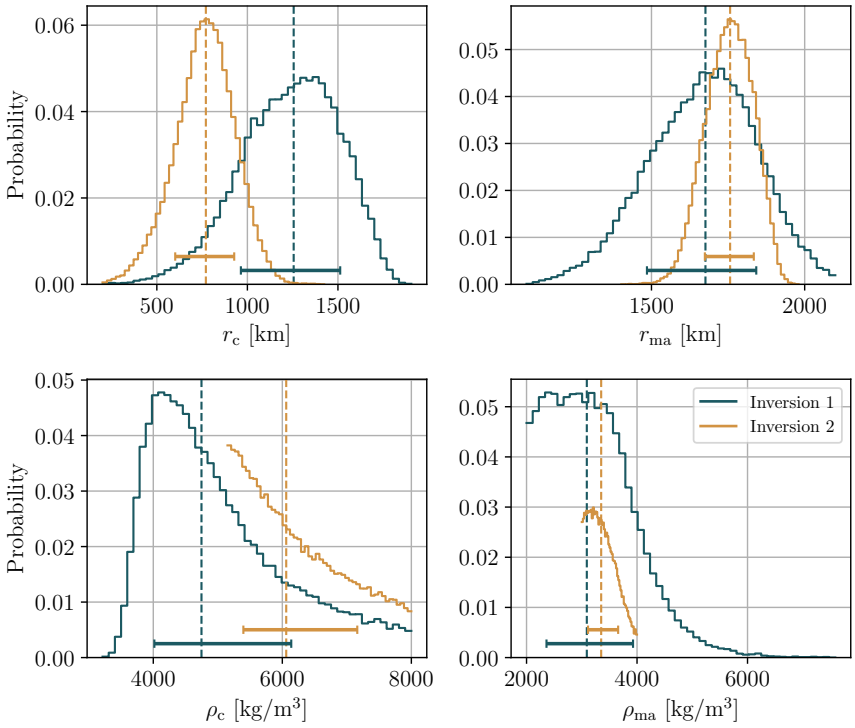

Figure 4.6: Posterior probability distributions of the core and mantle radii and densities retrieved from "Inversion 1" and "Inversion 2". The vertical dashed lines indicate the 50th percentile of the posterior distributions, while the horizontal bars show the 1-σ credible region.

Figure 4.6 and Figure 4.7 compare the marginalized posterior distributions of the Ganymede's interior structure parameters for "Inversion 1", using only the moment of inertia, and "Inversion 2", using both the moment of inertia and magnetic induction data. Figure 4.6 shows that the inversion results are strongly influenced by the choice of the prior ranges of the densities. When physical constraints are applied, the inversion favors smaller core radii and larger mantle radii. Additionally, both core and mantle densities are shifted toward the lower end of their prior range, suggesting a Fe-FeS composition for the core and an olivine silicate mantle (Sohl et al., 2002). The 1-σ credible intervals, indicated

by the horizontal bars, are narrower in this inversion, showing improved parameter constraints when assumptions on the layers' composition are included. Another inversion was performed using the same parameter settings as in "Inversion 1", but including the magnetic induction amplitude. The results are reported in Table E.1 in the column labeled "MoI + induction, Undifferentiated" and show that this observable has almost no effect on the parameters of the two innermost layers. Therefore, the moment of inertia is the most informative observation for constraining the structure of Ganymede's deep interior.

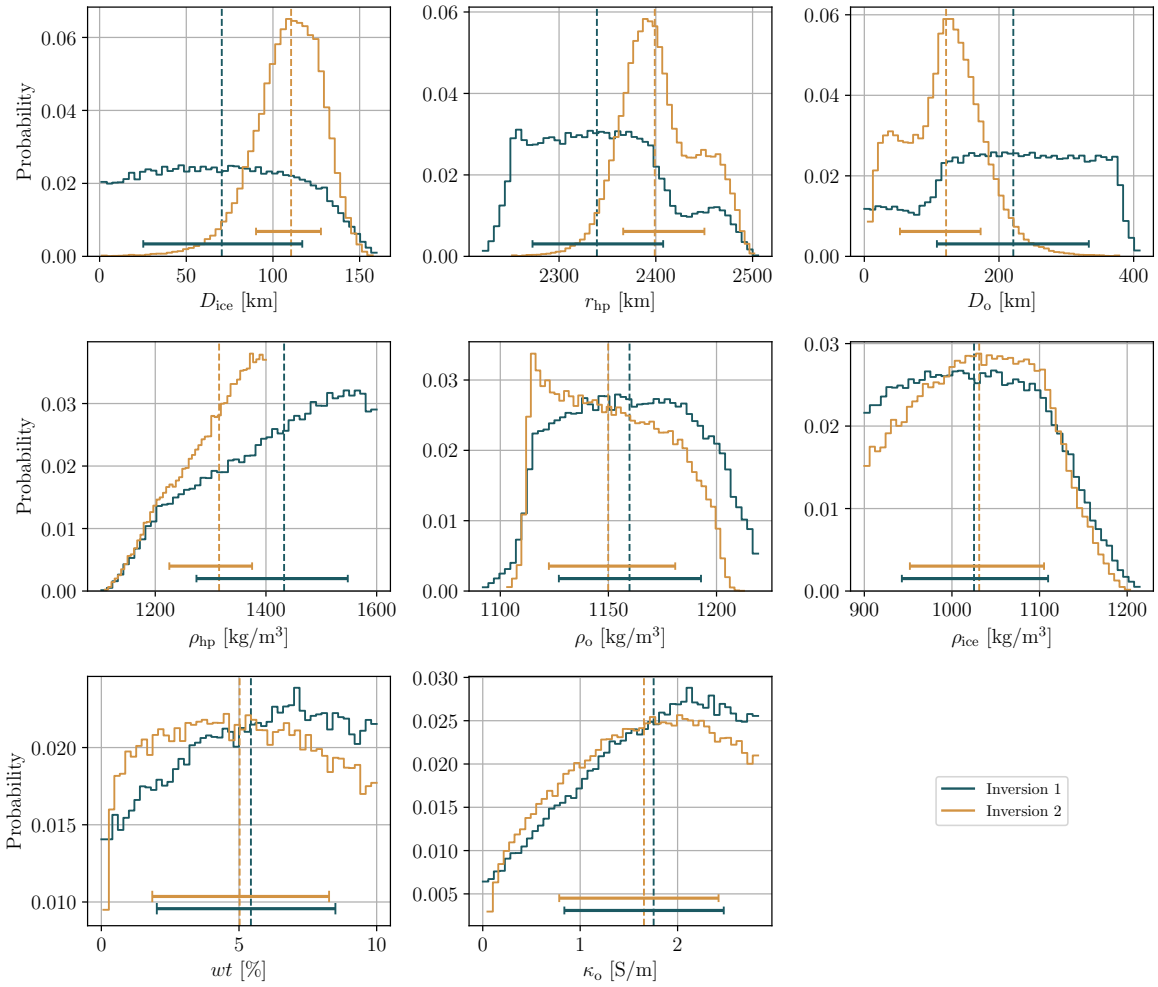

Figure 4.7: Posterior probability distributions of the hydrosphere parameters retrieved from "Inversion 1" and "Inversion 2". The vertical dashed lines indicate the 50th percentile of the posterior distributions, while the horizontal bars show the 1-σ credible region.

Figure 4.7 shows the posterior distributions of the hydrosphere parameters. In contrast with the deep interior parameters, introducing the magnetic induction amplitude as an observable significantly improves the constraints on several hydrosphere parameters, particularly the ice shell and ocean thicknesses, as discussed above. Similarly to the core and mantle densities, introducing a tighter constraint on the density of the HP ice narrows the posterior distribution and shifts it toward the upper end of the prior range, with a peak at $1400\,\mathrm{kg\,m^{-3}}$.

As mentioned in subsection 1.2.2, Jia et al. (2024) more recently estimated a magnetic induction amplitude of 0.72 ± 0.03 using an improved model of Ganymede's magnetic field. This value is lower than the one reported by Kivelson et al. (2002), but has a higher uncertainty. The inversion results would likely change if the updated estimate were used. A reduced induction amplitude would imply a deeper ocean, a lower ocean conductivity, or a combination of the two (Jia et al., 2024), while the larger uncertainty would broaden the posterior distributions and weaken the constraints on interior parameters. Future work should incorporate the updated estimate of the magnetic induction amplitude from Jia

et al. (2024) into the Bayesian inversion framework.

Table 4.1 summarizes the 50th percentile and the 1-σ credible intervals of Ganymede's interior structure parameters retrieved from the various inversions. In particular, the results of "Inversion 2" represent the current best estimate of Ganymede's interior structure, as it incorporates all available observational and theoretical constraints. In fact, this inversion combines both the MoI factor and magnetic induction data, and imposes physical constraints on the layers' densities based on plausible compositions. These compositions are consistent with a differentiated interior, a hypothesis supported by the observation of Ganymede's intrinsic magnetic field (Schubert et al., 1996).

In the next section, we analyze how future observations from the Juice mission could improve our understanding of Ganymede's interior structure. To this end, we consider the expected uncertainties of Juice's measurements and generate synthetic data based on the current best estimate of Ganymede's interior. The interior model used to generate the synthetic data is selected from the results of "Inversion 2". Among the 10 best-fitting models, we choose the one whose parameters are closest to the median values of the posterior distributions. The nominal parameters of this model are listed in Table 4.3, and the corresponding synthetic observations are reported in Table 4.2.

4.3. Future Measurements

In this section, we analyze how future measurements of Ganymede's tidal response and libration could help constrain its interior structure. Petricca et al. (2023) suggested that, while magnetic induction measurements are crucial for constraining the ocean's thickness, they are insufficient to infer its composition. Instead, tidal observations may provide this information, as the real part of the Love numbers depends on the ocean's density (Jara-Orué et al., 2016). Additionally, Hussmann et al. (2016) showed that the phase lag of the Love numbers (i. e., their imaginary part) is sensitive to the viscosity and rigidity of the ice shell, while the phase lag difference is mainly influenced by the properties of the HP ice layer. Lastly, although measurements of the shell's libration amplitude alone cannot fully constrain Ganymede's interior structure, they could still provide valuable information on the ice shell density and rigidity (Van Hoolst et al., 2013), and help to resolve the degeneracy between these parameters, as explained in section 3.3. Progressively incorporating these observations in the inversion process will refine our understanding of Ganymede's interior structure.

First, we perform a Bayesian inversion using the real part of k_2 ("Inversion 3"), since this observable might provide information on the ice shell and subsurface ocean (Van Hoolst et al., 2024). The Juice mission is expected to deliver high-accuracy measurements of the real part of k_2. It is thus of significant scientific interest to understand how this measurement can constrain interior parameters, such as the ocean density and the rigidities of the ice layers, and improve the current understanding of the Ganymede's interior structure. Then, we perform a second inversion using both the real and imaginary parts of k_2 ("Inversion 4") to retrieve information on the ice layers' viscosities, related to the dissipation in the moon.

Libration measurements carry large uncertainties and are therefore not expected to provide a useful constraint on the ice shell rigidity, as discussed in section 3.3. Since the induction signal already provides a strong constraint on the ice shell thickness, combining the tidal Love number k_2 with the displacement Love number h_2 could, in principle, allow the rigidity to be constrained through their relation with the ice shell thickness (Wahr et al., 2006, Equation 11). Exploring this possibility is left for future work, while here we perform two inversions using the real and imaginary parts of k_2, excluding h_2 and the shell libration amplitude.

4.3.1. Bayesian Inversion with Static Gravity, Magnetic Induction, and Real k_2 Tidal Love Number (Inversion 3)

The inversion described in this section is performed using Ganymede's moment of inertia, magnetic induction amplitude, and the real part of the k_2 tidal Love number as observables. To compute Ganymede's tidal response, the mechanical properties of the layers are required. From the results of the sensitivity analysis presented in section 3.3, among the mechanical properties of the layers, only

the ice shell and HP ice rigidities, the ice shell viscosity, and the Poisson's ratio are considered as free parameters, since they significantly influence the real part of the Love number. The other mechanical properties are considered fixed and set to the values listed in Table 4.3. This reduces the dimensionality of the parameter space, therefore decreasing the number of samples required for the chains to reach convergence.

The ranges and the constraints considered in this inversion are summarized in Table 4.6. The ranges of the core and mantle radii have been reduced compared to the previous inversions to exclude values that lie outside the bounds of the obtained posterior distribution. This adjustment reduces the number of discarded models and improves convergence by avoiding sampling in regions where no solutions were found with the previous inversion, which is particularly important given the large parameter space.

Table 4.6: Free and constrained parameters considered in "Inversion 3".

(a) Sampling ranges of the free parameters. The symbol log indicates the logarithm in base 10.

Parameter	Range	Unit
r_c	$[200, 1500]$	km
r_ma	$[1400, 2000]$	km
D_ice	$[1, 160]$	km
ρ_ma	$[3000, 4000]$	$\mathrm{kg\,m^{-3}}$
ρ_hp	$[1100, 1400]$	$\mathrm{kg\,m^{-3}}$
ρ_ice	$[900, 1300]$	$\mathrm{kg\,m^{-3}}$
wt	$[0, 10]$	%
$\log(\mu_\mathrm{s,hp})$	$[9, 10]$	log(Pa)
$\log(\mu_\mathrm{s,ice})$	$[8, 10]$	log(Pa)
$\log(\eta_\mathrm{ice})$	$[12, 20]$	log(Pa s)
υ	$[0.3, 0.49]$	-

(b) Constrained parameters and corresponding constraints.

Constrained parameter	Constraint
Core density ρ_c	$[5150, 8000]\ \mathrm{kg\,m^{-3}}$
Deep interior radii	$r_\mathrm{c} < r_\mathrm{ma} < r_\mathrm{hp}$
Hydrosphere densities	$\rho_\mathrm{ice} < \rho_\mathrm{o} < \rho_\mathrm{hp}$

For this inversion, the `emcee.moves.GaussianMove` sampler is used, which implements a standard M-H algorithm where new proposals are drawn from a multivariate Gaussian distribution centered on the current state (Foreman-Mackey, 2022). Since the sampling is performed in an 11-dimensional unit hypercube, we provide the covariance of the proposal distribution as a vector with 11 elements, each set to 1×10^{-5}. This defines an axis-aligned Gaussian proposal distribution, without correlations between parameters. Each element specifies the variance (i. e., the square of the standard deviation) along the corresponding dimension. In this case, setting all elements to 1×10^{-5} means that the sampler proposes small steps in each parameter direction, which allows for a fine exploration of the parameter space and avoids overly large jumps that would result in low acceptance rates. 64 walkers are used, each with a chain length of 7×10^6. This ensures that the inversion has converged and that the acceptance rate is around 0.2.

Figure 4.8 shows the posterior probability distributions of the hydrosphere and the mechanical properties of the layers. The distributions of the core and mantle parameters are not shown, as they closely resemble those previously obtained. The distribution of the ice shell thickness also remains qualitatively similar to the one obtained in the previous inversion, but the median shifts slightly toward lower values, and the credible interval broadens toward the lower end of the prior range. Including the real part of k_2 as an observable thus favors models with thinner ice shells and, consequently, thicker oceans. A thicker ocean increases the magnetic induction signal of the body, which can be compensated for by a less conductive ocean (i. e., a lower ocean salinity). This effect is reflected in the posterior distribution of the ocean composition, which shifts toward and peaks at the lower end of the prior range, indicating a preference for a less saline ocean. It is also interesting to note the correlation between ice shell thickness and ocean composition: models with thinner ice shells allow for a wider range of possible ocean compositions, while increasing ice shell thickness constrains the composition to higher values. This is because a thicker ice shell leaves a thinner ocean layer, which must be more conductive to produce the observed magnetic induction signal.

A similar trend to that of the ocean composition is observed for the ocean density (Figure E.4). This

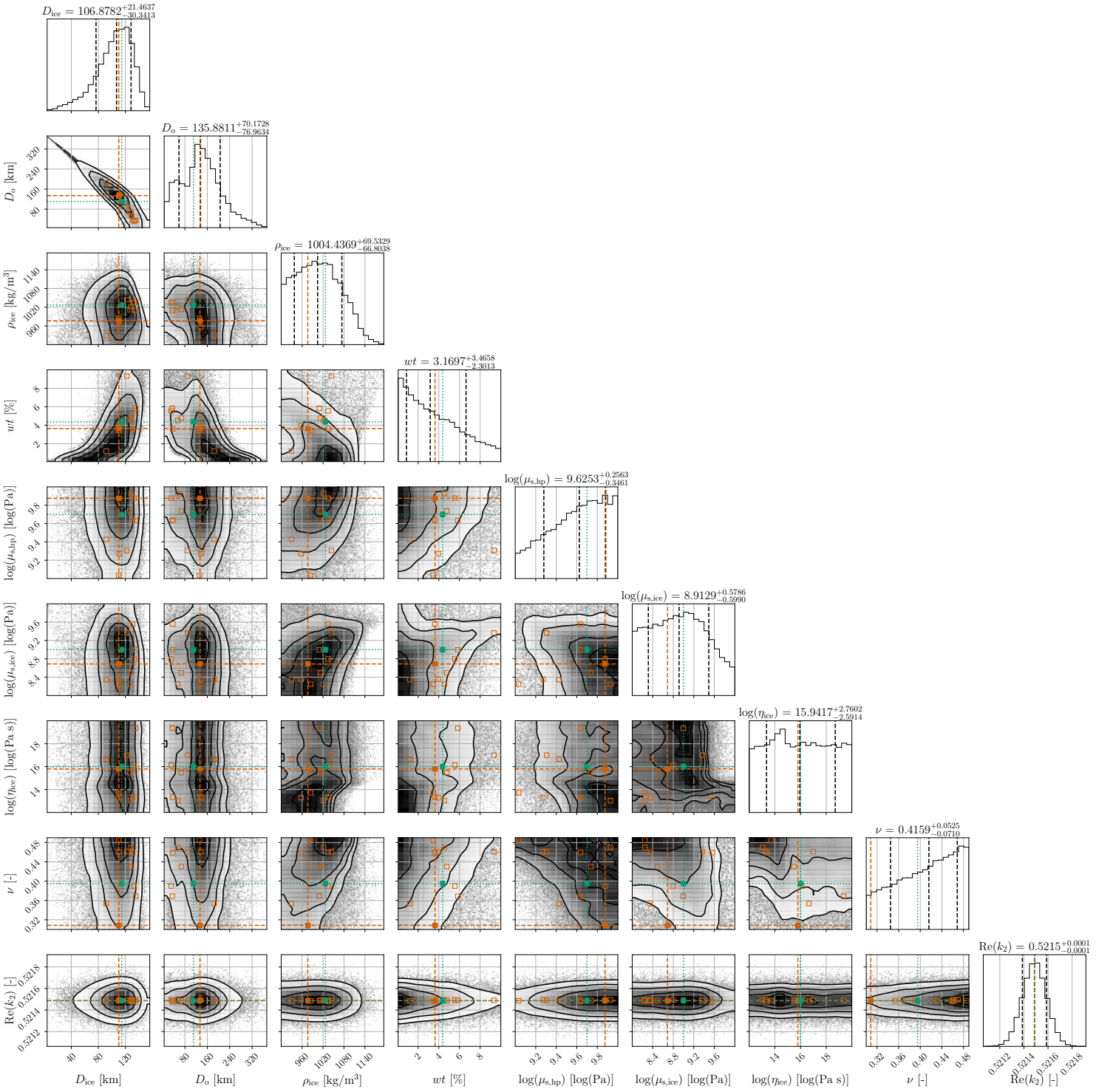

Figure 4.8: Posterior probability distributions of the hydrosphere parameters and mechanical properties retrieved from "Inversion 3". The vertical dashed black lines and the annotations above the subplots indicate the 16th, 50th, and 84th percentiles. The full orange squares and the orange dashed lines indicate the parameters corresponding to the best-fitting sample, while the orange empty squares indicate the next nine best-fitting samples. The full green squares and dotted lines indicate the true values of the parameters used to generate the synthetic data.

behavior can be explained in two ways. First, since the density is derived from the composition, a lower salinity directly translates into a lower density. Second, models with thinner ice shells yield higher $\mathrm{Re}(k_2)$ values, which can be balanced by a lower ocean density, as this has the opposite effect on the Love number. The real part of k_2 can thus provide information on the ocean composition, as suggested by Petricca et al. (2023), while the magnetic induction amplitude remains more sensitive to the ocean thickness. However, it is important to note that as discussed in section 3.2 and shown in Figure 3.6, the computation of ocean density becomes less accurate for thin ice shells. This could accentuate the spike observed in the posterior distribution of the ocean density at low values. A more accurate computation of ocean density may therefore modify the posterior distribution and should be considered in future work, but we expect the overall behavior to remain qualitatively similar. Lastly, the median value of the ice shell density is also shifted toward lower values, with a slightly narrower credible interval, showing an improvement in the constraint of this parameter when introducing tidal observations.

Regarding the mechanical properties of the layers, models with a rigid HP ice layer and incompressible layers are favored, as indicated by the distributions of $\mu_{\mathrm{s,hp}}$ and υ, which peak at the upper ends of their prior ranges. The distribution of the ice shell viscosity is overall flat, except for a local increase in probability density just above 1×10^{14} Pa s. According to Figure 3.12, this viscosity range corresponds to the transition between fluid-like and elastic behavior of the ice shell. Interestingly, this parameter also correlates with the ocean composition: models with low ocean salinity tend to favor a low-viscosity ice shell to increase $\mathrm{Re}(k_2)$, whereas at higher salinities, this preference disappears and the whole range of viscosities becomes equally likely. Lastly, the models show a preference for ice shell rigidity values in the middle of the prior range, around 1 GPa, with relatively high probability density also at the lower end, but with a strong decrease at higher rigidities.

4.3.2. Bayesian Inversion with Static Gravity, Magnetic Induction, Real and Imaginary k_2 Tidal Love Number (Inversion 4)

The inversion described in this section is performed using Ganymede's moment of inertia, magnetic induction amplitude, and both the real and the imaginary parts of the k_2 Love number as observables. Compared to "Inversion 3" (subsection 4.3.1), the viscosity of the HP ice layer is also included as a free parameter, since Figure 3.14 shows the dependence of the imaginary part of the Love number on this parameter. The ranges and constrained considered in this inversion are listed in Table 4.7.

Table 4.7: Free and constrained parameters considered in "Inversion 4".

(a) Sampling ranges of the free parameters. The symbol log indicates the logarithm in base 10.

Parameter	Range	Unit
r_{c}	$[200, 1500]$	km
r_{ma}	$[1400, 2000]$	km
D_{ice}	$[1, 160]$	km
ρ_{ma}	$[3000, 4000]$	$\mathrm{kg\,m^{-3}}$
ρ_{hp}	$[1100, 1400]$	$\mathrm{kg\,m^{-3}}$
ρ_{ice}	$[900, 1300]$	$\mathrm{kg\,m^{-3}}$
wt	$[0, 10]$	%
$\log(\mu_{\mathrm{s,hp}})$	$[9, 10]$	log(Pa)
$\log(\mu_{\mathrm{s,ice}})$	$[8, 10]$	log(Pa)
$\log(\eta_{\mathrm{hp}})$	$[12, 20]$	log(Pa s)
$\log(\eta_{\mathrm{ice}})$	$[12, 20]$	log(Pa s)
υ	$[0.3, 0.49]$	-

(b) Constrained parameters and corresponding constraints.

Constrained parameter	Constraint
Core density ρ_{c}	[5150, 8000] $\mathrm{kg\,m^{-3}}$
Deep interior radii	$r_{\mathrm{c}} < r_{\mathrm{ma}} < r_{\mathrm{hp}}$
Hydrosphere densities	$\rho_{\mathrm{ice}} < \rho_{\mathrm{o}} < \rho_{\mathrm{hp}}$

Similarly to the previous inversion, the `emcee.moves.GaussianMove` sampler is used, with a covariance of 1×10^{-5} for each parameter. 64 walkers are used, each with a chain length of 1×10^{7} to ensure convergence and an acceptance rate of around 0.2.

Figure 4.9 shows the posterior probability distributions of the hydrosphere parameters and the mechanical

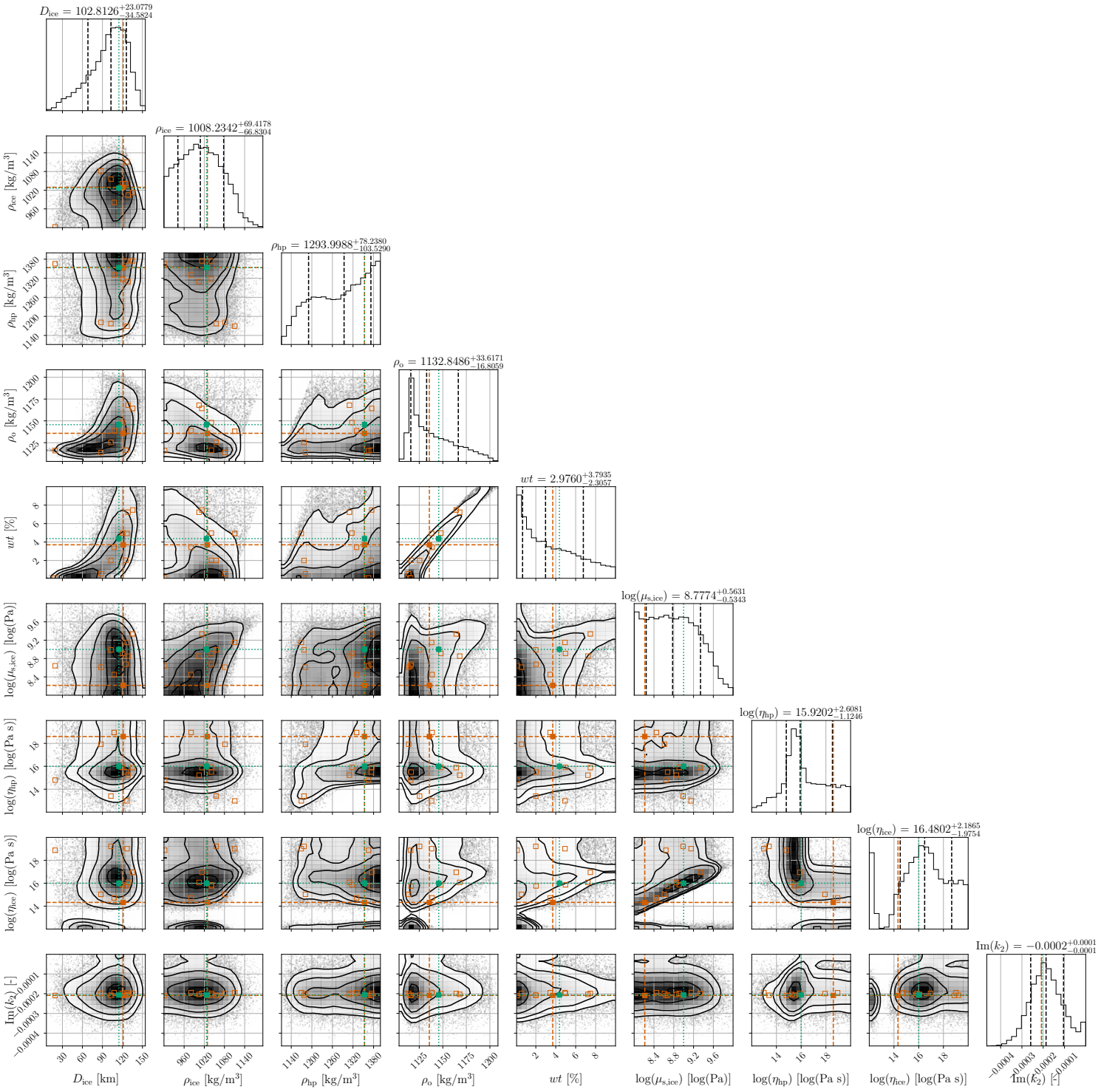

Figure 4.9: Posterior probability distributions of the hydrosphere parameters and mechanical properties retrieved from "Inversion 4". The vertical dashed black lines and the annotations above the subplots indicate the 16th, 50th, and 84th percentiles. The full orange squares and the orange dashed lines indicate the parameters corresponding to the best-fitting sample, while the orange empty squares indicate the next nine best-fitting samples. The full green squares and dotted lines indicate the true values of the parameters used to generate the synthetic data.

properties of the layers. Overall, the hydrosphere parameters show distributions similar to those obtained in the previous inversion. A notable difference arises in the HP ice density, which now presents a region of higher probability density at lower values, while the previous inversion yielded a linearly increasing distribution. The ocean composition and density distributions present higher peaks at the same values as before, while the conductivity distribution now shifts toward the lower end of the prior range, indicating a preference for a less saline ocean.

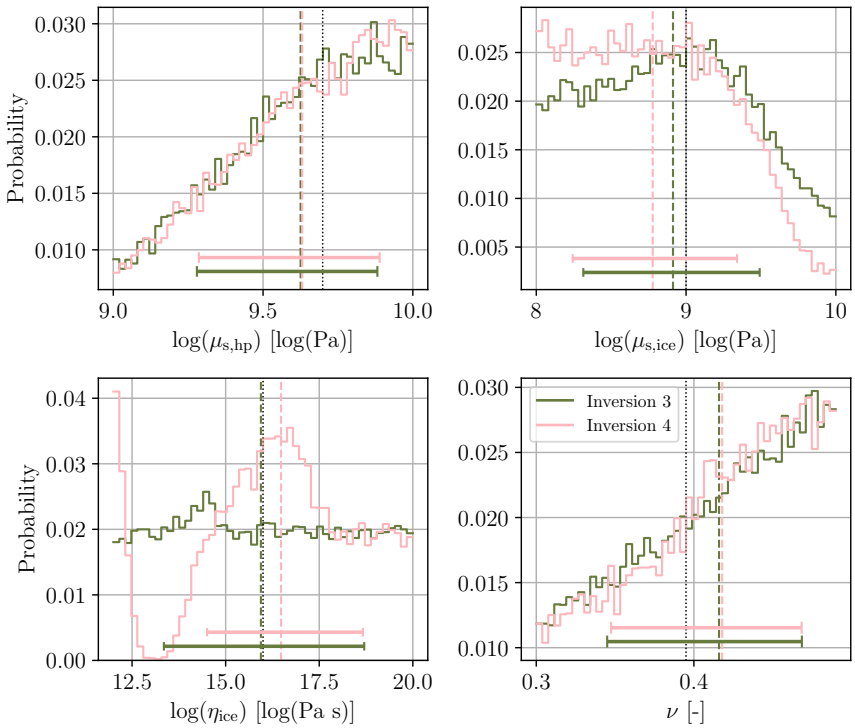

Figure 4.10: Posterior probability distributions of the mechanical properties retrieved from "Inversion 3" and "Inversion 4". The black vertical dotted lines indicate the true values of the parameters used to generate the synthetic data. The vertical dashed lines indicate the 50th percentile of the posterior distributions, while the horizontal bars show the 1-σ credible region. The HP viscosity is not shown, as it is not included in "Inversion 3".

Including $\mathrm{Im}(k_2)$ does not significantly affect the posterior distributions of the HP ice shear modulus and Poisson's ratio, but it does impact the viscosities of both ice layers and the shear modulus of the ice shell, as shown in Figure 4.10, which compares the posterior probability distributions of the mechanical properties retrieved from "Inversion 3" and "Inversion 4". $\mu_{s,ice}$ shifts its median toward lower values, with a slightly narrower credible interval, indicating a preference for a low-rigidity ice shell when the dissipation in the moon is taken into account. The viscosities of both ice layers are now well constrained: the ice shell viscosity shows a bimodal distribution with peaks at approximately 1×10^{12} and 1×10^{16} Pa s, while the HP ice viscosity presents a single peak at around 1×10^{15} Pa s. The bimodal distribution of the ice shell viscosity can be confirmed with the two-dimensional histogram from the sensitivity analysis (Figure 3.14), given that the nominal value of $\mathrm{Im}(k_2)$ is -2×10^{-4}. For this value, two regions with a higher concentration of models can be identified: one at low viscosities, around 1×10^{13}, and another at higher viscosities, around 1×10^{16}, which correspond to the peaks of the posterior distribution. This behavior can be explained by Maxwell rheology and the bell-shaped dependence of $\mathrm{Im}(k_2)$ on ice viscosity: for a given value of $\mathrm{Im}(k_2)$, two viscosity solutions exist, one on each side of the peak, except at the maximum of $\mathrm{Im}(k_2)$, which corresponds to the maximum dissipation and occurs when the Maxwell time equals the tidal period. However, Hussmann et al. (2016) reported that reasonable values for ice viscosity are above 1×10^{13} Pa s, which corresponds to the viscosity at melting point. Therefore, very low viscosities can be considered physically unrealistic, and this should be taken into account when interpreting the results.

The joint distribution of the viscosities of the two ice layers reveals a trade-off. Since both layers

contribute to the total dissipation in the moon, strong dissipation in one layer reduces the contribution of the other. For instance, the peak in the HP ice viscosity corresponds to a high dissipation within this layer. At these values, the viscosity of the ice shell spans a wide range in the upper end of the prior. In this regime, the ice shell behaves as a rigid layer, thus producing little dissipation, while the total dissipation of the moon remains consistent. The same reasoning applies in the opposite case: when the ice shell viscosity peaks, most of the dissipation is concentrated in this layer, allowing the high-pressure ice viscosity to vary over the upper end of the range without significantly affecting the total. Measurements of the phase lag difference between k_2 and h_2 might help to resolve this degeneracy by constraining the viscosity of the HP ice layer, as illustrated in section 3.3.

4.3.3. Summary of the Different Inversions

In this section, we summarize the main findings of the Bayesian inversion approach, highlight the differences between the various inversions performed, and conclude with the key takeaways of our work.

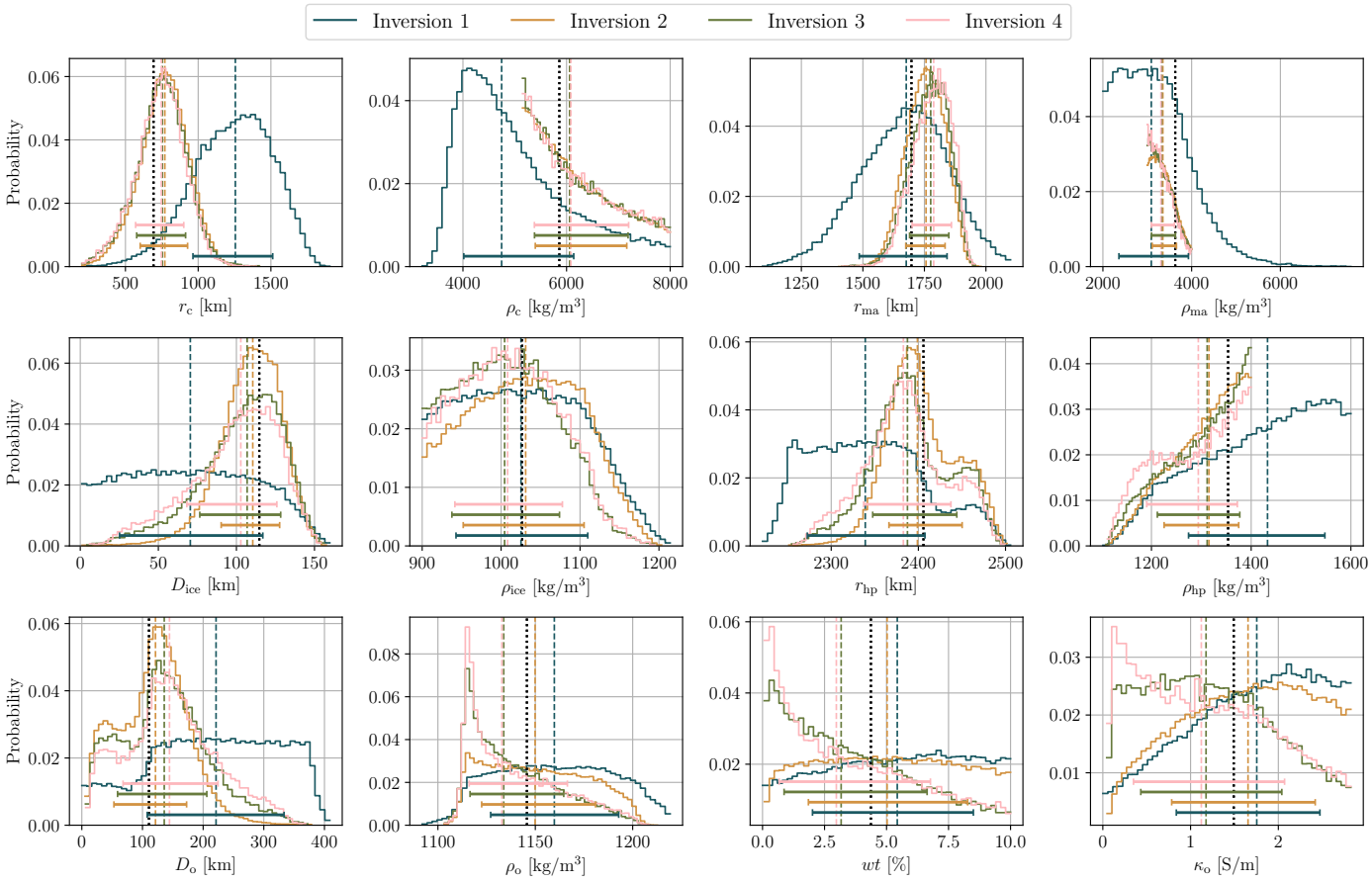

Figure 4.11: Posterior probability distributions of the interior parameters retrieved from the four different inversions, as detailed in Table 4.1. The black vertical dotted lines indicate the true values of the parameters used to generate the synthetic data. The vertical dashed lines indicate the 50th percentile of the posterior distributions, while the horizontal bars show the 1-σ credible region.

Figure 4.11 compares the posterior probability distributions of the interior parameters retrieved from four different inversions. Differences are evident in both the median values and the widths of the 1-σ credible intervals, especially for some parameters. The inversion using the MoI alone provides constraints on the deep interior layers, which can be improved by adopting narrower prior ranges. For other parameters, however, it yields broad and, in some cases, nearly flat distributions, indicating that several hydrosphere properties remain largely unconstrained when relying solely on this observable. Including magnetic induction data significantly improves the results, as discussed in subsection 4.2.2, providing estimates of the ocean depth and thickness. Yet, the distribution of the ocean composition remains flat, highlighting

the trade-off between these parameters. Adding the real part of k_2 further improves the results, while including its imaginary part mainly affects the estimates of the mechanical properties of the ice layers, as shown in Figure 4.10.

When including the Love number in the inversion, the credible intervals of the ice shell and ocean thicknesses become larger, while their medians remain overall similar. Compared to the magnetic induction amplitude, the $\mathrm{Re}(k_2)$ observation is consistent with a wider range of ice shell thicknesses. Because the real k_2 measurement has a much lower uncertainty than the induction amplitude, it is more constraining and it results in a "higher weight" in the inference. This means that the sampler tends to satisfy the $\mathrm{Re}(k_2)$ observation more often than the induction amplitude, which effectively broadens the posterior distribution of the ice shell thickness.

For the densities, the most notable effect is on the ocean density, whose distribution shifts towards lower values and becomes more sharply peaked, confirming the role of $\mathrm{Re}(k_2)$ in constraining this parameter. Since the ocean density is determined by its composition, the posterior distribution of wt also changes, shifting the median toward lower values and peaking at the lower end of the prior range, suggesting a preference for a less saline ocean. As suggested by Petricca et al. (2023), the real part of k_2 can thus be used to infer the ocean composition, while the magnetic induction amplitude is more sensitive to the ocean thickness. Since the ocean salinity is directly related to its composition, the posterior distribution of κ_o also shifts toward lower values, while its credible interval remains similar. Magnetic induction and k_2 observations therefore have opposite effects on the inferred ocean salinity: the former favors a more saline ocean, while the latter prefers a less saline one. When both observations are considered, the effect of the real part of k_2 dominates due to its lower uncertainty, resulting in a posterior distribution consistent with a low-salinity ocean. In the interpretation of the results, it is important to keep in mind the selected values for the synthetic observations, as different measurements of k_2 would likely lead to different parameter estimates.

Lastly, the median density of the ice shell layer is also shifted toward lower values, with a slightly narrower credible interval, showing an improvement in the constraint of this parameter when introducing tidal observations. The distribution of the HP ice density, on the other hand, remains overall similar when including $\mathrm{Re}(k_2)$, but it changes when also considering $\mathrm{Im}(k_2)$, as discussed in subsection 4.3.2.

For some parameters, the true values used to generate the synthetic observations were well retrieved by the final (and most complete) inversion. This is particularly the case, with some exceptions, for the innermost layers, where the MoI factor provides a relatively strong constraint, and for the ice shell thickness. In this case, the retrieved value is slightly lower than the true one, and it deviates further from the fiducial value when tidal observations are included in the inversion. The most uncertain parameters remain those related to the ocean composition and, in some cases, the mechanical properties, which are also the most physically uncertain. The inability to recover the true values for certain parameters indicates that degeneracies remain, and that additional constraints will be needed to improve parameter estimates.

Overall, Figure 4.11 illustrates the new information provided by each dataset and highlights the benefit of constraining the interior parameters using multiple observations, as each dataset brings complementary information that together provide a more comprehensive view of Ganymede's internal structure.

5

Conclusions and Recommendations

This chapter presents the conclusions of the thesis and outlines the recommendations for future work. The aim of this project was to investigate how the joint inversion of gravity, magnetic induction, tidal and libration observations can improve the characterization of Ganymede's interior structure, from which the main research question was formulated:

How can the joint inversion of gravity, magnetic induction, tidal and libration observations improve the characterization of the interior structure of Ganymede?

The research question was further divided into four sub-questions:

1. **[SQ1.1] What is the sensitivity of the different observations to variations in Ganymede's interior structure?**
2. **[SQ1.2] To what extent can the joint inversion of available data – static gravity and magnetic induction – constrain Ganymede's interior structure?**
3. **[SQ1.3] How can the addition of tidal and libration observations to the inversion improve the characterization of Ganymede's interior structure?**
4. **[SQ1.4] To what extent do the uncertainties in the input data affect the reliability of the inversion results?**

The work was divided into two main parts: a sensitivity analysis to evaluate the influence of the model parameters on the observables, which answered the first sub-question, and a Bayesian inversion to retrieve the interior parameters of Ganymede, which answered the second and third sub-questions. The fourth sub-question was not addressed in this project due to time constraints, but it could be explored in future work.

5.1. Conclusions

This work presents a comprehensive framework for characterizing Ganymede's interior structure through joint Bayesian inversion of gravity, magnetic induction, tidal, and libration observations. The results demonstrate that combining multiple observables is crucial to constrain the internal structure of icy moons, and that a joint inversion approach significantly improves parameter estimates compared to the use of a single-dataset.

The sensitivity analysis provided a preliminary understanding of how each observable changes with variations in interior parameters. The magnetic induction amplitude was found to be most sensitive to the thickness and conductivity of the subsurface ocean. Tidal displacement, particularly the real part of the Love number k_2, showed high sensitivity to the ice shell thickness and rigidity, while libration amplitude was primarily influenced by the shell's shear modulus. The analysis indicated that Ganymede's shell libration amplitude is small, in the same order of magnitude as the expected uncertainty from the Juice mission. Therefore, high measurements errors would hinder the ability to constrain the ice

shell's rigidity, highlighting the importance of high-precision libration observations to obtain meaningful constraints. The study also revealed several parameter degeneracies, such as the one between shell thickness, ocean density, and shear modulus in the tidal response. These findings highlight the need for a joint inversion approach to integrate multiple datasets and break such degeneracies.

The Bayesian inversion was performed in successive steps, progressively incorporating additional observables. The initial inversion using only Ganymede's moment of inertia provided broad constraints on the deep interior: the core radius was estimated at 1256^{+257}_{-292} km, with the mantle radius at 1676^{+166}_{-191} km. The densities estimates of these layers overlapped, leaving open the possibility of undifferentiated interiors if other constraints are not taken into account. In this inversion, the hydrosphere parameters were largely unconstrained, with almost flat posterior distributions and only a trend in the high-pressure ice density toward the prior upper bound.

The assumption of a differentiated structure, with density priors restricted to physically plausible Fe-FeS cores and silicate mantles, further narrowed the estimates of the deep interior structure parameters. In this case, the core radius shifted to smaller values, around 771^{+157}_{-169} km, and the mantle radius to larger values, 1757^{+77}_{-82} km, while both densities were shifted toward the lower ends of their prior ranges, supporting a Fe-FeS core and an olivine-rich mantle.

Including magnetic induction data significantly improved the estimates of the outer layers. In particular, the ice shell thickness was constrained around 110 km, and the ocean thickness peaked near ~ 125 km. The external radius of the high-pressure ice was also estimated to be ~ 2400 km. While this observables sharpened the distributions of layer thicknesses, they did not constrain the ocean composition, confirming the degeneracy between ocean salinity and thickness.

The inclusion of the tidal Love number k_2 improved the parameter estimates, although the results in this study strongly depend on the synthetic observations generated by the fiducial model, and different values of k_2 would likely yield different parameter estimates. In particular, the real part of the k_2 Love number helped refine the constraints on both the ice shell density and the ocean composition. The median ice shell density shifted downward to $\sim 1000\,\mathrm{kg/m^3}$, while the ocean density peaked at values around $1100\,\mathrm{kg/m^3}$, consistent with a low-salinity ocean. This value is lower than that assumed in the fiducial model used to generate the synthetic observations, highlighting that degeneracies between parameters are still present. Nevertheless, $\mathrm{Re}(k_2)$ allowed high-density oceans, and thus oceans with high $MgSO_4$ concentrations, to be ruled out. This inversion also provided constraints on mechanical properties: the rigidity of the high-pressure ice layer was pushed toward the upper end of the prior ($\mu_{\mathrm{s,hp}} \sim 10^{10}$ Pa), while incompressible layers ($\upsilon \sim 0.49$) were favored.

Finally, the inversion incorporating moment of inertia, magnetic induction amplitude, and both the real and imaginary parts of k_2, yielded the most comprehensive characterization of Ganymede's structure. The bimodal distribution of the ice shell viscosity revealed two possible dissipation regimes at $\sim 10^{12}$ and $\sim 10^{16}$ Pa s, while the viscosity of the high-pressure ice peaked at $\sim 10^{15}$ Pa s. The inclusion of tidal observations therefore not only constrains some of the mechanical properties of the ice layers, but also supports a low-density, low-salinity ocean.

Overall, the results demonstrate that a joint Bayesian inversion is a powerful tool for the characterization of planetary interiors. Starting from static gravity data alone, which constrain only the deep interior, the progressive inclusion of magnetic induction and tidal observations reduces parameter degeneracies, leading to a more comprehensive picture of Ganymede's structure. The framework developed here is not only applicable to Ganymede and the upcoming ESA's Juice mission data, but can be extended to other icy moons such as Europa and Enceladus, where spacecraft data will provide similar observational constraints.

5.2. Recommendations for Future Work

The results obtained in this thesis are promising, but several aspects could be refined or further investigated in future work. We divide the recommendations into two parts: the first concerns improvements of the interior modeling framework, while the second addresses possible extensions to aspects not considered in this study.

With respect to the interior modeling, several elements could be improved. First, the ocean density was computed from the mean pressure of the layer. However, we showed that this approach differs from calculating the density at each depth and then averaging the values, especially for thicker oceans. Future studies could adopt this more precise method to improve ocean density estimates. Second, we assumed a constant temperature profile in the convective ocean. A more realistic approach would be to consider an adiabatic temperature profile, where the temperature varies with depth depending on the thermal expansivity and the specific heat of the ocean. This would shift the intersection point of the pressure–temperature profile with the ice–liquidus curve, thus increasing the ocean thickness. Third, alternative ocean compositions could be explored. In particular, a water-NaCl solution could be considered, since the assumed composition in this study is itself a simplification.

Additionally, the modeling of Ganymede's interior structure could be improved by adopting self-consistent approaches, such as the method proposed by Kamata et al. (2016) or the framework implemented in *PlanetProfile* (Styczinski et al., 2023). These models derive radial profiles of mechanical, thermodynamic, and electrical properties by combining observed constraints with assumptions about composition and laboratory-based equations of state. Such an approach would, for example, yield depth-dependent conductivities that vary with the density and temperature of the ocean, which would influence the moon's magnetic induction response (Styczinski et al., 2022). At the same time, adopting a self-consistent framework introduces additional uncertainties, since some of the parameters rely on (semi-)empirical parameterizations. For example, the viscosity profile in the ice shell is usually described by a scaling law that depends on the assumed activation energy of ice, which itself remains uncertain. As a result, while these models offer a more realistic representation of the interior structure, they also strongly depend on the assumed rheological and thermodynamic parameters, which introduce an additional degree of uncertainty.

Lastly, to compute the tidal response we assumed a Maxwell rheological model to describe the viscoelastic behavior of Ganymede. While the Maxwell model is appropriate for capturing relaxation properties when the forcing period is close to the Maxwell time, it cannot represent attenuation across a wide range of frequencies (Tobie et al., 2025). More advanced rheological descriptions exist, including the Burgers, Andrade, Sundberg–Cooper, and Cole models. The Burgers model accounts for viscous creep and transient anelasticity, while the Andrade model provides a more accurate transient response, but both rely on empirical parameters that are largely unconstrained (Tobie et al., 2025). The Sundberg–Cooper model combines features of Andrade and Burgers to reproduce laboratory data at high frequencies, and the Cole model, developed for water ice, links dissipation to microscopic processes (Tobie et al., 2025). Future work could employ more advanced rheological models to improve the accuracy of Ganymede's viscoelastic response. Such approaches, however, introduce additional uncertainties due to the empirical parameters involved. For instance, adopting an Andrade model would require treating its two rheological parameters as free variables, therefore expanding the parameter space and increasing computational cost.

We now discuss possible extensions of this work, focusing in particular on the inclusion of additional observations in the Bayesian inversion. In this work, we considered the moment of inertia factor, the magnetic induction amplitude, and the real and imaginary parts of the k_2 tidal Love number. Future studies could incorporate the h_2 tidal Love number and the shell libration amplitude, which would provide additional constraints, particularly on the ice shell thickness and rigidity, and potentially on the viscosity of the HP ice. Additionally, the fourth sub-question could be addressed to investigate how uncertainties in the observations affect the retrieval of the interior parameters. A notable example is the libration measurement, which is expected to have large uncertainties. Given the expected magnitude of the shell libration, these uncertainties would lead to a very broad range of possible ice shell rigidities. In contrast, reducing the measurement uncertainty would significantly narrow this range, improve the estimation of this parameter, and reduce its degeneracy with the ice shell thickness.

In this work, we assume Ganymede to be in hydrostatic equilibrium. However, as discussed in subsection 4.1.1, this simplification may not fully capture the moon's interior state. Future studies could relax this assumption by accounting for deviations from hydrostaticity and considering the more recent MoI estimate of Casajus et al. (2021), which incorporates non-hydrostatic contributions. Additionally, as mentioned in subsection 1.2.2, Jia et al. (2024) reported an updated estimate of Ganymede's magnetic induction response, which was obtained by using magnetohydrodynamic simulations to subtract plasma

and ionospheric current contributions from spacecraft measurements. This refined analysis revealed an induction efficiency of $\sim 0.72 \pm 0.03$ (Jia et al., 2024), significantly lower than that reported by Kivelson et al. (2002). Future work should therefore update the value currently used in this study with the latest estimate obtained by Jia et al. (2024). Lastly, our results depend on the synthetic observations derived from the chosen fiducial model parameters. Future work could explore how variations in these measurements influence the parameter estimates.

In modeling Ganymede's magnetic induction response, we performed several simplifications, such as assuming a uniform excitation field from Jupiter, a single, uniform, and spherically symmetric conducting layer inside Ganymede, and an inducing period corresponding to Jupiter's synodic period. However, Van Hoolst et al. (2024) highlighted that electromagnetic induction responses at multiple frequencies are necessary to break the degeneracy between the ice shell thickness, ocean thickness, and ocean conductivity, since responses at a single frequency are insufficient to uniquely determine the parameters. While available Galileo and Juno data only allowed measurements of the induced magnetic field at the main inducing frequency (Jupiter's synodic period), Juice will perform measurements at secondary induction frequencies. Future studies could therefore incorporate multi-frequency induction modeling. Moreover, in addition to the magnetic induction amplitude, the phase lag of the magnetic induction response could also be included in the inversion. Seufert et al. (2011) showed that, with a more comprehensive magnetic field model, the phase lag can reveal interactions between the conducting layers.

In this study, we only considered the degree-two tidal response of a 1D, spherically symmetric Ganymede forced at its orbital period. While the degree-two tidal potential dominates because of the strong decrease of the tidal forcing with the distance from Jupiter, very accurate data from 3GM may allow the detection of higher-order terms in Ganymede's tidal response (Van Hoolst et al., 2024). For example, a measurement of the degree-three tide could introduce constraints on lateral variations in ice shell thickness, density and rheology (Van Hoolst et al., 2024). In addition, tides raised by other moons may also play a role, even though they are much weaker than those induced by Jupiter. Moon–moon tides are expected to generate vertical displacements of less than a millimeter, but resonances between the forcing frequencies of Io, Europa, and Callisto and Ganymede's ocean eigenmodes could amplify the response (Van Hoolst et al., 2024). If such resonances occur, their effect on the tidal Love numbers could allow the detectability of moon–moon tides. Measuring these tides at multiple frequencies with 3GM could then provide constraints on the viscoelastic behavior of the ice shell and on the ocean thickness to within about 10 km (Van Hoolst et al., 2024). Future work could therefore extend the analysis to include lateral variations and moon–moon tides.

References

Anderson, J., E. Lau, W. Sjogren, G. Schubert, and W. Moore (1996). "Gravitational constraints on the internal structure of Ganymede". In: *Nature* 384.6609, pp. 541–543. DOI: 10.1038/384541a0.

Baland, R.-M. and T. Van Hoolst (Oct. 2010). "Librations of the Galilean satellites: The influence of global internal liquid layers". In: *Icarus* 209.2, pp. 651–664. ISSN: 0019-1035. DOI: 10.1016/j.icarus.2010.04.004.

Baland, R.-M., M. Yseboodt, and T. Van Hoolst (2012). "Obliquity of the Galilean satellites: The influence of a global internal liquid layer". In: *Icarus* 220.2, pp. 435–448. DOI: 10.1016/j.icarus.2012.05.020.

Beuthe, M. (Sept. 2015). "Tidal Love numbers of membrane worlds: Europa, Titan, and Co." In: *Icarus* 258, pp. 239–266. ISSN: 0019-1035. DOI: http://dx.doi.org/10.1016/j.icarus.2015.06.008.

Biersteker, J. B., B. P. Weiss, C. J. Cochrane, C. D. Harris, X. Jia, K. K. Khurana, J. Liu, N. Murphy, and C. A. Raymond (2023). "Revealing the interior structure of icy moons with a Bayesian approach to magnetic induction measurements". In: *The Planetary Science Journal* 4.4, p. 62. DOI: 10.3847/PSJ/acc331.

Cappuccio, P., A. Hickey, D. Durante, M. Di Benedetto, L. Iess, F. De Marchi, C. Plainaki, A. Milillo, and A. Mura (2020). "Ganymede's gravity, tides and rotational state from JUICE's 3GM experiment simulation". In: *Planetary and Space Science* 187, p. 104902. DOI: 10.1016/j.pss.2020.104902.

Casajus, L. G., M. Zannoni, D. Modenini, P. Tortora, F. Nimmo, T. Van Hoolst, D. Buccino, and K. Oudrhiri (2021). "Updated Europa gravity field and interior structure from a reanalysis of Galileo tracking data". In: *Icarus* 358, p. 114187. DOI: 10.1016/j.icarus.2020.114187.

Chizhov, V. (1993). "Thermodynamic properties and thermal equations of the state of high-pressure ice phases". In: *Journal of applied mechanics and technical physics* 34.2, pp. 253–262. DOI: 10.1007/BF00852521.

Crameri, F. (2023). "Scientific colour maps". en. In: DOI: https://doi.org/10.5281/zenodo.8409685.

Crameri, F., G. E. Shephard, and P. J. Heron (Oct. 2020). "The misuse of colour in science communication". In: *Nature Communications* 11.1. ISSN: 2041-1723. DOI: https://doi.org/10.1038/s41467-020-19160-7.

Dobrovolskis, A. R. (Nov. 1990). "Tidal disruption of solid bodies". In: *Icarus* 88.1, pp. 24–38. ISSN: 0019-1035. DOI: https://dx.doi.org/doi:10.1016/0019-1035(90)90175-9.

Downey, B. G. and F. Nimmo (Feb. 2025). "Titan's spin state as a constraint on tidal dissipation". In: *Science Advances* 11.6. ISSN: 2375-2548. DOI: 10.1126/sciadv.adl4741.

Eckman, R. A., A. J. Brown, D. R. Adamo, and R. G. Gottlieb (2016). *Normalization and implementation of three gravitational acceleration models*. Tech. rep. URL: https://ntrs.nasa.gov/citations/20160011252.

Ermakov, A. I., R. S. Park, J. Roa, J. C. Castillo-Rogez, J. T. Keane, F. Nimmo, E. S. Kite, C. Sotin, T. J. W. Lazio, G. Steinbrügge, S. M. Howell, B. G. Bills, D. J. Hemingway, V. Viswanathan, G. Tobie, and V. Lainey (Aug. 2021). "A Recipe for the Geophysical Exploration of Enceladus". In: *The Planetary Science Journal* 2.4, p. 157. ISSN: 2632-3338. DOI: 10.3847/PSJ/ac06d2.

European Cooperation for Space Standardization (Mar. 2009). *ECSS-E-ST-40C: Software - General Requirements*. Tech. rep. Available at https://ecss.nl/standard/ecss-e-st-40c-software-general-requirements/. European Space Agency.

European Space Agency (2005). *Cosmic Vision: Space Science for Europe 2015-2025*. ESA Bulletin Reports BR-247. Noordwijk, The Netherlands: ESA Publications Division. ISBN: 92-9092-489-6. URL: https://www.esa.int/esapub/br/br247/br247.pdf.

European Space Agency (2014). *JUICE - JUpiter ICy moons Explorer: Exploring the emergence of habitable worlds around gas giants*. Tech. rep. ESA/SRE(2014)1. European Space Agency (ESA). URL: https://sci.esa.int/web/juice/-/54994-juice-definition-study-report.

European Space Agency (2021). *Voyage 2050: Long-Term Plan for the ESA Science Programme*. URL: https://www.cosmos.esa.int/documents/1866264/1866292/Voyage2050-Senior-Committee-report-public.pdf/e2b2631e-5348-5d2d-60c1-437225981b6b?t=1623427287109.

European Space Agency (May 2023). *Science Payload – JUICE Mission*. Accessed: 2025-09-19. URL: https://sci.esa.int/web/juice/-/50073-science-payload.

Foreman-Mackey, D. (June 2016). "corner.py: Scatterplot matrices in Python". In: *The Journal of Open Source Software* 1.2, p. 24. ISSN: 2475-9066. DOI: https://doi.org/10.21105/joss.00024.

Foreman-Mackey, D. (2022). *emcee: The MCMC Hammer – Documentation*. Accessed: 2025-07-04. emcee Development Team. URL: https://emcee.readthedocs.io/en/stable/.

Foreman-Mackey, D., D. W. Hogg, D. Lang, and J. Goodman (Mar. 2013). "emcee: The MCMC Hammer". In: *Publications of the Astronomical Society of the Pacific* 125.925, pp. 306–312. ISSN: 1538-3873. DOI: 10.1086/670067.

Gao, P. and D. J. Stevenson (Nov. 2013). "Nonhydrostatic effects and the determination of icy satellites' moment of inertia". In: *Icarus* 226.2, pp. 1185–1191. ISSN: 0019-1035. DOI: https://doi.org/10.1016/j.icarus.2013.07.034.

Gomez Casajus, L., A. I. Ermakov, M. Zannoni, J. T. Keane, D. Stevenson, D. R. Buccino, D. Durante, M. Parisi, R. S. Park, P. Tortora, and S. J. Bolton (Dec. 2022). "Gravity Field of Ganymede After the Juno Extended Mission". In: *Geophysical Research Letters* 49.24. ISSN: 1944-8007. DOI: 10.1029/2022GL099475.

Goodman, J. and J. Weare (Jan. 2010). "Ensemble samplers with affine invariance". In: *Communications in Applied Mathematics and Computational Science* 5.1, pp. 65–80. ISSN: 1559-3940. DOI: 10.2140/camcos.2010.5.65.

Grasset, O., M. Dougherty, A. Coustenis, E. Bunce, C. Erd, D. Titov, M. Blanc, A. Coates, P. Drossart, L. Fletcher, et al. (2013). "JUpiter ICy moons Explorer (JUICE): An ESA mission to orbit Ganymede and to characterise the Jupiter system". In: *Planetary and Space Science* 78, pp. 1–21. DOI: 10.1016/j.pss.2012.12.002.

Gregory, P. (2005). *Bayesian logical data analysis for the physical sciences: A comparative approach with Mathematica® support*. Cambridge University Press. ISBN: 9780511791277.

Gurnett, D., W. Kurth, A. Roux, S. Bolton, and C. Kennel (1996). "Evidence for a magnetosphere at Ganymede from plasma-wave observations by the Galileo spacecraft". In: *Nature* 384.6609, pp. 535–537. DOI: 10.1038/384535a0.

Hand, K. and C. Chyba (Aug. 2007). "Empirical constraints on the salinity of the europan ocean and implications for a thin ice shell". In: *Icarus* 189.2, pp. 424–438. ISSN: 0019-1035. DOI: 10.1016/j.icarus.2007.02.002.

Hand, K., C. Sotin, A. Hayes, and A. Coustenis (2020). "On the habitability and future exploration of ocean worlds". In: *Space science reviews* 216.5, p. 95. DOI: 10.1007/s11214-020-00713-7.

Hay, H. C. F. C., I. Matsuyama, and R. T. Pappalardo (May 2022). "The High-Frequency Tidal Response of Ocean Worlds: Application to Europa and Ganymede". In: *Journal of Geophysical Research: Planets* 127.5. ISSN: 2169-9100. DOI: 10.1029/2021JE007064.

Hofmann-Wellenhof, B. and H. Moritz (2006). *Physical geodesy*. Springer Science & Business Media. ISBN: 978-3-211-23584-3.

Hussmann, H., D. Shoji, G. Steinbrügge, A. Stark, and F. Sohl (2016). "Constraints on dissipation in the deep interiors of Ganymede and Europa from tidal phase-lags". In: *Celestial Mechanics and Dynamical Astronomy* 126, pp. 131–144. DOI: 10.1007/s10569-016-9721-0.

Jara Orue, H. (2016). "Rotational Dynamics of Icy Satellites". In: DOI: 10.4233/uuid:2e35b789-735a-47a3-ac4f-63dd7651de44.

Jara-Orué, H. and B. Vermeersen (Mar. 2016). "Tides on Jupiter's moon Ganymede and their relation to its internal structure". In: *Netherlands Journal of Geosciences - Geologie en Mijnbouw* 95.2, pp. 191–201. ISSN: 1573-9708. DOI: http://dx.doi.org/10.1017/njg.2015.23.

Jia, X., M. G. Kivelson, K. K. Khurana, and R. J. Walker (Dec. 2024). "Improved Models of Ganymede's Permanent and Induced Magnetic Fields Based on Galileo and Juno Data". In: *Journal of Geophysical Research: Planets* 130.1. ISSN: 2169-9100. DOI: https://doi.org/10.1029/2024JE008309.

Kamata, S., J. Kimura, K. Matsumoto, F. Nimmo, K. Kuramoto, and N. Namiki (2016). "Tidal deformation of Ganymede: Sensitivity of Love numbers on the interior structure". In: *Journal of Geophysical Research: Planets* 121.7, pp. 1362–1375. DOI: 10.1002/2016JE005071.

Kaula, W. M. (1968). *An introduction to planetary physics. The terrestrial planets*. Wiley. ISBN: 978-0471460701.

Kaula, W. M. (Nov. 1964). "Tidal dissipation by solid friction and the resulting orbital evolution". In: *Reviews of Geophysics* 2.4, pp. 661–685. ISSN: 1944-9208. DOI: 10.1029/RG002i004p00661.

Kivelson, M., K. Khurana, and M. Volwerk (June 2002). "The Permanent and Inductive Magnetic Moments of Ganymede". In: *Icarus* 157.2, pp. 507–522. ISSN: 0019-1035. DOI: 10.1006/icar.2002.6834.

Kivelson, M., K. Khurana, C. Russell, R. Walker, J. Warnecke, F. Coroniti, C. Polanskey, D. Southwood, and G. Schubert (1996). "Discovery of Ganymede's magnetic field by the Galileo spacecraft". In: *Nature* 384.6609, pp. 537–541. DOI: 10.1038/384537a0.

Matsuyama, I., F. Nimmo, J. T. Keane, N. H. Chan, G. J. Taylor, M. A. Wieczorek, W. S. Kiefer, and J. G. Williams (2016). "GRAIL, LLR, and LOLA constraints on the interior structure of the Moon". In: *Geophysical Research Letters* 43.16, pp. 8365–8375. DOI: 10.1002/2016GL069952.

Moore, W. B. and G. Schubert (Sept. 2000). "The Tidal Response of Europa". In: *Icarus* 147.1, pp. 317–319. ISSN: 0019-1035. DOI: doi:10.1006/icar.2000.6460.

Moore, W. B. and G. Schubert (2003). "The tidal response of Ganymede and Callisto with and without liquid water oceans". In: *Icarus* 166.1, pp. 223–226. DOI: 10.1016/j.icarus.2003.07.001.

Murray, C. D. and S. F. Dermott (Feb. 2000). "Solar System Dynamics". In: DOI: 10.1017/CBO9781139174817.

National Academies of Sciences, E., Medicine, et al. (Oct. 2023). "Origins, Worlds, and Life: A Decadal Strategy for Planetary Science and Astrobiology 2023-2032". In: DOI: https://doi.org/10.17226/26522.

Nelson, B., E. B. Ford, and M. J. Payne (Dec. 2013). "RUN DMC: AN EFFICIENT, PARALLEL CODE FOR ANALYZING RADIAL VELOCITY OBSERVATIONS USING N -BODY INTEGRATIONS AND DIFFERENTIAL EVOLUTION MARKOV CHAIN MONTE CARLO". In: *The Astrophysical Journal Supplement Series* 210.1, p. 11. ISSN: 1538-4365. DOI: 10.1088/0067-0049/210/1/11.

Nimmo, F. and R. T. Pappalardo (2016). "Ocean worlds in the outer solar system". In: *Journal of Geophysical Research: Planets* 121.8, pp. 1378–1399. DOI: 10.1002/2016JE005081.

Padovan, S., T. Spohn, P. Baumeister, N. Tosi, D. Breuer, S. Csizmadia, H. Hellard, and F. Sohl (Dec. 2018). "Matrix-propagator approach to compute fluid Love numbers and applicability to extrasolar planets". In: *Astronomy and Astrophysics* 620, A178. ISSN: 1432-0746. DOI: 10.1051/0004-6361/201834181.

Pappalardo, R. T., G. C. Collins, J. Head, P. Helfenstein, T. B. McCord, J. M. Moore, L. M. Prockter, P. M. Schenk, and J. R. Spencer (2004). "Geology of ganymede". In: *Jupiter: The planet, satellites and magnetosphere* 2, p. 363.

Petricca, F., A. Genova, J. C. Castillo-Rogez, M. J. Styczinski, C. J. Cochrane, and S. Vance (2023). "Characterization of icy moon hydrospheres through joint inversion of gravity and magnetic field measurements". In: *Geophysical Research Letters* 50.17, e2023GL104016. DOI: 10.1029/2023GL104016.

Rambaux, N., T. Van Hoolst, and Ö. Karatekin (Feb. 2011). "Librational response of Europa, Ganymede, and Callisto with an ocean for a non-Keplerian orbit". In: *Astronomy and Astrophysics* 527, A118. ISSN: 1432-0746. DOI: 10.1051/0004-6361/201015304.

Roache, P. J. (Jan. 1997). "QUANTIFICATION OF UNCERTAINTY IN COMPUTATIONAL FLUID DYNAMICS". In: *Annual Review of Fluid Mechanics* 29.1, pp. 123–160. ISSN: 1545-4479. DOI: 10.1146/annurev.fluid.29.1.123.

Rovira-Navarro, M., I. Matsuyama, and A. Berne (May 2024). "A Spectral Method to Compute the Tides of Laterally Heterogeneous Bodies". In: *The Planetary Science Journal* 5.5, p. 129. ISSN: 2632-3338. DOI: 10.3847/psj/ad381f.

Rovira-Navarro, M., I. Matsuyama, and H. C. C. Hay (2023). "Thin-shell tidal dynamics of ocean worlds". In: *The Planetary Science Journal* 4.2, p. 23. DOI: 10.3847/PSJ/acae9a.

Sabadini, R., B. Vermeersen, and G. Cambiotti (2016). "Global Dynamics of the Earth: Applications of Viscoelastic Relaxation Theory to Solid-Earth and Planetary Geophysics". In: DOI: 10.1007/978-94-017-7552-6.

Saur, J., S. Duling, L. Roth, X. Jia, D. F. Strobel, P. D. Feldman, U. R. Christensen, K. D. Retherford, M. A. McGrath, F. Musacchio, A. Wennmacher, F. M. Neubauer, S. Simon, and O. Hartkorn (Mar. 2015). "The search for a subsurface ocean in Ganymede with Hubble Space Telescope observations of its auroral ovals". In: *Journal of Geophysical Research: Space Physics* 120.3, pp. 1715–1737. ISSN: 2169-9402. DOI: 10.1002/2014JA020778.

Schubert, G., J. Anderson, T. Spohn, and W. B. McKinnon (2004). "Interior composition, structure and dynamics of the Galilean satellites". In: *Jupiter: The planet, satellites and magnetosphere* 1. ISBN: 0-521-81808-7, pp. 281–306.

Schubert, G., K. Zhang, M. G. Kivelson, and J. D. Anderson (1996). "The magnetic field and internal structure of Ganymede". In: *Nature* 384.6609, pp. 544–545. DOI: 10.1038/384544a0.

Seufert, M., J. Saur, and F. M. Neubauer (2011). "Multi-frequency electromagnetic sounding of the Galilean moons". In: *Icarus* 214.2, pp. 477–494. DOI: 10.1016/j.icarus.2011.03.017.

Sohl, F., T. Spohn, D. Breuer, and K. Nagel (2002). "Implications from Galileo observations on the interior structure and chemistry of the Galilean satellites". In: *Icarus* 157.1, pp. 104–119. DOI: 10.1006/icar.2002.6828.

Spohn, T. and G. Schubert (Feb. 2003). "Oceans in the icy Galilean satellites of Jupiter?" In: *Icarus* 161.2, pp. 456–467. ISSN: 0019-1035. DOI: 10.1016/s0019-1035(02)00048-9.

Steinbrügge, G., A. Stark, H. Hussmann, F. Sohl, and J. Oberst (Nov. 2015). "Measuring tidal deformations by laser altimetry. A performance model for the Ganymede Laser Altimeter". In: *Planetary and Space Science* 117, pp. 184–191. ISSN: 0032-0633. DOI: http://dx.doi.org/10.1016/j.pss.2015.06.013.

Steinbrügge, G., T. Steinke, R. Thor, A. Stark, and H. Hussmann (July 2019). "Measuring Ganymede's Librations with Laser Altimetry". In: *Geosciences* 9.7, p. 320. ISSN: 2076-3263. DOI: https://doi.org/10.3390/geosciences9070320.

Styczinski, M. J., S. Vance, E. M. Harnett, and C. J. Cochrane (2022). "A perturbation method for evaluating the magnetic field induced from an arbitrary, asymmetric ocean world analytically". In: *Icarus* 376, p. 114840. DOI: 10.1016/j.icarus.2021.114840.

Styczinski, M. J., S. Vance, and M. Melwani Daswani (2023). "PlanetProfile: Self-Consistent Interior Structure Modeling for Ocean Worlds and Rocky Dwarf Planets in Python". In: *Earth and Space Science* 10.8, e2022EA002748. DOI: 10.1029/2022EA002748.

ter Braak, C. J. F. and J. A. Vrugt (Oct. 2008). "Differential Evolution Markov Chain with snooker updater and fewer chains". In: *Statistics and Computing* 18.4, pp. 435–446. ISSN: 1573-1375. DOI: https://doi.org/10.1007/s11222-008-9104-9.

The pandas development team (2025). "pandas-dev/pandas: Pandas". In: DOI: https://doi.org/10.5281/zenodo.3509134.

Tobie, G., P. Auclair-Desrotour, M. Běhounková, M. Kervazo, O. Souček, and K. Kalousová (2025). "Tidal Deformation and Dissipation Processes in Icy Worlds". In: *Space Science Reviews* 221.1, pp. 1–57. DOI: 10.1007/s11214-025-01136-y.

Van Hoolst, T., R.-M. Baland, and A. Trinh (2013). "On the librations and tides of large icy satellites". In: *Icarus* 226.1, pp. 299–315. DOI: 10.1016/j.icarus.2013.05.036.

Van Hoolst, T., R.-M. Baland, A. Trinh, M. Yseboodt, and F. Nimmo (Aug. 2020). "The Librations, Tides, and Interior Structure of Io". In: *Journal of Geophysical Research: Planets* 125.8. ISSN: 2169-9100. DOI: 10.1029/2020JE006473.

Van Hoolst, T., G. Tobie, C. Vallat, N. Altobelli, L. Bruzzone, H. Cao, D. Dirkx, A. Genova, H. Hussmann, L. Iess, J. Kimura, K. Khurana, A. Lucchetti, G. Mitri, W. Moore, J. Saur, A. Stark, A. Vorburger, M. Wieczorek, A. Aboudan, J. Bergman, F. Bovolo, D. Breuer, P. Cappuccio, L. Carrer, B. Cecconi, G. Choblet, F. De Marchi, M. Fayolle, A. Fienga, Y. Futaana, E. Hauber, W. Kofman, A. Kumamoto, V. Lainey, P. Molyneux, O. Mousis, J. Plaut, W. Puccio, K. Retherford, L. Roth, B. Seignovert, G. Steinbrügge, S. Thakur, P. Tortora, F. Tosi, M. Zannoni, S. Barabash, M. Dougherty, R. Gladstone, L. I. Gurvits, P. Hartogh, P. Palumbo, F. Poulet, J.-E. Wahlund, O. Grasset, and O. Witasse (July 2024). "Geophysical Characterization of the Interiors of Ganymede, Callisto and Europa by ESA's JUpiter ICy moons Explorer". In: *Space Science Reviews* 220.5. ISSN: 1572-9672. DOI: 10.1007/s11214-024-01085-y.

van Zelst, I., F. Crameri, A. E. Pusok, A. Glerum, J. Dannberg, and C. Thieulot (Mar. 2022). "101 geodynamic modelling: how to design, interpret, and communicate numerical studies of the solid Earth". In: *Solid Earth* 13.3, pp. 583–637. ISSN: 1869-9529. DOI: https://doi.org/10.5194/se-13-583-2022.

Vance, S., M. P. Panning, S. Stähler, F. Cammarano, B. G. Bills, G. Tobie, S. Kamata, S. Kedar, C. Sotin, W. T. Pike, et al. (2018). "Geophysical investigations of habitability in ice-covered ocean worlds". In: *Journal of Geophysical Research: Planets* 123.1, pp. 180–205. DOI: 10.1002/2017JE005338.

Vance, S., M. Styczinski, B. Bills, C. Cochrane, K. Soderlund, N. Gómez-Pérez, and C. Paty (2021). "Magnetic induction responses of Jupiter's ocean moons including effects from adiabatic convection". In: *Journal of Geophysical Research: Planets* 126.2, e2020JE006418. DOI: 10.1029/2020JE006418.

Vance, S., M. Bouffard, M. Choukroun, and C. Sotin (2014). "Ganymede's internal structure including thermodynamics of magnesium sulfate oceans in contact with ice". In: *Planetary and Space Science* 96, pp. 62–70. ISSN: 0032-0633. DOI: 10.1016/j.pss.2014.03.011.

Virtanen, P., R. Gommers, T. E. Oliphant, M. Haberland, T. Reddy, D. Cournapeau, E. Burovski, P. Peterson, W. Weckesser, J. Bright, S. J. van der Walt, M. Brett, J. Wilson, K. J. Millman, N. Mayorov, A. R. J. Nelson, E. Jones, R. Kern, E. Larson, C. J. Carey, İ. Polat, Y. Feng, E. W. Moore, J. VanderPlas, D. Laxalde, J. Perktold, R. Cimrman, I. Henriksen, E. A. Quintero, C. R. Harris, A. M. Archibald, A. H. Ribeiro, F. Pedregosa, P. van Mulbregt, and SciPy 1.0 Contributors (2020). "SciPy 1.0: Fundamental Algorithms for Scientific Computing in Python". In: *Nature Methods* 17, pp. 261–272. DOI: 10.1038/s41592-019-0686-2.

Wahr, J. M., M. T. Zuber, D. E. Smith, and J. I. Lunine (Dec. 2006). "Tides on Europa, and the thickness of Europa's icy shell". In: *Journal of Geophysical Research: Planets* 111.E12. ISSN: 0148-0227. DOI: 10.1029/2006JE002729.

Weijermars, R. (1997). *Principles of rock mechanics*. Alboran Science Publishing. ISBN: 9789056740023.

A

Planning

The following work packages are identified and planned to be carried out in the next 8 months.

1. [**WP1**] **Literature Research:** This work package involves the review of the existing literature on Ganymede's interior structure, magnetic field, tidal response, and librations, as well as on the Bayesian inversion methodology. The review will be used to develop a comprehensive understanding of the problem and to identify the gaps in the existing knowledge.
2. [**WP2**] **Ganymede's Interior Model:** This work package involves the development of an interior model of Ganymede according to subsection 2.1.1. It can be further divided into the following sub-packages.
   - 2.1 [**WP2.1**] Definition of the different layers.
   - 2.2 [**WP2.2**] Definition of the parameters of interest for each layer.
   - 2.3 [**WP2.3**] Definition of plausible ranges for each parameter value.
   - 2.4 [**WP2.4**] Computation of the constrained parameters.
   - 2.5 [**WP2.5**] Verification.
3. [**WP3**] **Forward Model:** This work package involves building the forward model used to generate synthetic data for magnetic induction, tidal response and librations of Ganymede. It can be further divided into the following sub-packages. The procedure follows the methodology described in chapter 2.
   - 3.1 [**WP3.1**] Magnetic Induction Data (subsection 2.1.2).
   - 3.2 [**WP3.2**] Tidal Response (subsection 2.1.3).
   - 3.3 [**WP3.3**] Librations (subsection 2.1.4).
   - 3.4 [**WP3.4**] Validation.
4. [**WP4**] **Sensitivity analysis:** This work package involves the sensitivity analysis of the different observations to variations in the interior parameters. The following sub-packages are identified.
   - 4.1 [**WP4.1**] Impact of parameters variations on the constrained parameters: This package focuses on how the constrained parameters vary with changes in the interior parameters. This step is useful for a preliminary analysis of plausible interior models of Ganymede.
   - 4.2 [**WP4.2**] Impact of parameters variations on Ganymede's responses: This package analyzes how the different observations change with variations in the interior parameters. This step is useful for understanding the sensitivity of the data to the interior properties and for identifying the most influential parameters.
   - 4.3 [**WP4.3**] Definition of model parameters: Identification of the parameters to be retrieved in the Bayesian inversion and their ranges. These parameters will be the ones that have the highest influence on the expected measurements.

5. [**WP5**]: **Bayesian Inversion:** This work package involves the application of Bayesian inversion to the combined data sets. It can be divided into the following sub-packages.

   5.1 [**WP5.1**] Problem Formulation.

      5.1.1 [**WP5.1.1**] Definition of the prior distributions and likelihood functions.

      5.1.2 [**WP5.1.2**] Definition of the sampling method and setup of the sampler: This includes the definition of settings such as the number of walkers, the length of the chains, the moves to use, and the burn-in period.

   5.2 [**WP5.2**] Inversion with currently available observations.

      5.2.1 [**WP5.2.1**] Inversion with gravity data.

      5.2.2 [**WP5.2.2**] Inversion with gravity and magnetic induction data.

   5.3 [**WP5.3**] Inversion with future Juice observations.

      5.3.1 [**WP5.3.1**] Benchmark interior model: Definition of a benchmark interior model, which will be used to generate synthetic data for Ganymede's tidal response and libration.

      5.3.2 [**WP5.3.2**] Synthetic data generation: Generation of synthetic data for Ganymede's tidal response and libration using the forward model developed in [**WP3**].

      5.3.3 [**WP5.3.3**] Inversion with gravity, magnetic induction and tidal observations.

      5.3.4 [**WP5.3.4**] Inversion with gravity, magnetic induction, tidal and libration observations (*not achieved*).

6. **Thesis Reporting:** This task is not identified as a work package itself since it will be carried out in parallel with the other work packages. However, a significant amount of time will be allocated to the writing of the thesis towards the end of the project.

A Work Breakdown Structure (WBS) of the work packages is shown in Figure A.1. An estimated timeline for the completion of the project is shown in the Gantt chart in Figure A.2. In the planning, buffer time, holidays and other contingencies are included. With the described planning, the project is expected to be completed by October 2025.

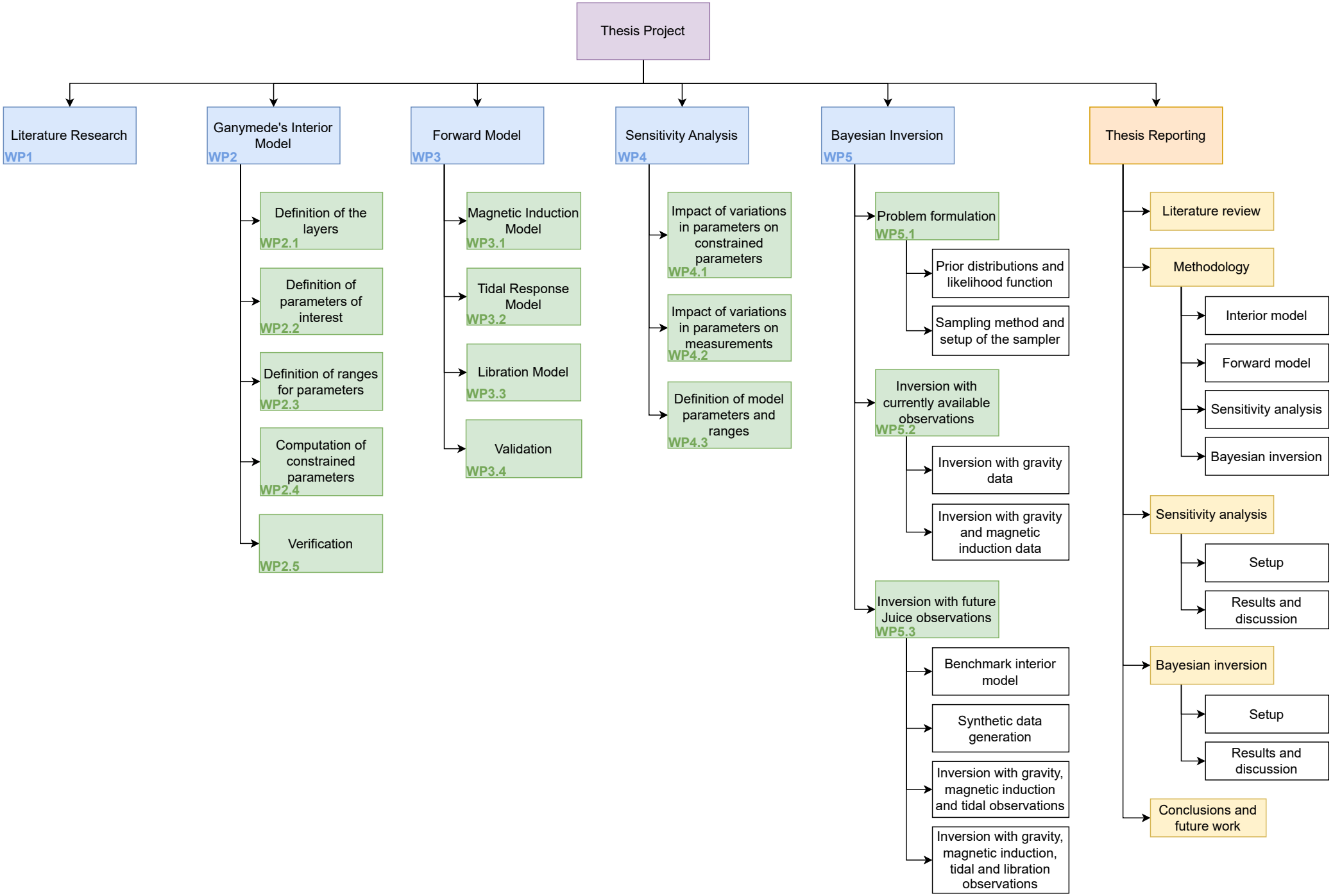

Figure A.1: Work Breakdown Structure

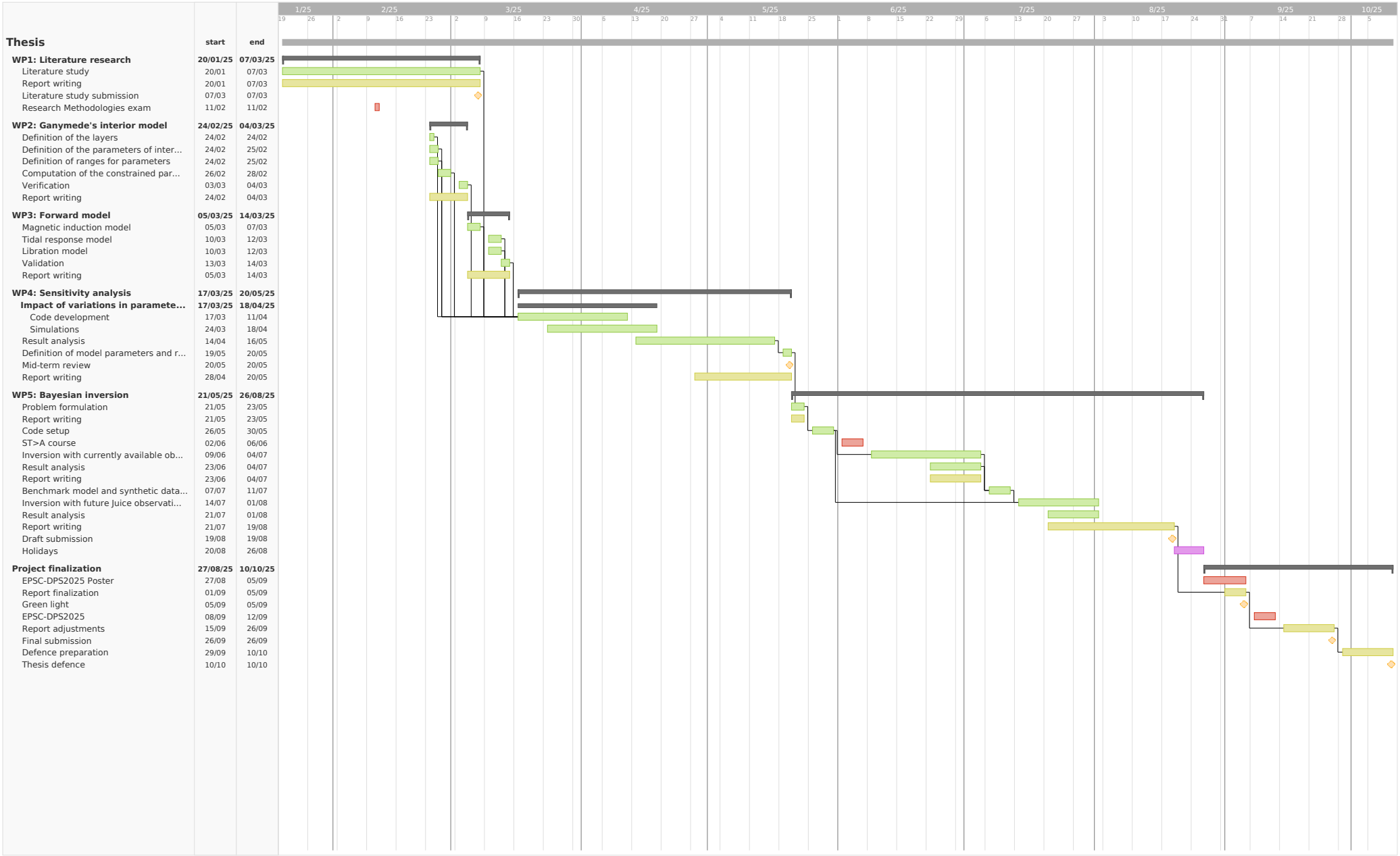

Figure A.2: Gantt Chart

B

Background Knowledge

B.1. Gravitational Field

The gravity field of a celestial body can be described by the Legendre expansion in spherical harmonics of its gravitational potential function Φ:

$$\Phi(r,\phi,\lambda) = -\frac{GM}{r}\sum_{n=0}^{\infty}\left(\frac{R}{r}\right)^n \sum_{m=0}^{n}\left[C_{nm}\cos(m\lambda) + S_{nm}\sin(m\lambda)\right] P_{nm}(\sin\phi) \tag{B.1}$$

The resulting gravitational force can be expressed as the opposite of the gradient of the potential function. In the reference frame of the body, r, ϕ, and λ are the spherical coordinates of the point at which the potential is evaluated. P_{nm} are the associated Legendre polynomials, while C_{nm} and S_{nm} are the gravitational coefficients. These coefficients represent mass properties of the body, and they can be divided in three subsets, each with a specific name (Eckman et al., 2016):

- $J_n = -C_{n0}$ are the zonal coefficients
- C_{nn} and S_{nn} $(n = m)$ are the sectorial coefficients
- C_{nm} and S_{nm} $(n \neq m)$ are the tesseral coefficients

This terminology reflects the geometrical representation of the corresponding spherical harmonic. Depending on how the sign of the harmonic changes, different patterns are formed on the spherical surface, as shown in Figure B.1: zones, sectors, and tesserae (i. e., "tiles"), from which the corresponding names are derived. For more details on the Legendre expansion and spherical harmonics, refer to Hofmann-Wellenhof et al. (2006).

Due to the presence of the term $(R/r)^n$, the gravitational potential is dominated by the lowest-degree terms. In addition, the coefficients up to degree and order two have an easily interpretable physical meaning. C_{00} represents the monopole, and it corresponds to the gravitational potential of a point mass. The higher degree and order coefficients are related to the distribution of mass within the body, and they describe the deviations of the body's gravity field from that of a homogeneous sphere. The first-degree terms describe the offset of the center of mass from the chosen frame origin. If the origin of the coordinate system coincides with the center of mass of the body, the coefficients of degree $n = 1$ are zero. The second-degree terms describe the gravitational quadrupole moment and give information about the shape and mass distribution of the body. The coefficient $J_2 = -C_{20}$ describes the effect of the equatorial bulge, C_{21} and S_{21} describe the tilt of the body's rotation axis with respect to the principal axis of inertia, while C_{22} and S_{22} represent equatorial asymmetries and mass variations.

The gravitational field of a body affects trajectories of spacecrafts, which are deflected as the body is approached. Thus, by measuring these deflections, the gravitational field can be inferred. The Galileo spacecraft's radio communication system, from which the Deep Space Network (DSN) produced Doppler

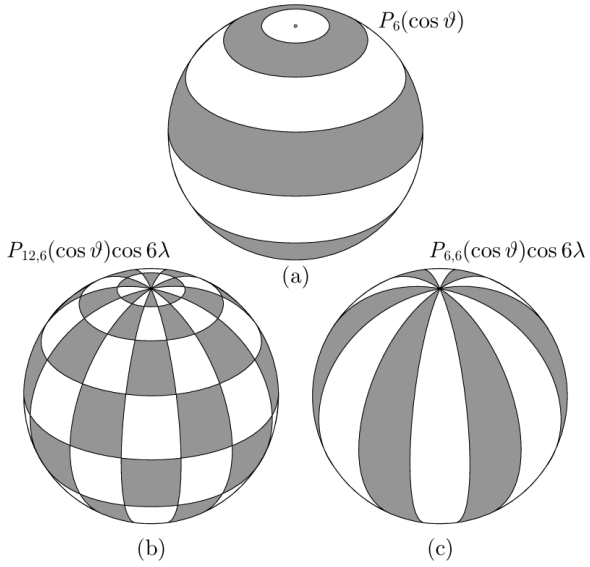

Figure B.1: Representation of different spherical harmonics: (a) zonal, (b) tesseral, and (c) sectorial. Image credit: Hofmann-Wellenhof et al. (2006, Chapter 1, page 18).

data, has been used to calculate the mass and gravitational quadrupole moments of the four Galilean satellites (Schubert et al., 2004).

For the purpose of this study, the only gravitational parameters of interest are the monopole GM, and the two quadrupole coefficients J_2 and C_{22}, which are determined through weighted least-squares fits to the Galileo Doppler data. These terms can be linked to the principal moments of inertia of the body as follows:

$$J_2 = \frac{2\bar{I} - \bar{B} - \bar{A}}{2MR^2} \qquad\qquad C_{22} = \frac{\bar{B} - \bar{A}}{4MR^2} \tag{B.2}$$

where $\bar{I}$ is the axial or polar moment of inertia, $\bar{A}$ and $\bar{B}$ are the equatorial moments of inertia, and $\bar{I} > \bar{B} > \bar{A}$ (Schubert et al., 2004).

However, these two coefficients are not independent. The extent to which they are linked is indicated by a statistical correlation coefficient μ. If this value is close to unity, the body can be considered to be in (or close to) hydrostatic equilibrium and the relation between the two coefficients is:

$$J_2 = \frac{10}{3} C_{22} \tag{B.3}$$

This correlation can be explained in the light of the moon's rotational and tidal response, which can be described by the fluid Love number k_f multiplied by a rotational and a tidal parameter, q_r and q_t respectively (Schubert et al., 2004).

$$k_\mathrm{f}\, q_\mathrm{r} = -3(2C_{22} - J_2) \qquad\qquad k_\mathrm{f}\, q_\mathrm{t} = -12C_{22} \tag{B.4}$$

q_r is computed as:

$$q_\mathrm{r} = \frac{\omega^2 R^3}{GM} \tag{B.5}$$

From these quantities, under the assumption of a body in rotational and tidal equilibrium, the C_{22} coefficient can be obtained as (Schubert et al., 2004):

$$C_{22} = \frac{1}{4} k_\mathrm{f} q_\mathrm{r} \tag{B.6}$$

The Radau relationship links the moment of inertia factor I/MR^2 to the fluid love number k_f, which can be obtained from C_{22} and q_r (Kaula, 1968):

$$I/MR^2 = \frac{2}{3}\left[1 - \frac{2}{5}\left(\frac{4 - k_\mathrm{f}}{1 + k_\mathrm{f}}\right)^{1/2}\right] \tag{B.7}$$

Therefore, from the gravitational parameters GM and C_{22}, the total mass of the body and its moment of inertia factor can be computed and used as constraints for the interior models.

B.2. Tides

The gravitational pull from a planet varies across the interior of its satellite, creating a forcing field that causes the satellite to deform. This tidal forcing field creates an elongation in the satellite along the direction of the planet, forming a tidal bulge. If the satellite always presented the same face to the planet, the bulge would remain fixed. Due to non-synchronous rotation, elliptical orbits, and non-zero obliquities, the bulge moves relative to the planet, leading to periodic deformations and internal heating.

The tidal energy is mostly converted into heat through viscous friction within the satellite's viscoelastic interior. The efficiency of this process depends on the satellite's internal thermal state and it is quantified by the tidal quality factor Q. In the case of Ganymede, two opposite effects influence the satellite's orbit. On one hand, tidal dissipation acts to circularize its orbit and synchronize its rotation with its revolution. On the other hand, the 1:2:4 Laplace resonance with Io and Europa increases the eccentricity of its orbit, allowing for a non-zero eccentricity despite the presence of the tidal dissipation.

The tidal potential at a certain point on the surface of the satellite can be expressed as a series of spherical harmonics (Sabadini et al., 2016):

$$\Phi^T = -\frac{GM}{d^*} \sum_{l=0}^{\infty} \left(\frac{r}{d^*}\right)^l P_l\left(\cos\Psi\right) \tag{B.8}$$

The resulting tidal forces can be expressed as the opposite of the gradient of the tidal potential. Note that, due to character limitation, the symbols in this section differ from those used in the rest of the document and are defined as follows:

- M: Mass of the tide-raising body
- d^*: Distance between the bodies' center of mass
- r: Radial distance from the center of the satellite
- P_l: Legendre polynomial of spherical harmonic degree l
- Ψ: Angle between the satellite's position vector and the position vector of a point on the surface of the satellite

Expressing Ψ in terms of latitude and longitude of the end points of the position vectors, and using the addition theorem, the tidal potential can be written as (Kaula, 1964):

$$\Phi^T = -\frac{GM}{d^*} \sum_{l=2}^{\infty} \left(\frac{r}{d^*}\right)^l \sum_{m=0}^{l} \frac{(l-m)!}{(l+m)!}(2-\delta_{0m}) P_{lm}(\cos\theta^*) P_{lm}(\cos\theta)[\cos(m\varphi^*)\cos(m\varphi)+\sin(m\varphi^*)\sin(m\varphi)] \tag{B.9}$$

where:

- θ^*: Co-latitude of the tide-raising body
- φ^*: Longitude of the tide-raising body
- θ: Co-latitude of the point on the satellite's surface
- φ: Longitude of the point on the satellite's surface

The tidal potential can be expressed in terms of Keplerian elements of the satellite's orbit (Kaula, 1964):

$$\left(\frac{1}{d^*}\right)^{l+1} P_l(\cos\theta^*)\cos(m\varphi^*) = \left(\frac{1}{a^*}\right)^{l+1} \sum_{p=0}^{l} F_{lmp}(i^*) \sum_{q=-\infty}^{\infty} G_{lpq}(e^*)\cos m\varphi \begin{cases} \cos v^*_{lmpq}, & l-m \text{ even} \\ \sin v^*_{lmpq}, & l-m \text{ odd} \end{cases} \tag{B.10}$$

$$\Phi^T = -\frac{GM}{a^*}\sum_{l=2}^{\infty}\left(\frac{r}{a^*}\right)^l \sum_{m=0}^{l}\frac{(l-m)!}{(l+m)!}(2-\delta_{0m})P_{lm}(\cos\theta)\sum_{p=0}^{l}\sum_{q=-\infty}^{\infty}F_{lmp}(i^*)G_{lpq}(e^*)\left[\cos m\varphi\begin{cases}\cos v^*_{lmpq}, & l-m \text{ even}\\ \sin v^*_{lmpq}, & l-m \text{ odd}\end{cases}\right] \tag{B.11}$$

where:

- a^*: Semi-major axis
- e^*: Eccentricity
- i^*: Obliquity
- l: Degree
- m: Order
- $G_{lpq}(e^*)$: Eccentricity functions
- $F_{lmp}(i^*)$: Inclination functions
- $v^*_{lmpq} = (l-2p)\omega^* + (l-2p+q)M^* + m\gamma^* - m\varphi^*_0$ (Tidal angle)
- γ: Longitude of the ascending node
- ω: Argument of pericenter
- M^*: Mean anomaly
- φ^*_0: Longitude reference meridian
- n^*: Orbital frequency

Similarly to the gravitational potential, due to the term $(r/a^*)^l$, the tidal potential is dominated by the second-degree harmonic. With the assumption that eccentricity and inclination are small, the expression can be simplified, and static and time-varying components can be identified.

The static tidal potential represents the potential acting on the satellite if its orbit was circular, its rotation synchronous, and its obliquity zero (Sabadini et al., 2016):

$$\Phi^T_0 = -\frac{GMr^2}{a^{*3}}\left\{-\frac{1}{2}P_{20}(\cos\theta) + \frac{1}{4}P_{22}(\cos\theta)\cos(2\varphi)\right\} \tag{B.12}$$

The time-varying tidal potential resulting from non-zero eccentricity and obliquity are respectively given by (Jara Orue, 2016):

$$\Phi^T_e(t) = -\frac{GMr^2}{a^{*3}}e^*\left\{-\frac{3}{2}P_{20}(\cos\theta)\cos(n^*t) + \frac{1}{4}P_{22}(\cos\theta)\left[3\cos(n^*t)\cos(2\varphi) + 4\sin(n^*t)\sin(2\varphi)\right]\right\} \tag{B.13}$$

$$\Phi^T_i(t) = -\frac{GMr^2}{a^{*3}}\sin i^* P_{21}(\cos\theta)\cos(\varphi)\sin(\omega + n^*t) \tag{B.14}$$

These different tidal perturbations cause displacements and stresses in the body, which lead to tidal dissipation. The tidal Love numbers describe the body's viscoelastic response to an external forcing caused by the primary body. In the case of a spherically symmetric body, the Love numbers do not depend on the order m, and the response of the body will be of the same degree l as the forcing (Rovira-Navarro et al., 2024). Therefore, we can denote the Love numbers as k_l (gravitational), h_l (radial), and l_l (poloidal).

The different tidal potentials give rise to responses at different time scales, and therefore different Love numbers are used. Over long time scales, the static tidal potential causes a static deformation in the body, which is close to that of a body in hydrostatic equilibrium. In this case, the deformation is described by the so-called fluid Love numbers, which only depend on the density distribution of the body. Considering only the second-degree harmonic, the perturbed potential Φ_p at the surface is expressed in terms of the fluid Love number k_f as (Padovan et al., 2018):

$$\Phi_p = -k_\mathrm{f}\Phi^T_0 \tag{B.15}$$

The displacement u_r at the surface is described by the fluid Love number h_f as (Padovan et al., 2018):

$$u_r = -\frac{h_f}{g_{\text{surf}}}\Phi_0^T \tag{B.16}$$

Since the body is in hydrostatic equilibrium and can be approximated as a fluid, the surface is an equipotential surface, which is defined by the sum of the external potential Φ_0^T and the perturbed potential Φ_p (Padovan et al., 2018):

$$u_r = -\frac{1+k_{\text{f}}}{g_{\text{surf}}}\Phi_0^T \tag{B.17}$$

Therefore, the fluid Love numbers satisfy the relation:

$$h_f = 1 + k_{\text{f}} \tag{B.18}$$

On the other hand, the time-varying tidal potential caused by the eccentricity and inclination of the satellite's orbit leads to periodic deformations in the body at much shorter time scales. In this case, the Love numbers that describe the body's response are frequency-dependent complex numbers that depend on the body's interior structure, rehology and period of the exerted force. Mass displacements in the interior of the satellite cause variations in the tidal potential, described by k_l, while the surface displacements are described by h_l and l_l, respectively in the radial and lateral directions (Hussmann et al., 2016).

In case of a purely elastic body, the imaginary parts of the Love numbers, i. e., the phase lags, are zero, while for viscoelastic responses the phase lag of the tidal potential ν_{k_n} and of the radial deformation ν_{h_n} describe the time delay between the tidal potential and the body's response.

Considering the second-degree harmonic, the perturbed potential Φ_p and the radial deformation u_r are related to the tidal potential by the Love numbers k_2 and h_2 as:

$$\Phi_p = -k_2\Phi^T \qquad\qquad u_r = -\frac{h_2}{g_{\text{surf}}}\Phi^T \tag{B.19}$$

B.3. Bayesian Inference

The scientific method is an iterative process that aims to infer the laws of nature through observation, hypothesis formulation, and experimental testing, as schematically represented in Figure B.2. However, real-world data are inherently incomplete, and experimental results rarely provide definitive yes-or-no answers. This uncertainty requires statistical inference, which allows scientists to make reasoned conclusions based on limited information.

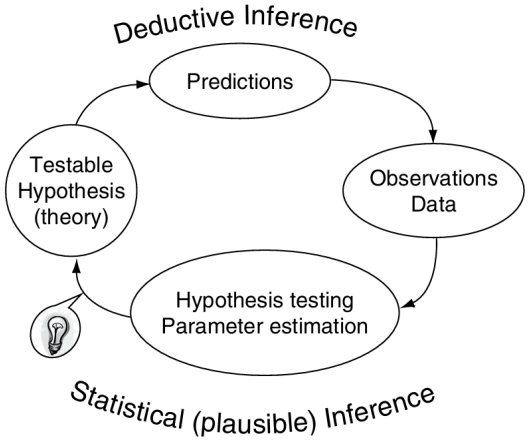

Figure B.2: Scientific method. Image credit: Gregory (2005, Chapter 1, page 2).

Traditional statistical approaches, often referred to as frequentist methods, define probability as the long-run relative frequency of an event occurring in identical experimental repeats (Gregory, 2005).

While useful for handling random errors in measurements, this framework struggles with addressing the probability of hypotheses or model parameters.

A more general framework for statistical inference, the Bayesian probability theory, has gained increasingly more importance in modern science. Unlike frequentist statistics, Bayesian inference treats probability as a measure of plausibility based on prior knowledge and observed data. This approach allows for a direct computation of the probability of a hypothesis or parameter value, offering a consistent method to update our beliefs taking new evidence into consideration (Gregory, 2005).

In Bayesian analysis, probability distributions represent uncertainty, and inference is conducted through Bayes' theorem, which updates prior beliefs with new data to produce posterior probabilities. This method aligns with the logic of scientific reasoning, where theories evolve as new observations improve our understanding. Bayesian inference thus provides a natural extension of deductive and inductive reasoning, integrating prior knowledge with empirical data in a coherent manner.

In Bayesian probability theory, the plausibility of certain hypotheses or model parameters is expressed as the probability of these quantities given observed data and prior information. In many scientific applications, the aim is not to compare different hypotheses but rather to estimate the parameters of a given model. Bayesian inference provides a framework for this process by treating the parameters as continuous random variables with associated probability distributions.

In the following, we denote a model as $\bar{M}$, its parameters as $\mathbf{X}$, the observed data as $\mathbf{\Theta}$ and any prior information as I. We identify different quantities:

- The prior probability $p(\mathbf{X}|\bar{M}, I)$, which represents our knowledge about the model parameters before observing the data.
- The likelihood function $p(\mathbf{\Theta}|\mathbf{X}, \bar{M}, I)$, which quantifies the probability of observing the data given the model parameters.
- The posterior probability $p(\mathbf{X}|\mathbf{\Theta}, \bar{M}, I)$, which represents our knowledge about the model parameters after observing the data.
- The global likelihood $p(\mathbf{\Theta}|\bar{M}, I)$, which quantifies the overall probability of observing the data.

Bayes' theorem relates these quantities as follows:

$$p(\mathbf{X}|\mathbf{\Theta}, \bar{M}, I) = \frac{p(\mathbf{\Theta}|\mathbf{X}, \bar{M}, I) \times p(\mathbf{X}|\bar{M}, I)}{p(\mathbf{\Theta}|\bar{M}, I)} \tag{B.20}$$

As shown in Gregory (2005, Chapter 3, Equation 3.7), the global likelihood acts as a normalization constant. We can therefore define $C = 1/p(\mathbf{\Theta}|\bar{M}, I)$ and rewrite Equation B.20 as:

$$p(\mathbf{X}|\mathbf{\Theta}, \bar{M}, I) = C \times p(\mathbf{\Theta}|\mathbf{X}, \bar{M}, I) \times p(\mathbf{X}|\bar{M}, I) \tag{B.21}$$

The posterior probability is also referred to as the joint posterior probability and concerns the entire parameter space. For any subset of parameters $\mathbf{X}_i$, the marginal posterior probability is obtained by integrating over the remaining parameters:

$$p(\mathbf{X}_i|\mathbf{\Theta}, \bar{M}, I) = \int p(\mathbf{X}|\mathbf{\Theta}, \bar{M}, I)\, \mathrm{d}\mathbf{X}_j \quad \text{for} \quad j = 1, 2, \ldots, N \quad \text{and} \quad j \neq i \tag{B.22}$$

where N is the total number of parameters.

Unlike frequentist methods, which provide single best-fit estimates, Bayesian inference yields the entire posterior distribution. Statistical quantities, such as the posterior mean and posterior mode, can then be used to report parameter estimates in terms of best-fit values and associated uncertainties. Another key concept in Bayesian parameter estimation is the credible interval, which represents the range within which the true parameter value is likely to fall with a given probability.

In many cases, models include parameters that influence the observed data but are not of primary interest. These are referred to as nuisance parameters. Bayesian inference allows to handle nuisance

parameters through a process known as marginalization. This involves integrating out the unwanted parameters to obtain a marginalized posterior distribution for the parameters of interest:

$$p(\bar{\mathbf{X}}|\boldsymbol{\Theta}, \bar{M}, I) = \int p(\bar{\mathbf{X}}, \mathbf{X}_n|\boldsymbol{\Theta}, \bar{M}, I)\, \mathrm{d}\mathbf{X}_n \tag{B.23}$$

where $\mathbf{X}_n$ represents the nuisance parameters and $\bar{\mathbf{X}}$ the parameters of interest. This ensures that the final inference about $\bar{\mathbf{X}}$ accounts for all possible values of $\mathbf{X}_n$, weighted by their probability.

C

Verification and Validation

Verification and validation are crucial steps in the development of any software, as they ensure that the software meets its requirements and performs as expected. According to the ECSS standard, verification is the "process to confirm that adequate specifications and inputs exist for any activity, and that the outputs of the activities are correct and consistent with the specifications and input" (European Cooperation for Space Standardization, 2009), while validation is the "process to confirm that the requirements baseline functions and performances are correctly and completely implemented in the final product" (European Cooperation for Space Standardization, 2009). In short, verification means "solving the equations right", while validation means "solving the right equations" (Roache, 1997).

Code verification involves the use of tests and benchmarks to ensure the correctness and reliability of numerical models (van Zelst et al., 2022). Tests are typically designed to evaluate specific parts of the code, particularly under extreme or limiting conditions, and are used to verify both the numerical implementation and overall functionality. Unit tests are especially useful for validating the correctness of individual subroutines. When analytical solutions are available, they provide a reliable reference for comparison. In cases where analytical solutions are not possible, "community benchmarks" offer an alternative approach (van Zelst et al., 2022). These benchmarks involve different codes developed to solve the same model setup, allowing for direct comparison and cross-verification of results.

The code verification process is described in section C.1. This include verifying the implementation of the interior model described in subsection 2.1.1 to ensure that all the subroutines and modules work as intended. Section C.2 presents the validation of the forward models described in subsection 2.1.2, subsection 2.1.3 and subsection 2.1.4 by comparing the obtained output with benchmark cases from literature.

C.1. Verification

The process to build the interior model of Ganymede is described in subsection 2.1.1 and is summarized in Figure 2.3. It mainly consists of six functions:

- a function to compute the interior profiles of mass, gravity and pressure;
- a function to interpolate tabulated phase diagrams and determine the intersections of the pressure profile with the ice-ocean interface and ocean floor;
- a function to compute the ocean density;
- a function to compute the ocean conductivity;
- a function to compute the core and mantle densities based on Ganymede's mass and MoI;
- a function to compute the bulk moduli of the layers from the shear moduli and Poisson's ratio.

The verification process includes testing the correctness of these functions, ensuring they produce the expected results and handle edge cases correctly.

C.1.1. Core and mantle densities

Given the thicknesses and densities of the layers, the mass and MoI of Ganymede are computed with Equation 2.6 and Equation 2.7, respectively. When constructing the interior model, we invert these equations to compute the core and mantle densities based on Ganymede's total mass and MoI. This function is verified using the analytical expressions for mass and MoI. We use the nominal parameters listed in Table D.1a and the constrained parameters from Table D.1b, which are computed numerically, to analytically evaluate the mass and MoI of Ganymede's layers and verify that they match the numerically computed values.

Equation 2.6 and Equation 2.7 can be written for a single spherical layer as:

$$M_{\text{layer}} = \frac{4}{3}\pi\rho_{\text{layer}}\left(r_{\text{outer}}^3 - r_{\text{inner}}^3\right) \tag{C.1}$$

$$\bar{I}_{\text{layer}} = \frac{8}{15}\pi\rho_{\text{layer}}\left(r_{\text{outer}}^5 - r_{\text{inner}}^5\right) \tag{C.2}$$

Note that the polar moment of inertia $\bar{I}$ is reported without normalization, as it refers to a single layer. Both the numerical and analytical results for Ganymede's mass and MoI are summarized in Table C.1.

Table C.1: Mass and MoI of Ganymede's layers computed using the nominal parameters listed in Table D.1a and the corresponding constrained parameters in Table D.1b. Here, the polar moment of inertia $\bar{I}$ is reported without normalization. The total analytical values are computed by summing the contributions of all layers.

Layer	Numerical M [10^{23} kg]	Analytical M [10^{23} kg]	Numerical $\bar{I}$ [10^{35} kg m^{-2}]	Analytical $\bar{I}$ [10^{35} kg m^{-2}]
Core	0.0690	0.0690	0.0107	0.0107
Mantle	0.8362	0.8362	1.1799	1.1799
HP ice	0.3712	0.3712	1.1416	1.1416
Ocean	0.1136	0.1136	0.4577	0.4577
Ice shell	0.0916	0.0916	0.4056	0.4056
Total	1.4816	1.4816	3.1955	3.1955

The results show that the numerical and analytical values for both mass and MoI match, which verifies the correctness of the implementation.

C.1.2. Interior profiles

To find the ocean boundaries from interpolation of the phase diagram, the mass, gravity and pressure profiles of Ganymede are computed as explained in subsection 2.1.1. The computation of the mass profile is verified by comparing the mass at each layer's boundary with the analytical mass computed using Equation C.1.

The results are summarized in Table C.2. Since the mass profile is computed iteratively, the mass at each boundary takes into account the mass of all layers below it, not just the mass of the layer itself. Therefore, the reported values are the cumulative mass of all layers up to that boundary, and the analytical values are computed by summing the contributions of all layers below that boundary. The results show that the errors in the numerical values, compared to the analytical ones, are below 0.15 % for all layers, and even smaller for the upper layers, which are of interest when interpolating the phase diagram. Therefore, we can consider the numerical implementation of the mass profile to be verified.

The pressure and gravity profiles are shown in Figure C.1a. At the center of Ganymede, according to Equation 2.3, the gravitational acceleration is zero. At the surface, using the values reported in Table 1.1, the gravitational acceleration is $g_{\text{surf}} = 1.4280\ \text{m s}^{-2}$. The gravity profile gives a gravitational acceleration at the surface of $g_{\text{surf}} = 1.4285\ \text{m s}^{-2}$, which is within 0.0350 % of the expected value.

The interior profiles obtained in this work are compared to those computed by Sohl et al. (2002), shown in Figure C.1b for three different core compositions. The nominal parameters used here result in a core density of approximately 6860 kg m^{-3}, which lies between the densities of a core composed of 50 % Fe

Table C.2: Masses of Ganymede's internal layers, obtained from the numerical computation of the interior profile, and from analytical calculations using the nominal parameters in Table D.1a and the corresponding constrained parameters in Table D.1b. The variation between the numerical and analytical values is reported in percentage of the analytical value.

Layer	Numerical M [10^{23} kg]	Analytical M [10^{23} kg]	$\frac{M_{\mathrm{num}}-M_{\mathrm{an}}}{M_{\mathrm{an}}} \times 100$ [%]
Core	0.0691	0.0690	0.1449
Mantle	0.9056	0.9052	0.0442
HP ice	1.2769	1.2764	0.0392
Ocean	1.3906	1.3901	0.0360
Ice shell	1.4822	1.4817	0.0337

and 50 % FeS, and a core composed of 100 % Fe. However, Sohl et al. (2002) do not provide the exact thicknesses and densities of each layer, which prevents a direct quantitative comparison. Additionally, their model includes multiple HP phases, while we only consider a single HP phase of 1200 kg m^{-3} density. Therefore, the profiles shown in Figure C.1a and Figure C.1b are not directly equivalent, but they are qualitatively similar, showing the same trends across the different layers. Taking this into account, along with the checks at the interfaces performed previously, we consider the implementation of the interior profiles to be verified.

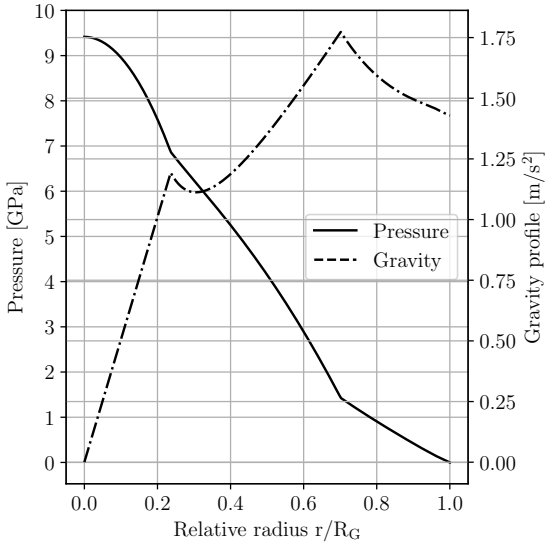

(a) Pressure and gravity profiles within Ganymede's interior for the nominal parameters' values listed in Table D.1a and the corresponding constrained parameters.

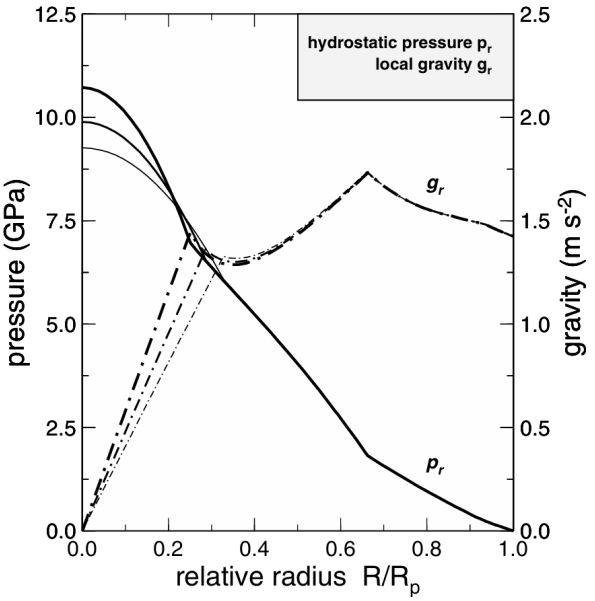

(b) Pressure and gravity profiles within Ganymede's interior for three different core compositions (bold curve: 100 % Fe; normal curve: 50 % Fe and 50 % FeS; light curve: 100 % FeS). Image credit: Sohl et al. (2002, Fig. 10).

C.1.3. Phase diagram interpolation

To compute the ocean boundaries, tabulated phase diagrams of $MgSO_4$ solutions are used. Given certain ice density and thickness, the pressure profile within the ice layer is computed and the value at the bottom of the layer is used to interpolate the phase diagram to obtain the temperature at the ice-ocean interface. This value is then used to compute the pressure at the ocean floor, which is assumed to be at the same temperature as the ice-ocean interface for a fully convective ocean.

A test function is implemented to verify the correctness of the interpolation function. The test function selects a profile with a certain $wt\%$ from the dataset and chooses a pressure value from the dataset as the interpolation input. This pressure represents the pressure at the bottom of the ice shell and is used in the interpolation function, which returns the temperature at the ice-ocean interface and the pressure at the ocean floor. The interpolated temperature is compared against the tabulated temperature at

the chosen pressure. This temperature value has two pressure values associated with it, one for the ice-ocean interface and one for the ocean floor. The latter is used to verify the interpolated pressure value. The test confirms that the interpolated values match the original dataset. Figure C.2 is used visually confirm the alignment.

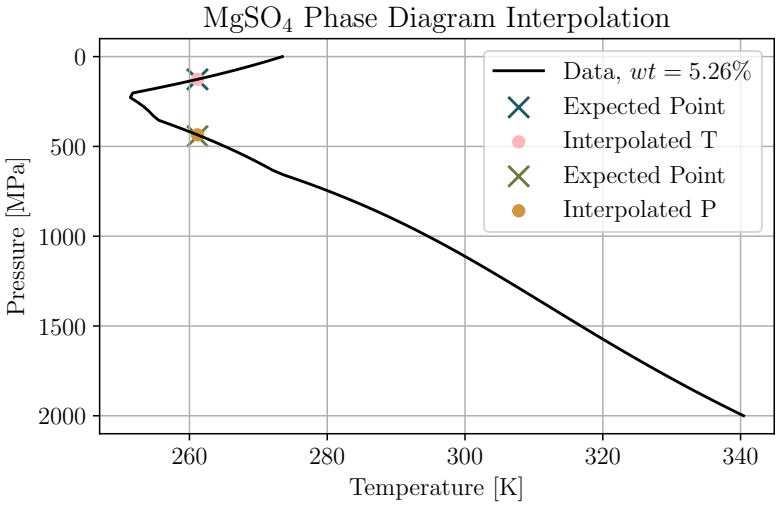

Figure C.2: Verification of the phase diagram interpolation function.

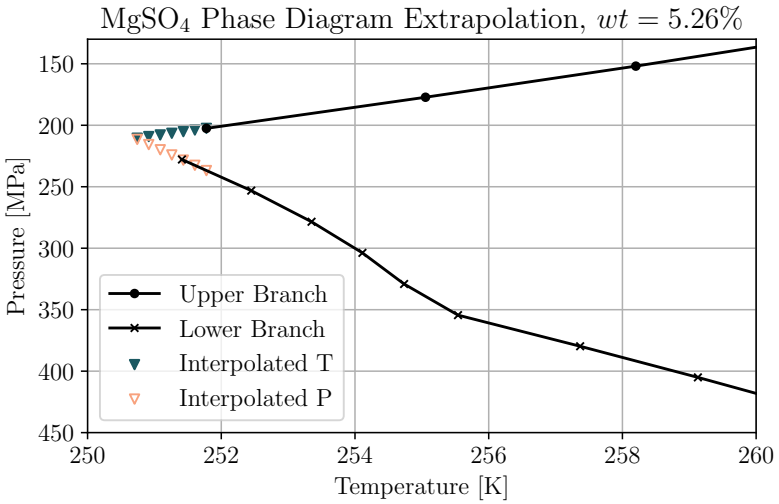

Figure C.3: Verification of the phase diagram interpolation function outside of the tabulated domain.

Since the dataset consists of discrete points, special attention must be paid to edge cases, particularly near the triple point. As shown in Figure C.3, the available data points do not span the entire range of pressures and temperatures up to the triple point. Therefore, values outside the tabulated domain are extrapolated.

Although the extrapolation provides results for any input value, the interpolation function returns an error if the pressure at the bottom of the ocean is lower than the pressure at the ice-ocean interface (i. e., the triple point has been exceeded). Figure C.3 shows the verification of the extrapolation behavior of the interpolation function. The test procedure selects pressure values beyond the maximum pressure available in the upper branch of the phase diagram and evaluates the interpolation function at these points. The resulting temperatures and pressures follow the expected trend of the phase diagram. As expected, the function returns an error once the triple point is exceeded.

C.1.4. Ocean density computation

The density of the ocean layer is computed using a function that interpolates $MgSO_4$ equation-of-state spline data (Styczinski et al., 2023) over molality, pressure, and temperature.

To verify its correctness, a test function selects known values of molality, pressure, and temperature from the EOS dataset. The corresponding weight percentage is computed using the molality and $MgSO_4$ molar mass. The function is then called with this weight percentage, and the interpolated density is compared with the directly tabulated density value. The test confirms that the interpolated result matches the tabulated value.

C.1.5. Ocean conductivity computation

The ocean conductivity is computed from Equation 2.1 (Hand et al., 2007). Since it is an equation of degree three, it has three roots, out of which one is negative and two are positive. The negative root is discarded, and comparing it with Hand et al. (2007, Fig. 1), the lower positive root is the one that corresponds to the ocean conductivity.

The verification is performed by visually comparing the computed conductivity with the trend and values shown in Hand et al. (2007). Figure C.4 shows the computed conductivity as a function of concentration of $MgSO_4$ in the ocean, which agrees with the values reported in Hand et al. (2007, Fig. 1).

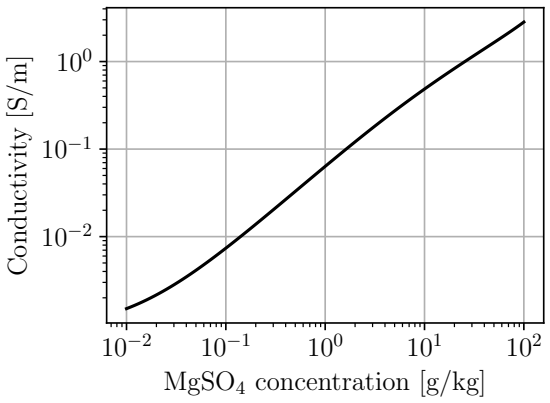

Figure C.4: Conductivity of the ocean as a function of the concentration of $MgSO_4$ obtained from Equation 2.1. The concentration is computed as $C = wt \times 10$. The plotted values correspond to the lower positive root of the cubic equation.

C.1.6. Bulk moduli computation

The bulk moduli of the compressible layers are computed from the shear moduli and Poisson's ratio using Equation 2.8. Comparing the results with the analytical values, we verify the correctness of the implementation.

Table C.3: Bulk moduli of Ganymede's layers computed using the nominal parameters listed in Table D.1a and the corresponding constrained parameters in Table D.1b. The analytical values are computed using Equation 2.8 with the same parameters.

	Numerical value [GPa]	Analytical value [GPa]
K_{ma}	182.5490	182.5490
K_{hp}	8.6059	8.6059
K_{ice}	8.6059	8.6059

C.2. Validation

After code verification, the next step is to validate the models against literature data. Specifically, we validate the forward models described in subsection 2.1.2, subsection 2.1.3 and subsection 2.1.4 by comparing the obtained output with benchmark cases from the literature.

C.2.1. Magnetic Induction Response

To validate the magnetic induction implementation, we apply the model to the benchmark case of Vance et al. (2021). The interior model parameters of interest and their values are listed in Table C.4. From these parameters, the ones needed in Equation 2.9 are directly computed.

Table C.4: Interior model parameters from Vance et al. (2021).

Parameter	Values	Unit
D_{ice}	50	km
D_{o}	10^{0} to 10^{3}	km
κ_{o}	10^{-1} to 10^{2}	$\text{S}\,\text{m}^{-1}$

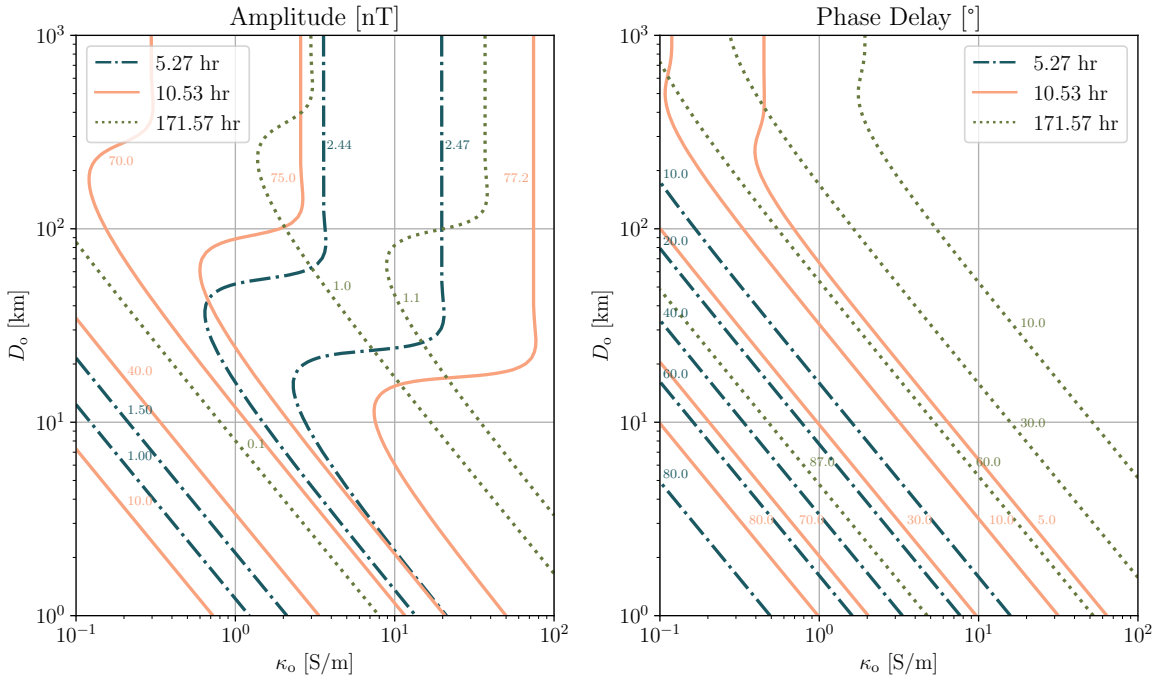

Figure C.5: Magnetic induction amplitude and phase delay of the maximum induced field B_y at the three periods with strongest induction (Vance et al., 2021), computed with the parameters listed in Table C.4 and the model described in subsection 2.1.2.

The magnetic induction amplitude and phase delay are shown in Figure C.5 for the three periods with the strongest induction. Comparing these plots with Figure 4 in Vance et al. (2021), we can confirm that the results of our model are in good agreement with the ones of Vance et al. (2021). We can therefore conclude that the implementation of the magnetic induction model is validated.

C.2.2. Tidal Response

To validate the model used to compute the tidal response, we compare the results with the benchmark cases of Jara-Orué et al. (2016) and Hussmann et al. (2016) for the real and imaginary parts of the tidal Love numbers, respectively.

Table C.5 lists the interior model parameters used to compute the tidal response. The values of the fixed parameters are taken from Table 1 in Jara-Orué et al. (2016), while the ranges of the variable parameters are selected from Table 2 in Jara-Orué et al. (2016). Here, a six-layer model is used, with a ductile ice shell and an elastic crust. The obtained Love numbers are shown in Figure C.6. By comparing the results with Figures 1 and 2 in Jara-Orué et al. (2016), we can confirm that the real part of the tidal Love numbers h_2 and k_2 is correctly computed.

Table C.5: Interior model parameters from Jara-Orué et al. (2016). The outer ice shell is divided into a ductile ice shell and an elastic crust. The outer radius of Ganymede is 2634 km. The core and mantle densities are computed to satisfy the mass and moment of inertia constraints.

Parameter	Values	Unit
r_{c}	720	km
r_{ma}	1840	km
r_{HP}	2284	km
r_{o}	$[2484, 2496.22, 2508.44, \ldots 2581.78, 2594]$	km
r_{ice}	2614	km
r_{crust}	2634	km
ρ_{hp}	1346	$\mathrm{kg\,m^{-3}}$
ρ_{o}	1100	$\mathrm{kg\,m^{-3}}$
ρ_{ice}	937	$\mathrm{kg\,m^{-3}}$
$\mu_{\mathrm{s,ma}}$	65	GPa
$\mu_{\mathrm{s,hp}}$	6.6	GPa
$\mu_{\mathrm{s,ice}}$	$[1, 3.5, 10]$	GPa
$\mu_{\mathrm{s,crust}}$	3.5	GPa
η_{ma}	1×10^{20}	Pa s
η_{hp}	1×10^{17}	Pa s
η_{ice}	$[1 \times 10^{14}, 1 \times 10^{17}, 1 \times 10^{19}]$	Pa s
η_{crust}	1×10^{21}	Pa s

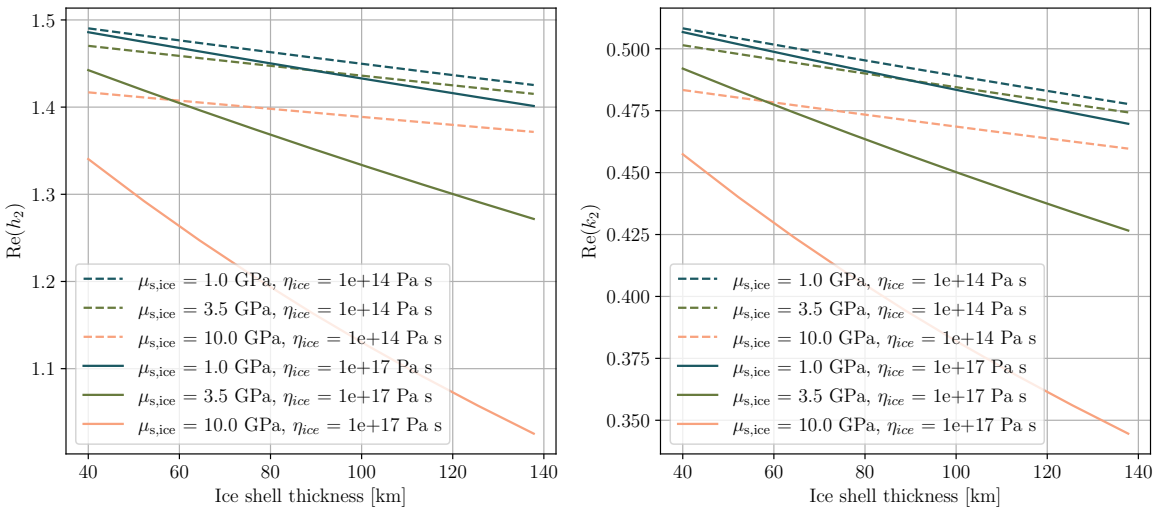

Figure C.6: Real part of the tidal Love numbers h_2 and k_2 as a function of the ice shell thickness for different values of ice shell rigidity and viscosity, as listed in Table C.5.

Table C.6 lists the interior model parameters used in Hussmann et al. (2016) to compute the tidal response. The results are analyzed in terms of phase lag ν of the tidal Love numbers k_2 and h_2, as well as the difference $\Delta\nu = \nu_{k_2} - \nu_{h_2}$. Figure C.7, Figure C.8 and Figure C.9 are equivalent to Figures 2(a), 2(b) and 2(c) in Hussmann et al. (2016), respectively, while Figure C.10 is equivalent to Figure 3 in Hussmann et al. (2016). Comparing the obtained results with the ones of Hussmann et al. (2016), we

Table C.6: Interior model parameters from Hussmann et al. (2016). The elastic crust was not considered here for the tidal response, and a single ice shell was modelled.

Parameter	Values			Unit
	Model			
	1	2	3	
r_c	689	716.4	782.1	km
ρ_c	6500	6500	6500	$kg\,m^{-3}$
r_{ma}	1800	1750	1700	km
ρ_{ma}	3263.2	3345.5	3383	$kg\,m^{-3}$
$\mu_{s,ma}$	50	50	50	GPa
η_{ma}	10×10^{20}	10×10^{20}	10×10^{20}	Pa s
r_{hp}	2350	2400	2450	km
ρ_{hp}	1400	1400	1400	$kg\,m^{-3}$
$\mu_{s,hp}$	6.6	6.6	6.6	GPa
η_{hp}	5×10^{13}	5×10^{13}	5×10^{13}	Pa s
ρ_o	1000	1000	1000	$kg\,m^{-3}$
D_{ice}	140	140	140	km
ρ_{ice}	1000	1000	1000	$kg\,m^{-3}$
$\mu_{s,ice}$	3.3	3.3	3.3	GPa
η_{ice}	1×10^{14}	1×10^{14}	1×10^{14}	Pa s

can confirm that the imaginary part of the Love numbers is correctly computed. Therefore, we can conclude that the implementation of the tidal response model is validated.

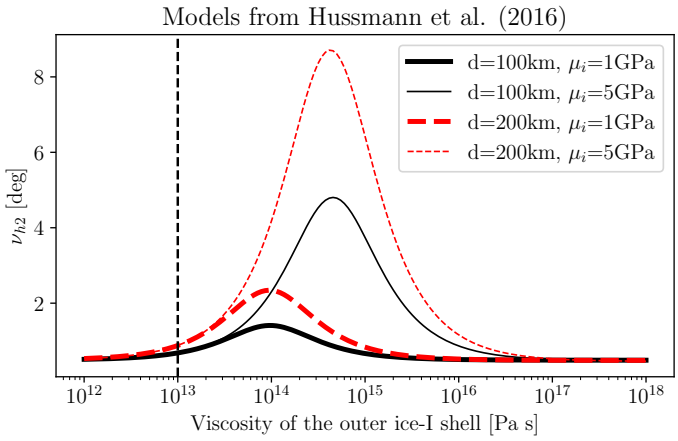

Figure C.7: h_2 phase lag as a function of the ice shell viscosity for model 2 described in Table C.6. Different values for the shear modulus and thickness of the ice shell are considered, as shown in the legend.

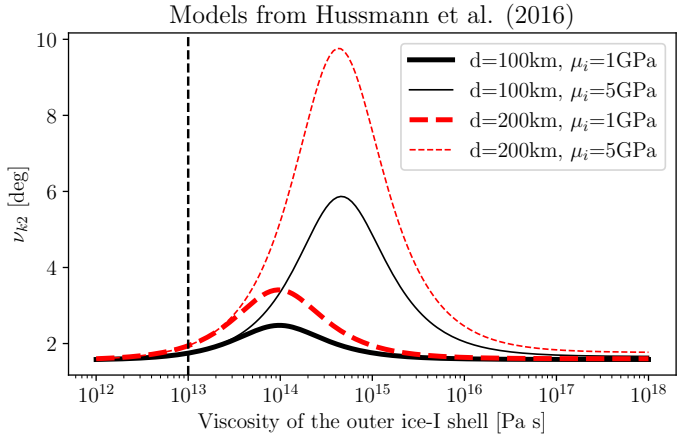

Figure C.8: k_2 phase lag as a function of the ice shell viscosity for model 2 described in Table C.6. Different values for the shear modulus and thickness of the ice shell are considered, as shown in the legend.

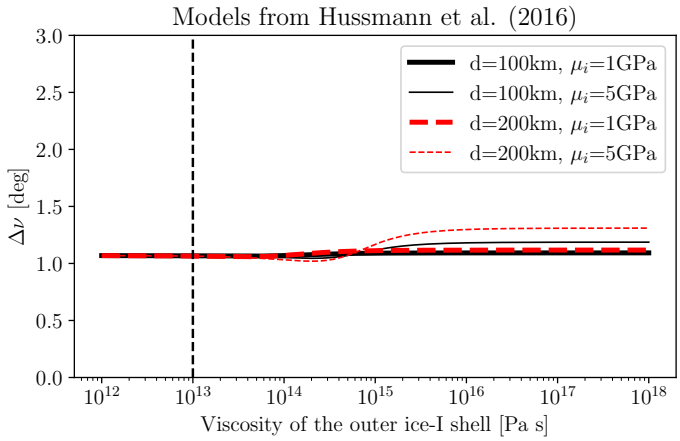

Figure C.9: $\Delta\nu = \nu_{k_2} - \nu_{h_2}$ as a function of the ice shell viscosity for model 2 described in Table C.6. Different values for the shear modulus and thickness of the ice shell are considered, as shown in the legend.

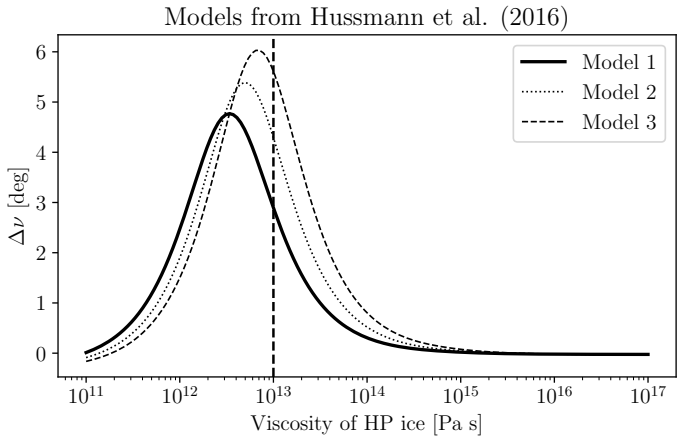

Figure C.10: $\Delta\nu = \nu_{k_2} - \nu_{h_2}$ as a function of the HP ice viscosity for the three models described in Table C.6.

C.2.3. Libration Response

To validate the libration response model, we compare the results with the benchmark cases of Van Hoolst et al. (2013). The interior model parameters listed in Table C.7 are selected to be closely in alignment with the ones used in Van Hoolst et al. (2013). Here, we consider a signle core layer instead of a distinguishing between a solid and a liquid core. Core and mantle densities are computed to satisfy the mass and moment of inertia constraints, while the ocean thickness is calculated from the total radius of Ganymede. Only valid models are selected to compute the libration response. The libration amplitude of the ice shell is shown in Figure C.11 as a function of the ice shell density for the different interior models. Comparing Figure C.11 with Figure 12 in Van Hoolst et al. (2013), we can confirm that the libration amplitude is correctly computed, which validates the libration response model.

Table C.7: Interior model parameters from Van Hoolst et al. (2013).

Parameter	Values	Unit
r_{c}	$[200, 400, 600, 800, 1000, 1200]$	km
r_{ma}	$[1500, 1625, 1750, 1875, 2000]$	km
r_{HP}	$[1900, 2100, 2300, 2500]$	km
D_{ice}	$[25, 50, 75, 100, 150, 200, 300, 400, 500]$	km
ρ_{hp}	$[1000, 1200, 1400]$	$\mathrm{kg\,m^{-3}}$
ρ_{o}	$[800, 900, 1000, 1100, 1200]$	$\mathrm{kg\,m^{-3}}$
ρ_{ice}	$[800, 900, 1000, 1100, 1200]$	$\mathrm{kg\,m^{-3}}$
$\mu_{\mathrm{s,ma}}$	100	GPa
$\mu_{\mathrm{s,hp}}$	4.6	GPa
$\mu_{\mathrm{s,ice}}$	3.3	GPa

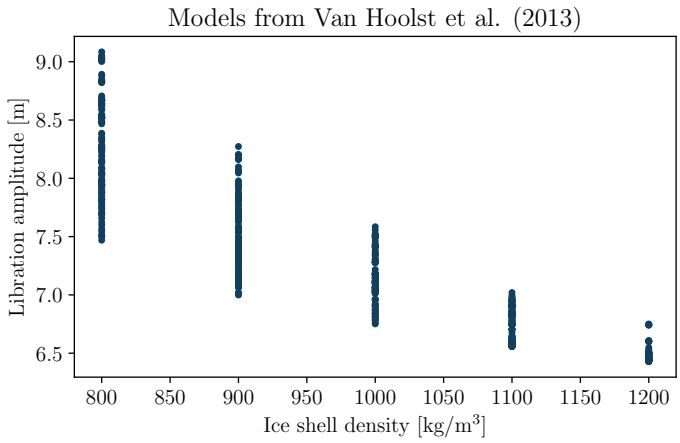

Figure C.11: Ice shell libration amplitude as a function of the ice shell density for different Ganymede's interior models from Van Hoolst et al. (2013).

D

Sensitivity Analysis

This chapter presents the results obtained from the OAT sensitivity analysis and includes additional plots from the MC analysis.

D.1. One-at-a-Time Sensitivity Analysis

D.1.1. Setup

The general setup of the OAT sensitivity analysis is described in section 2.1, where the parameter space defined in Table 2.1 is explored by increasing each variable by a certain step size, while keeping the other parameters fixed at their nominal values, listed in Table D.1a together with the step sizes or number of parameters considered for the sampling. When the number of parameters is specified, the variable is sampled in logarithmic space. Since this preliminary analysis has the goal of understanding general

Table D.1: Free and constrained parameters considered in the OAT sensitivity analysis.

(a) Nominal parameters and corresponding step sizes or number of parameters considered for the OAT sampling.

Free Parameter	Nominal Value	Step	Number of Parameters
r_{c}	621.5 km	1 km	
r_{ma}	1846 km	1 km	
D_{ice}	109.8 km	1 km	
ρ_{hp}	1200 kg m^{-3}	1 kg m^{-3}	
ρ_{ice}	1000 kg m^{-3}	1 kg m^{-3}	
$\mu_{\mathrm{s,ma}}$	70 GPa		100
η_{ma}	1×10^{20} Pa s		500
$\mu_{\mathrm{s,hp}}$	3.3 GPa		100
η_{hp}	1×10^{14} Pa s		500
$\mu_{\mathrm{s,ice}}$	3.3 GPa		100
η_{ice}	1×10^{20} Pa s		500
wt	5 %	0.5 %	
υ	0.33	0.01	

(b) Constrained parameters and corresponding constraints.

Constrained parameter	Constraint	Nominal value
ρ_{c}	Equation 2.6 and 2.7	6864.3902 kg m^{-3}
ρ_{ma}	Equation 2.6 and 2.7	3299.2076 kg m^{-3}
r_{hp}	Phase diagram	2391.3259 km
r_{o}	Total radius	2521.4 km
ρ_{o}	EOS	1152.7547 kg m^{-3}
κ_{o}	Equation 2.1	1.6490 S m^{-1}
K_{ma}	Equation 2.8	182.5490 GPa
K_{hp}	Equation 2.8	8.6059 GPa
K_{ice}	Equation 2.8	8.6059 GPa

behaviors of parameters and main trends in the response instead of obtaining accurate results, when applying the mass and MoI constraints shown in Equation 2.6 and Equation 2.7, we do not sample their values from a Gaussian distribution but rather use the expected values reported in Table 1.1.

The nominal values of the layer thicknesses are based on the default model of Ganymede provided by

the *PlanetProfile* software (Styczinski et al., 2023). The other default values are based on the literature reported in Table 2.1 or selected within the allowable ranges. Interior models are generated according to subsection 2.1.1 and Figure 2.3. For the models that respect the constraints in Table 2.2, the magnetic induction, tidal and libration responses are computed according to subsection 2.1.2, subsection 2.1.3 and subsection 2.1.4 respectively.

D.1.2. Constrained Parameters

In this section, the constrained parameters are analyzed. Figure D.1 to Figure D.5 show the major trends of the constrained parameters as a function of the free parameters.

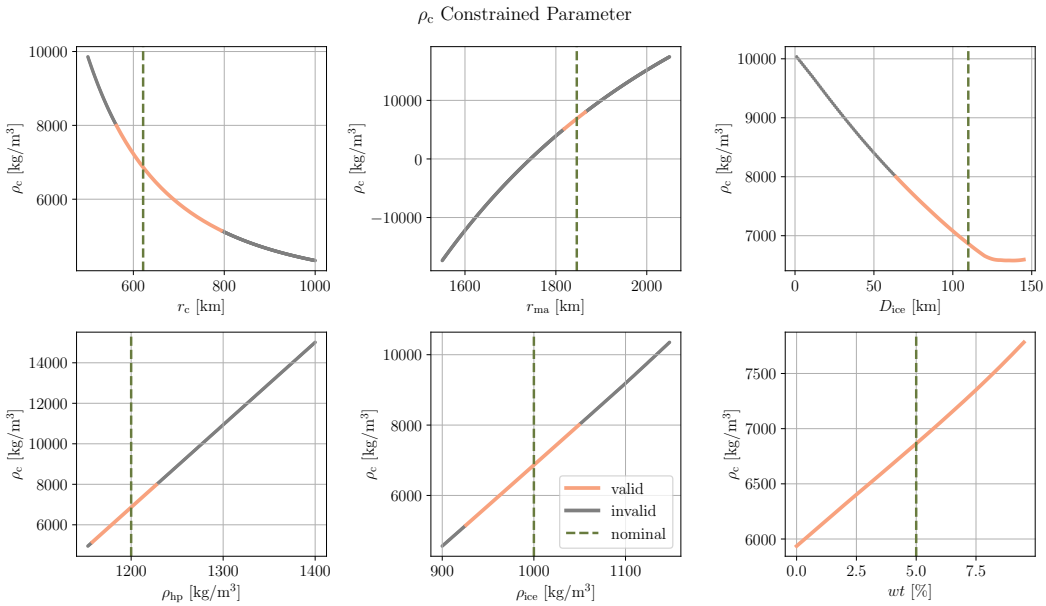

Figure D.1: Density of the core as function of relevant free parameters. The invalid models are shown in gray, while the vertical dashed line indicates the nominal value of the free parameter.

Figure D.1 and Figure D.2 illustrate the core and mantle densities, respectively. Models that violate the imposed constraints are shown in gray, while vertical dashed lines mark the nominal value of each free parameter. These trends are driven by the mass and MoI constraints: when changing the thickness or density of one layer, another parameter must be adjusted to maintain the total mass and MoI of Ganymede.

Figure D.3 shows the ocean thickness and density as a function of the ocean composition and ice shell thickness and density. The ocean thickness is defined from the phase diagram, and from Figure 2.2 it is clear that it decreases with increasing ice shell thickness (e. g., with increasing pressure at the ice-ocean interface). The ocean composition directly effects the phase diagrams, and therefore the ocean parameters, while the ice shell density affects the ocean properties through Equation 2.2. For a fixed shell thickness, increasing the ice shell density results in an increase in the slope of the pressure profile, leading to a higher pressure at the bottom of the ice, and consequently a lower ocean thickness.

Figure D.4 shows the phase diagram of a $MgSO_4$-water solution, along with the mean ocean pressure, calculated as the average of the pressures at the top and bottom of the ocean. The change in slope in the trends of the ocean thickness and density is due to the change in slope of the ice-liquid phase boundary in the phase diagram. Specifically, ice III forms at lower temperatures, while ice V forms at higher temperatures, as shown in Figure 2.2.

Figure D.5 shows the bulk moduli of the mantle, HP ice and ice shell as a function of the layer's rigidity and Poisson's ratio. These trends are expected, as their dependence is defined by Equation 2.8.

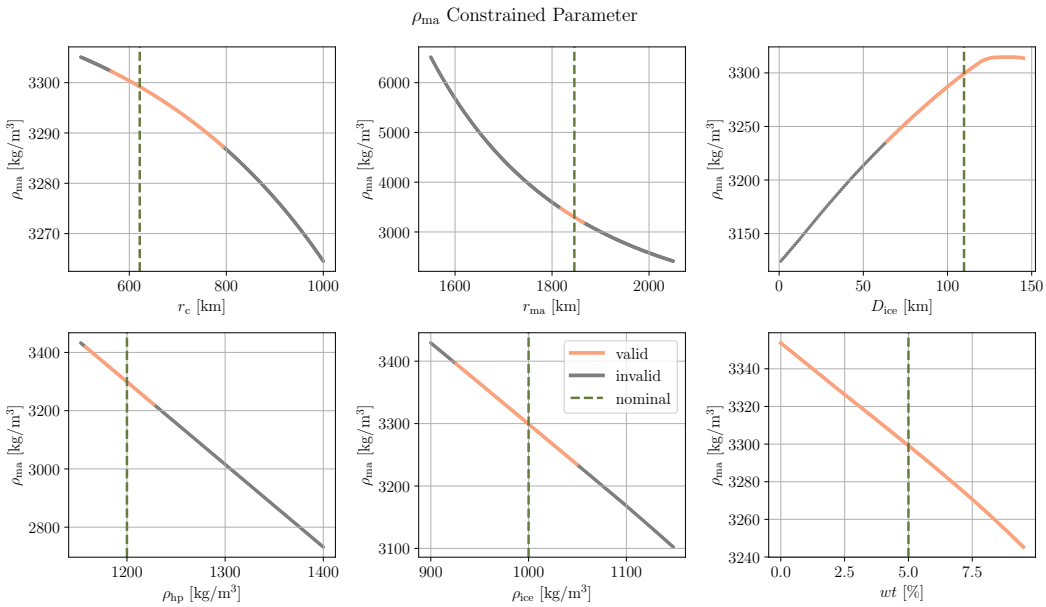

Figure D.2: Density of the mantle as function of relevant free parameters. The invalid models are shown in gray, while the vertical dashed line indicates the nominal value of the free parameter.

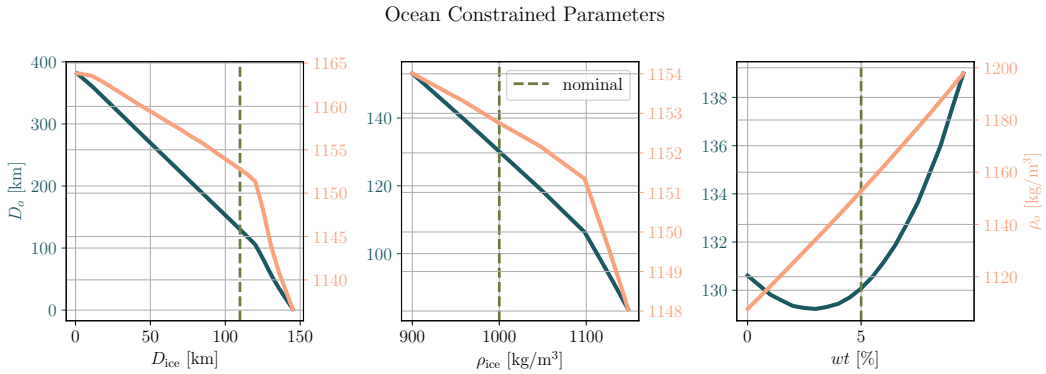

Figure D.3: Ocean thickness (left y axis) and density (right y axis) as a function of the hydrosphere free parameters. All models are shown, and a vertical dashed line indicates the nominal value of the free parameter.

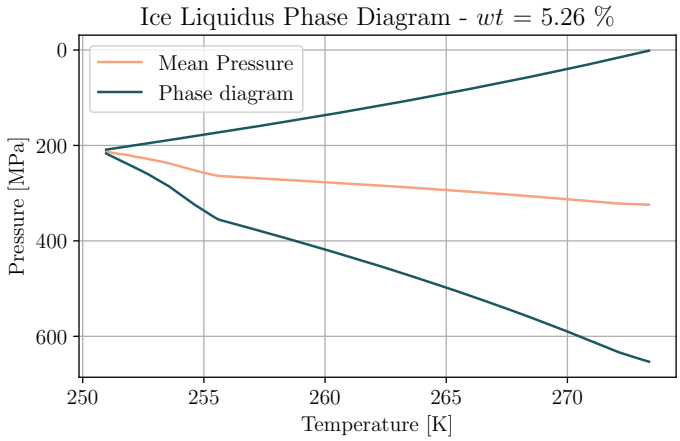

Figure D.4: Portion of the phase diagram of a $MgSO_4$-water solution with $wt = 5.26\%$. The mean pressure used to compute the ocean density is shown in the plot.

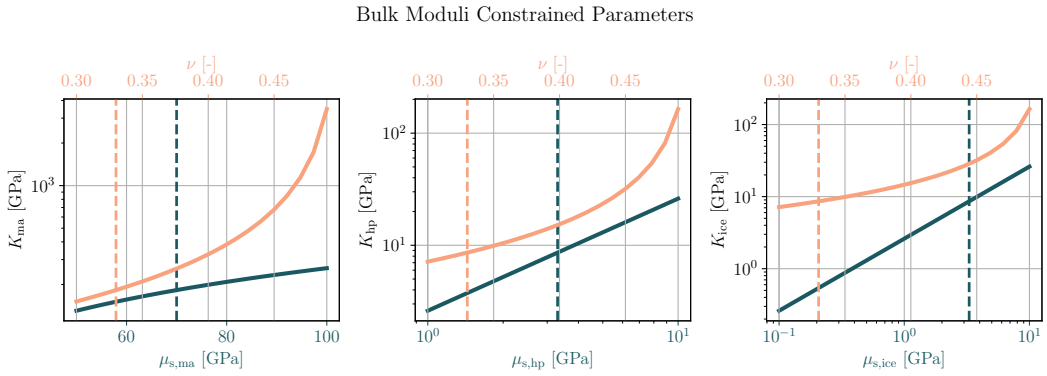

Figure D.5: Bulk moduli of the mantle, HP ice and ice shell as function of the shear moduli and Poisson's ratio. Vertical dashed lines with the same color as the curves indicate the nominal values of the free parameters.

D.1.3. Observations

In this section, we analyze the responses computed for the valid models and their dependence on the free and constrained parameters.

Magnetic Induction Response

Figure D.6 shows the magnetic induction amplitude as a function of the ice shell thickness and ocean composition. The color scales indicate the ocean thickness and conductivity, which are directly defined from the free parameters and are the main contributors to the induction response. For a given ocean composition, the induction response decreases as the ocean gets thinner, while the response amplitude increases with increasing ocean conductivity, with a dominant effect of the ocean thickness. These findings are expected and consistent with Vance et al. (2021), who reported that warmer and thicker oceans yield larger induction responses.

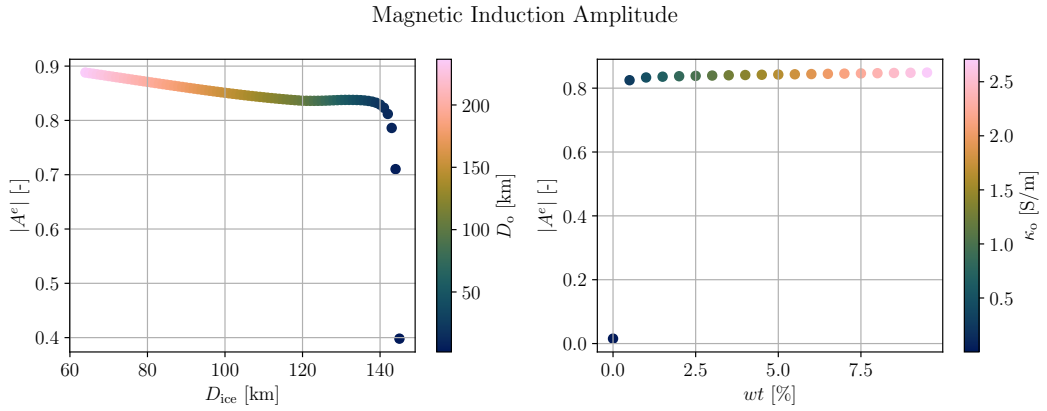

Figure D.6: Magnetic induction amplitude as a function of the ice shell thickness and ocean composition. The subplot on the left shows the corresponding values of the D_o, while the subplot on the right the values of the κ_o.

Figure D.7 shows the variation of the induction amplitude in percentage with respect to the value obtained with the nominal parameters of $|A^e| = 0.8427$. Although the ice shell density is not directly involved in the induction response formulation, its effect is included because it influences ocean thickness through Equation 2.2. These plots indicate that the ocean thickness, controlled by the ice shell thickness, has the largest effect on the induction response, even though Vance et al. (2021) showed that the role of ocean conductivity becomes more significant at longer induction periods.

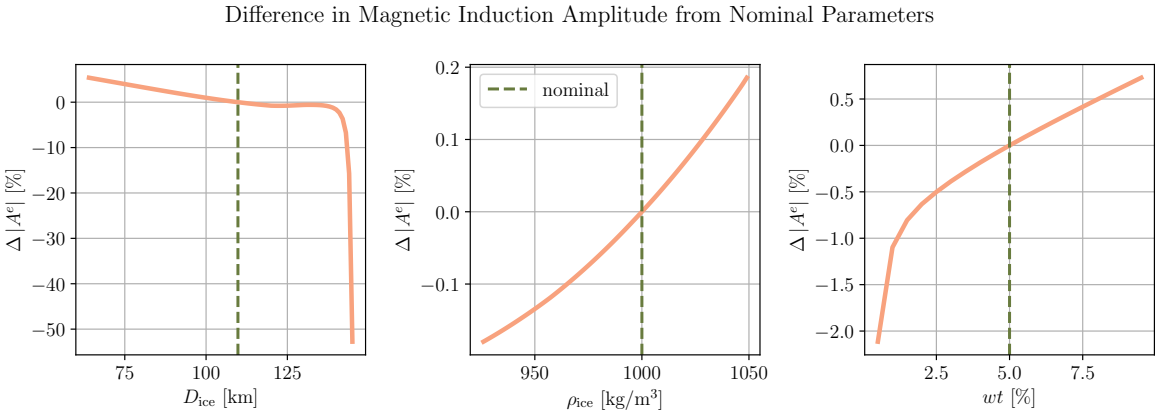

Figure D.7: Variation of the induction amplitude in percentage with respect to the nominal value of $|A^e| = 0.8427$. In the subplot on the right, the first point, corresponding to $wt = 0\%$ is discarded to better visualize the variation of the induction amplitude with wt corresponding to salty oceans.

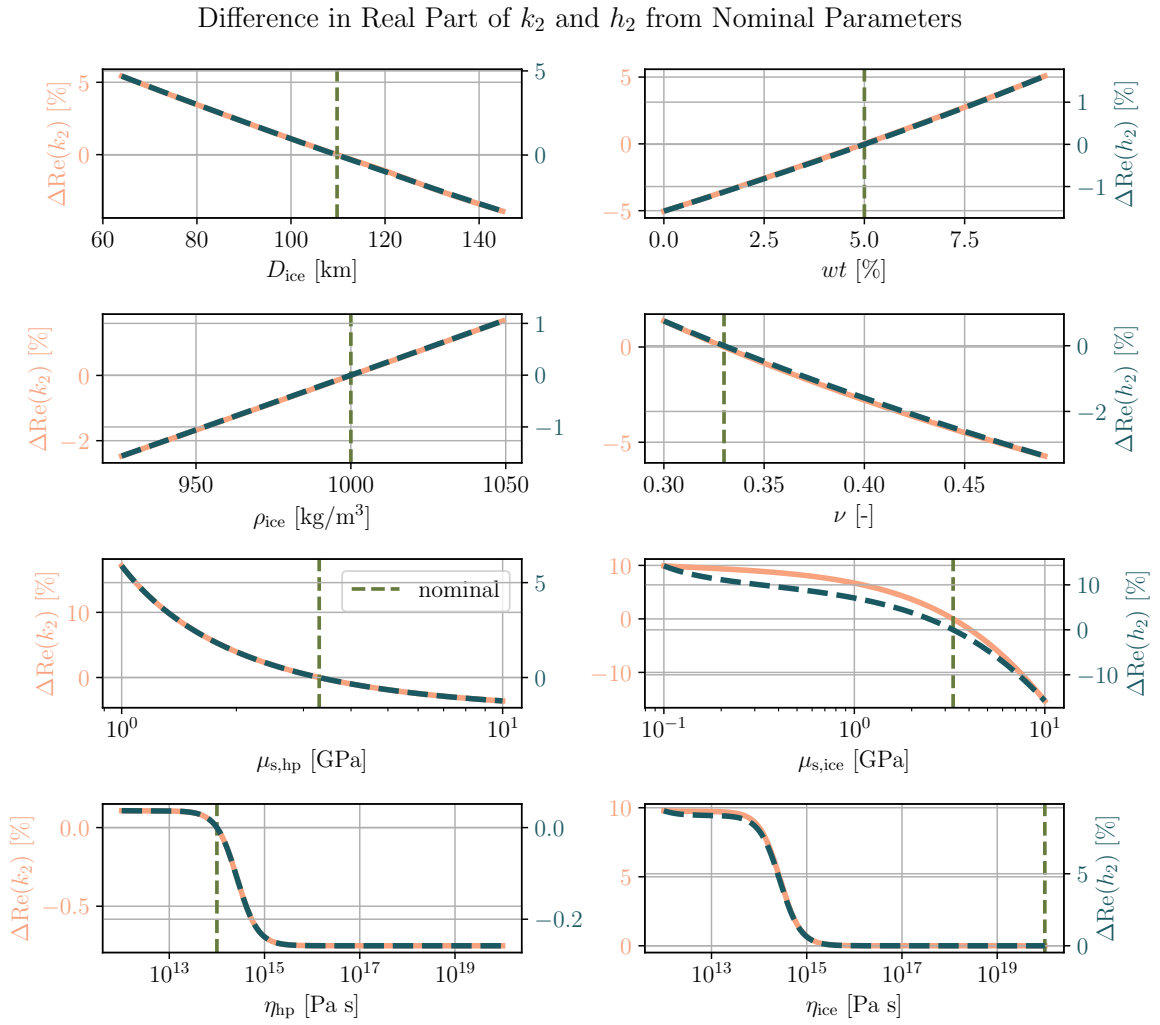

Figure D.8: Variation of the real part of the tidal response in percentage with respect to the nominal values, shown with a vertical dashed line. k_2 is plotted on the left y axis and h_2 on the right y axis, and the nominal values are $\text{Re}(k_2) = 0.5099$ and $\text{Re}(h_2) = 1.4122$.

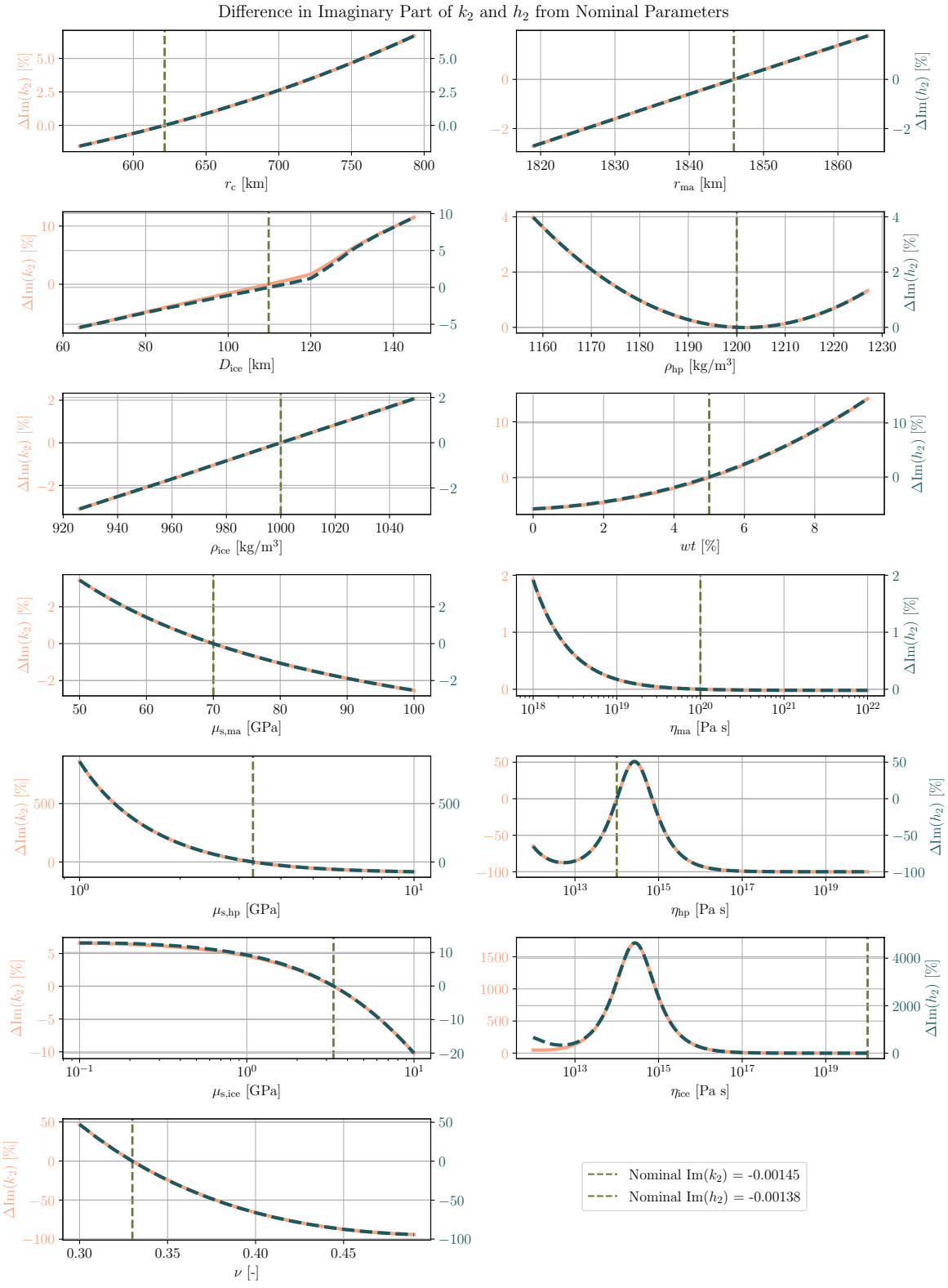

Figure D.9: Variation of the imaginary part of the tidal response in percentage with respect to the nominal values. k_2 is shown on the left y axis and h_2 on the right y axis.

Tidal Response

Figure D.8 and Figure D.9 show the variation of the real and imaginary part of the tidal response in percentage with respect to the response obtained with the nominal parameters. As shown in Figure D.8, both k_2 and h_2 decrease linearly with increasing ice shell thickness, since a thicker shell is more resistant to deformation (Jara-Orué et al., 2016; Van Hoolst et al., 2024). In contrast, higher ocean densities result in larger Love numbers (the effect of the ocean density can be observed through the effect of wt), which is consistent with the trends summarized in Van Hoolst et al. (2024, Figure 4) and the results of Kamata et al. (2016).

Similarly, the Love numbers decrease with increasing ice rigidity, as also reported by Jara-Orué et al. (2016) and Moore et al. (2003). This behavior can be explained by noting that higher shear moduli correspond to more rigid materials, which deform less easily and therefore exhibit smaller elastic responses. The trend of the real Love numbers with the ice viscosities shows the transition from fluid-like behavior at low viscosities to elastic behavior at high viscosities (Moore et al., 2003). Lastly, Figure D.8 and Figure D.9 show that k_2 and h_2 decrease with decreasing compressibility of the layers.

The imaginary components of the Love numbers, shown in Figure D.9, are related to the tidal dissipation within the moon and are therefore most sensitive to the mechanical properties of the outer ice layers. In particular, they depend strongly on viscosity, exhibiting a peak at a specific value. This behavior is well captured by the Maxwell rheological model, which defines a characteristic timescale, the Maxwell time. When the tidal forcing period approaches this timescale, energy dissipation reaches a maximum, which here occurs for viscosity values between 1×10^{14} and 1×10^{15} Pa s.

Libration Response

Figure D.10 shows the variation of the libration amplitude in percentage with respect to the nominal value of $|\Psi_{\text{ice}}| = 7.1480\,\text{m}$. The main contributor to the libration amplitude is the rigidity of the ice

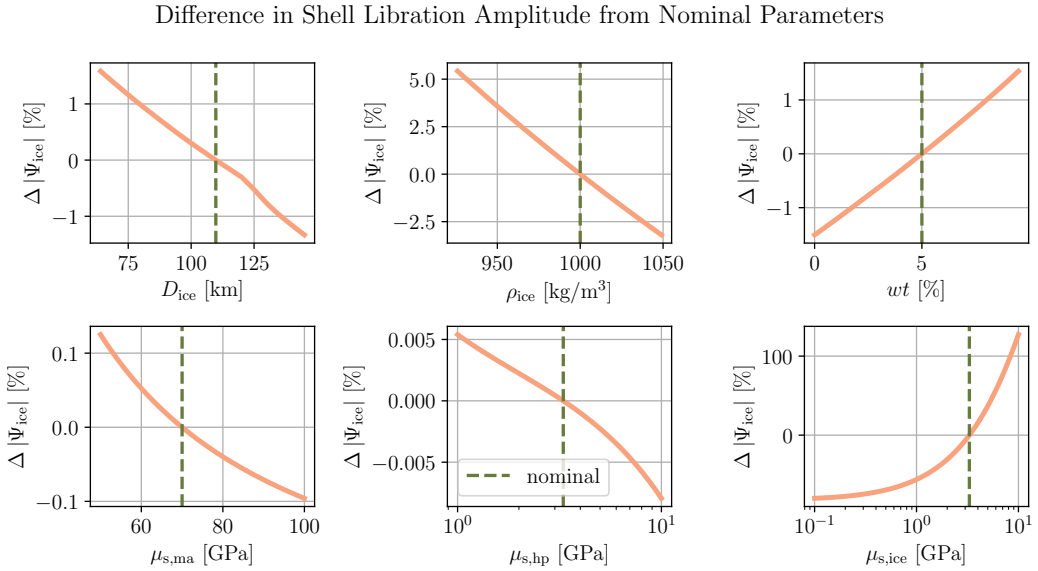

Figure D.10: Variation of the shell libration amplitude in percentage with respect to the nominal value of $|\Psi_{\text{ice}}| = 7.1480\,\text{m}$.

shell. For low rigidities, the ice behaves like a fluid and is more easily deformed, decreasing the libration amplitude, while highly rigid shells increase the libration (Van Hoolst et al., 2013). Additionally, the rigidities of the layers below the ocean have a minor effect on the libration amplitude, which is consistent with the findings of Van Hoolst et al. (2013). Another factor influencing the libration amplitude is the ice shell density: higher densities result in smaller amplitudes, as expected from Van Hoolst et al. (2013). Although the variation is limited to approximately $-2.5\,\%$ to $5\,\%$ relative to the nominal value, the ice shell density is here limited to a maximum of $1050\,\text{kg}\,\text{m}^{-3}$ due to imposed constraints.

Shell thickness also has a weak impact on the libration amplitude, with thinner shells leading to larger amplitudes, as shown by Van Hoolst et al. (2013). Finally, ocean composition has an effect of similar magnitude to that of shell thickness. The ocean composition directly affects the ocean's density, and Baland et al. (2010) showed how the libration amplitude depends on the density contrast between the ocean and the ice shell, which explains the observed trend.

D.2. Full Monte Carlo Analysis

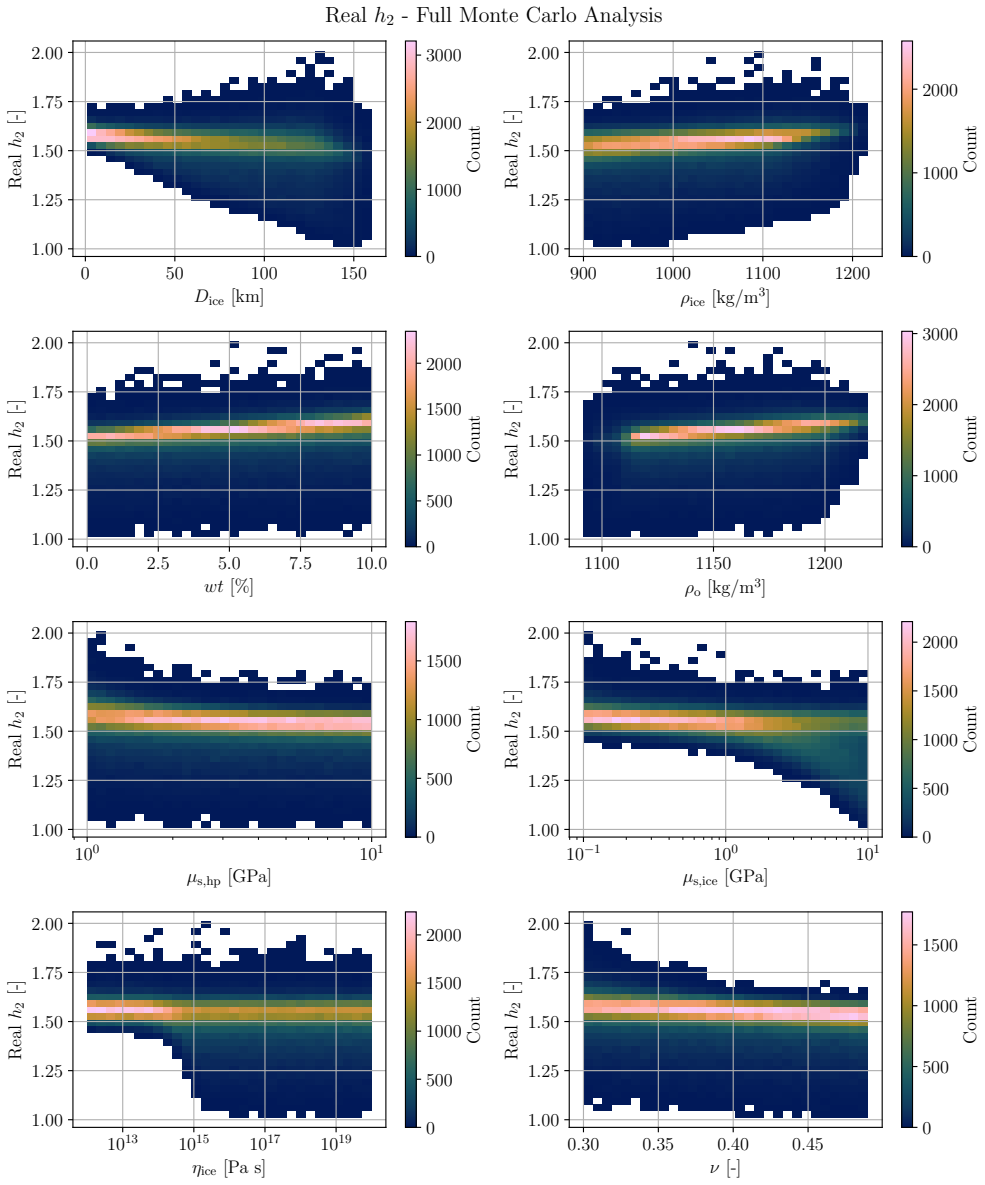

Figure D.11: Two-dimensional histogram of the real part of h_2.

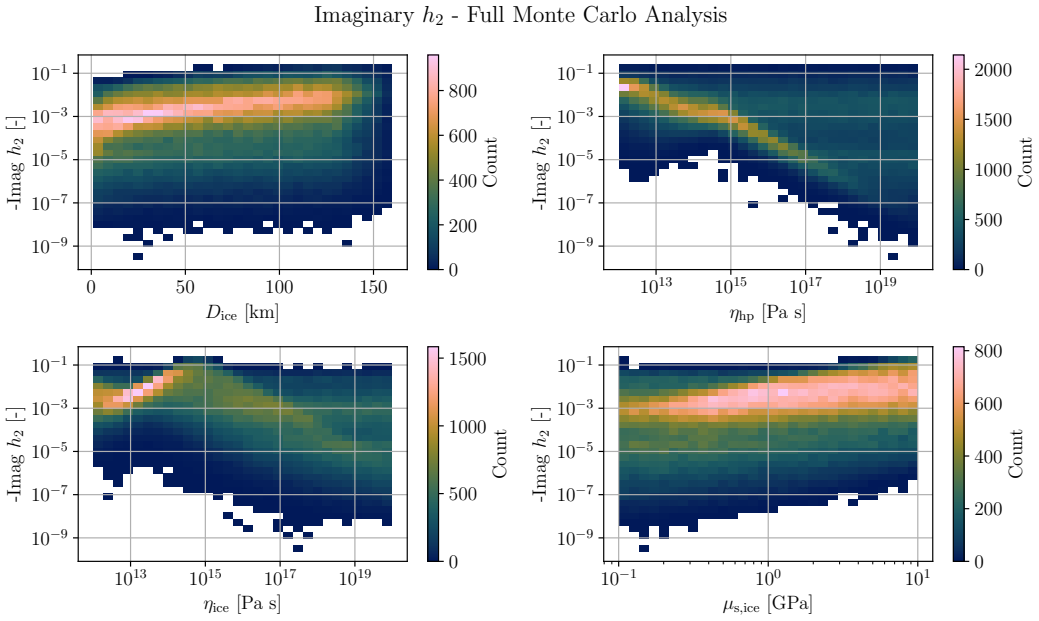

Figure D.12: Two-dimensional histogram of the imaginary part of h_2.

E

Bayesian Inversion

This chapter includes additional plots from the different Bayesian inversions performed, as well as a table summarizing all the obtained results.

E.1. Inversion with Static Gravity

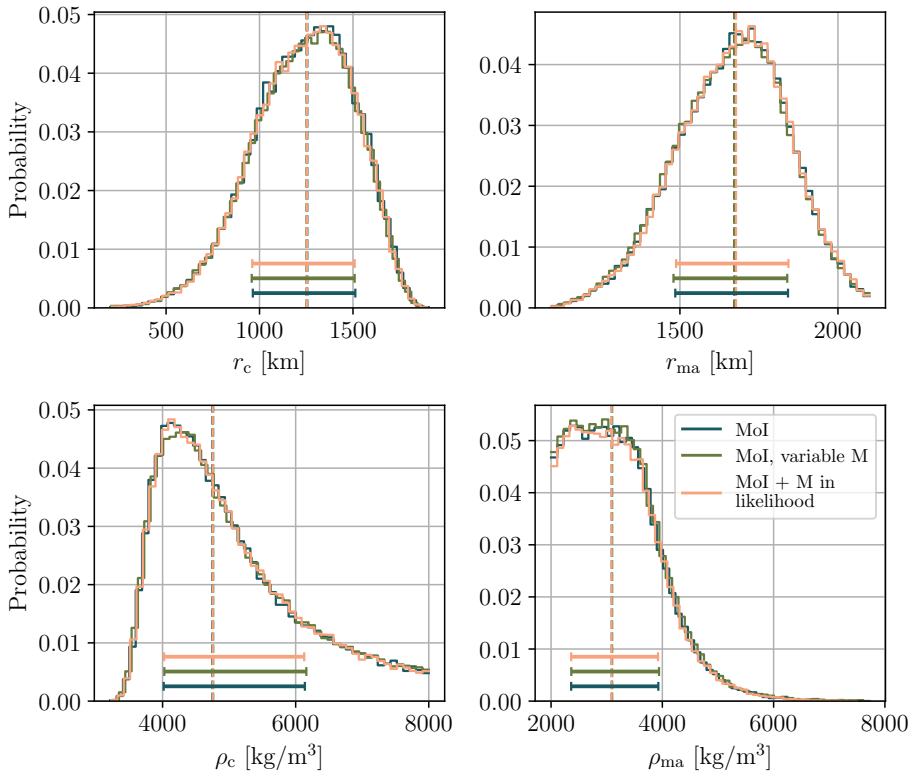

Figure E.1: Posterior probability distributions of the core and mantle radii and densities retrieved from three different inversions using Ganymede's moment of inertia as observation. The first inversion, labeled as "MoI" and corresponding to "Inversion 1", considers a fixed mass of Ganymede, $M_G = 1.481\,67 \times 10^{23}$ kg, and a fixed total radius, $R_G = 2631.2$ km. The second inversion, labeled as "MoI, variable M", allows the mass of Ganymede to vary within its uncertainty, $M_G \pm \sigma_M$, but does not include it in the likelihood function. The third inversion, labeled as "MoI + M in likelihood", allows both the mass and total radius of Ganymede to vary, and includes the mass in the likelihood function. The vertical dashed lines indicate the 50th percentile of the posterior distributions, while the horizontal bars show the 1-σ credible region.

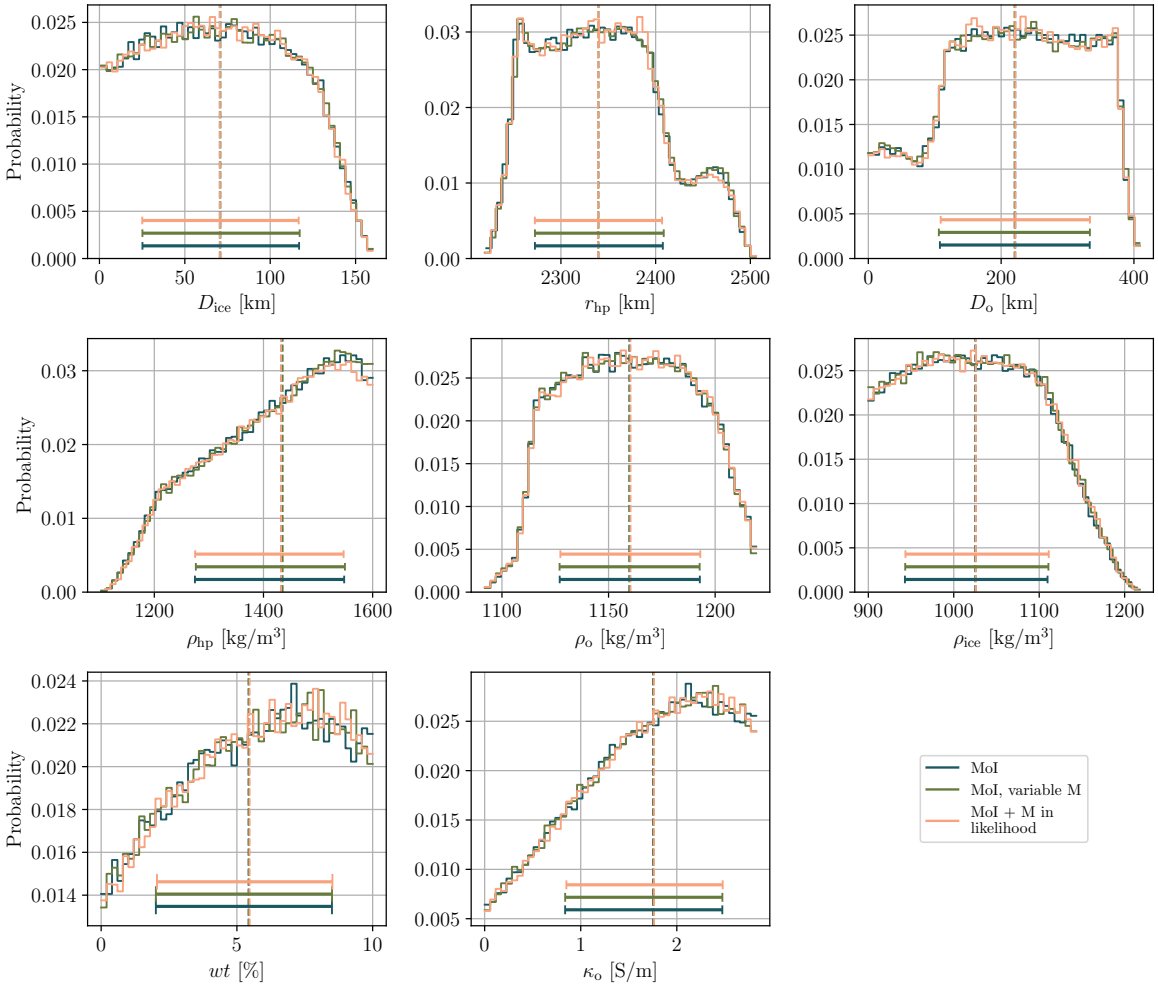

Figure E.2: Posterior probability distributions of the hydrosphere parameters retrieved from three different inversions using Ganymede's moment of inertia as observation. The three inversions are the same as described in Figure E.1. The vertical dashed lines indicate the 50th percentile of the posterior distributions, while the horizontal bars show the 1-σ credible region.

E.2. Inversion 2

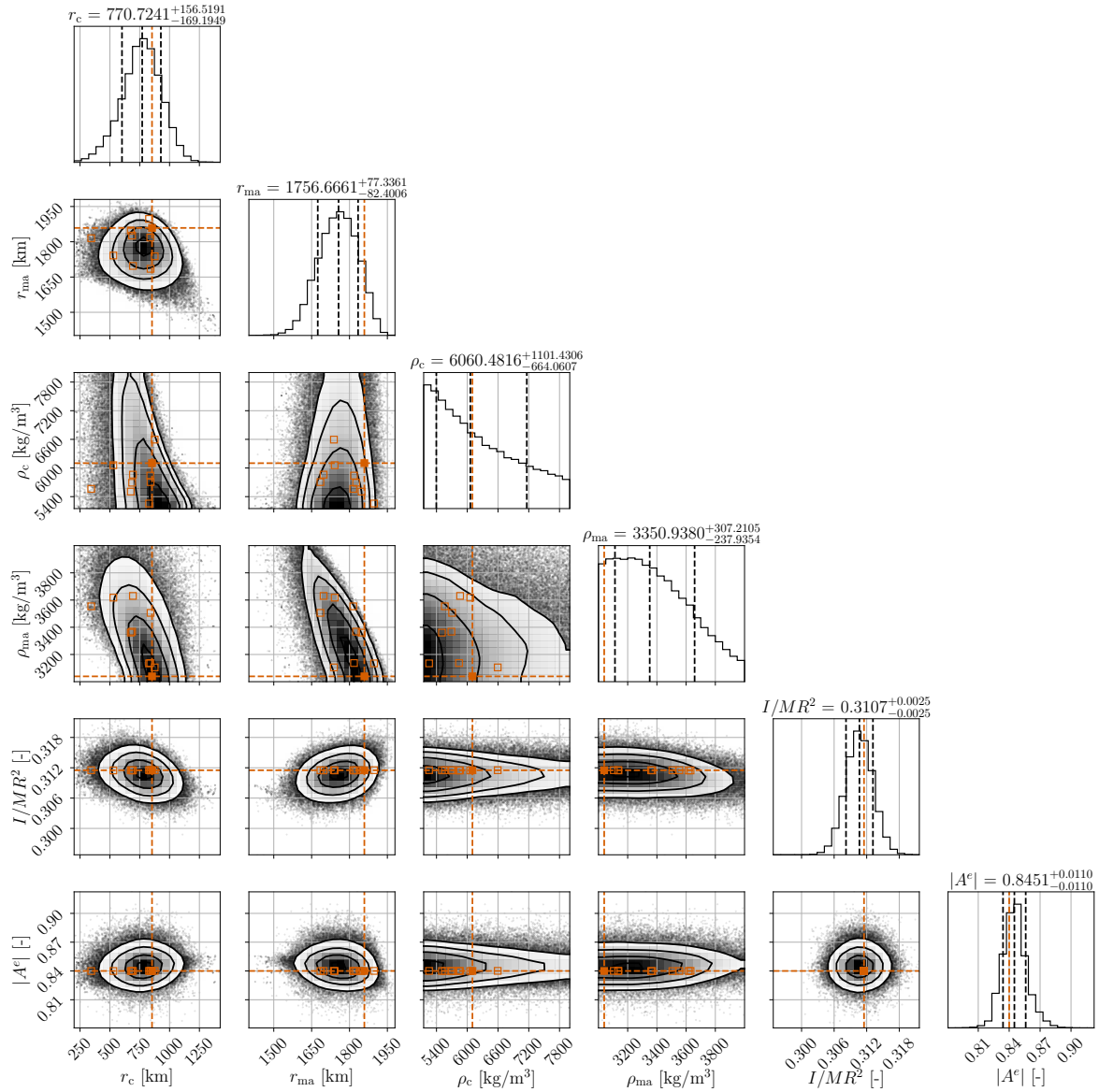

Figure E.3: Posterior probability distributions of the core and mantle radii and densities retrieved from "Inversion 2". The vertical dashed black lines indicate the 16th, 50th, and 84th percentiles. The full orange square and the orange dashed line indicate the parameters corresponding to the best-fitting sample, while the orange empty squares indicate the next nine best-fitting samples.

E.3. Inversion 3

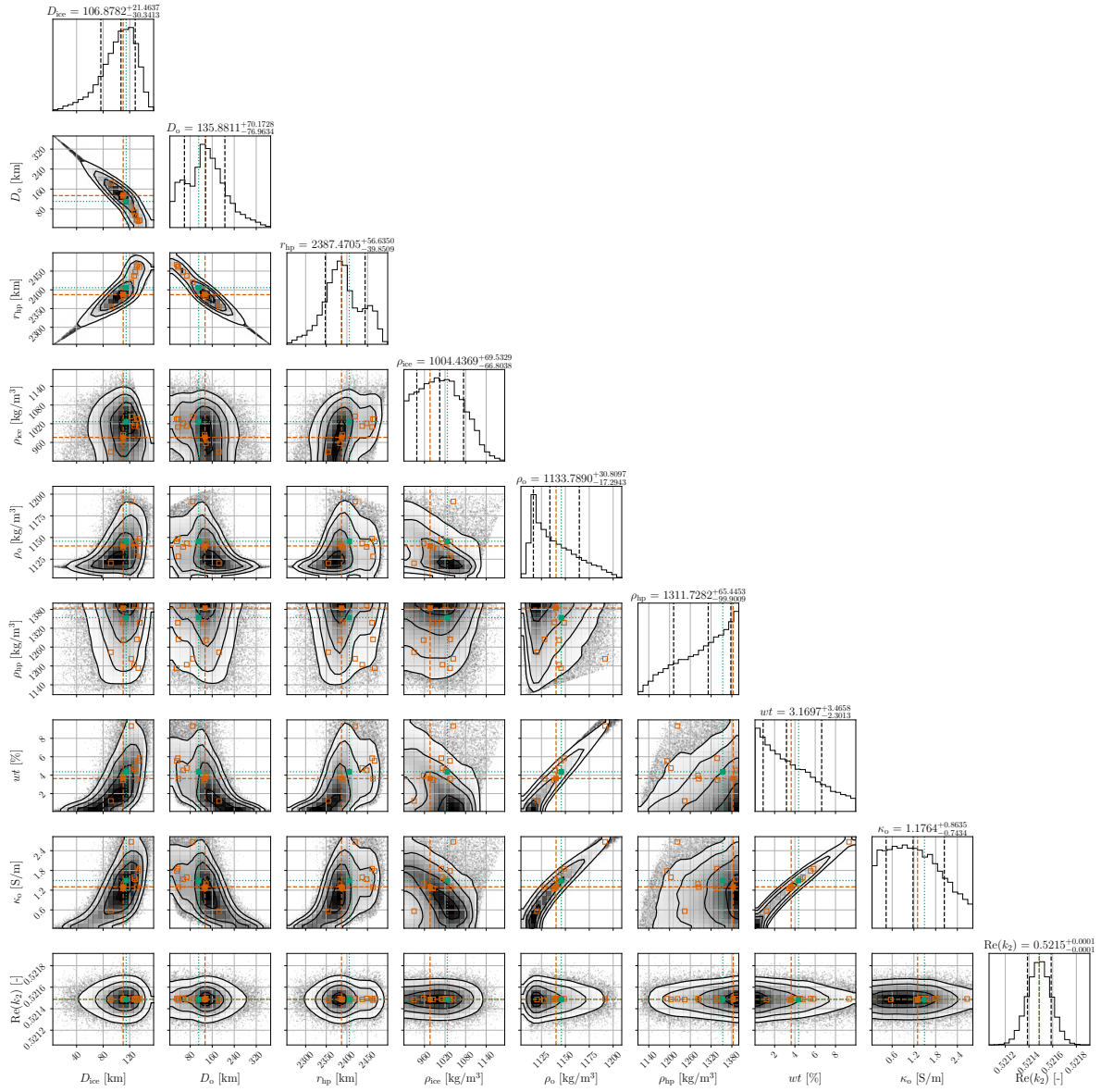

Figure E.4: Posterior probability distributions of the hydrosphere parameters retrieved from "Inversion 3". The vertical dashed black lines and the annotations above the subplots indicate the 16th, 50th, and 84th percentiles. The full orange squares and the orange dashed lines indicate the parameters corresponding to the best-fitting sample, while the orange empty squares indicate the next nine best-fitting samples. The full green squares and dotted lines indicate the true values of the parameters used to generate the synthetic data.

E.4. Inversion 4

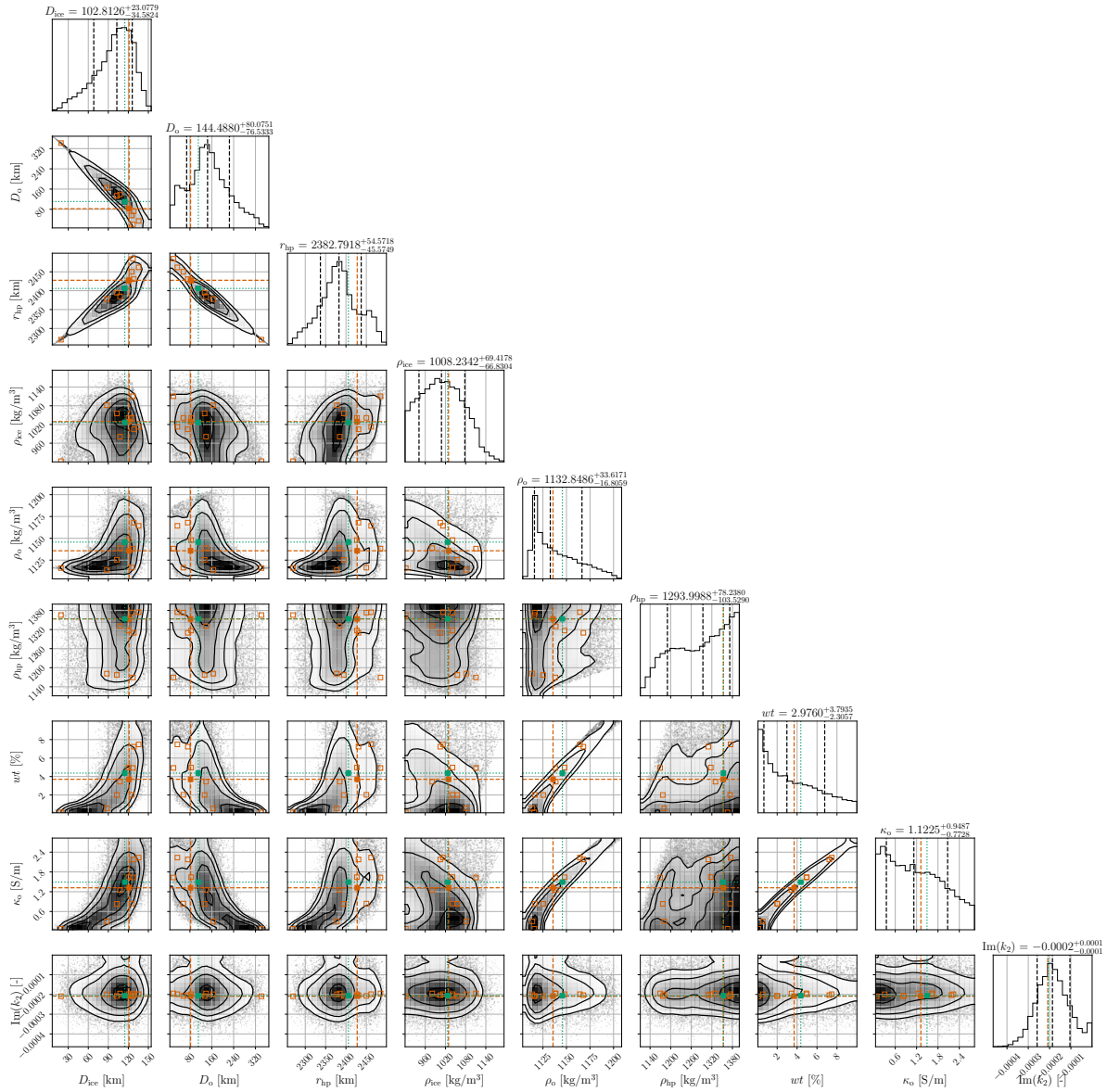

Figure E.5: Posterior probability distributions of the hydrosphere parameters retrieved from "Inversion 4". The vertical dashed black lines and the annotations above the subplots indicate the 16th, 50th, and 84th percentiles. The full orange squares and the orange dashed lines indicate the parameters corresponding to the best-fitting sample, while the orange empty squares indicate the next nine best-fitting samples. The full green squares and dotted lines indicate the true values of the parameters used to generate the synthetic data.

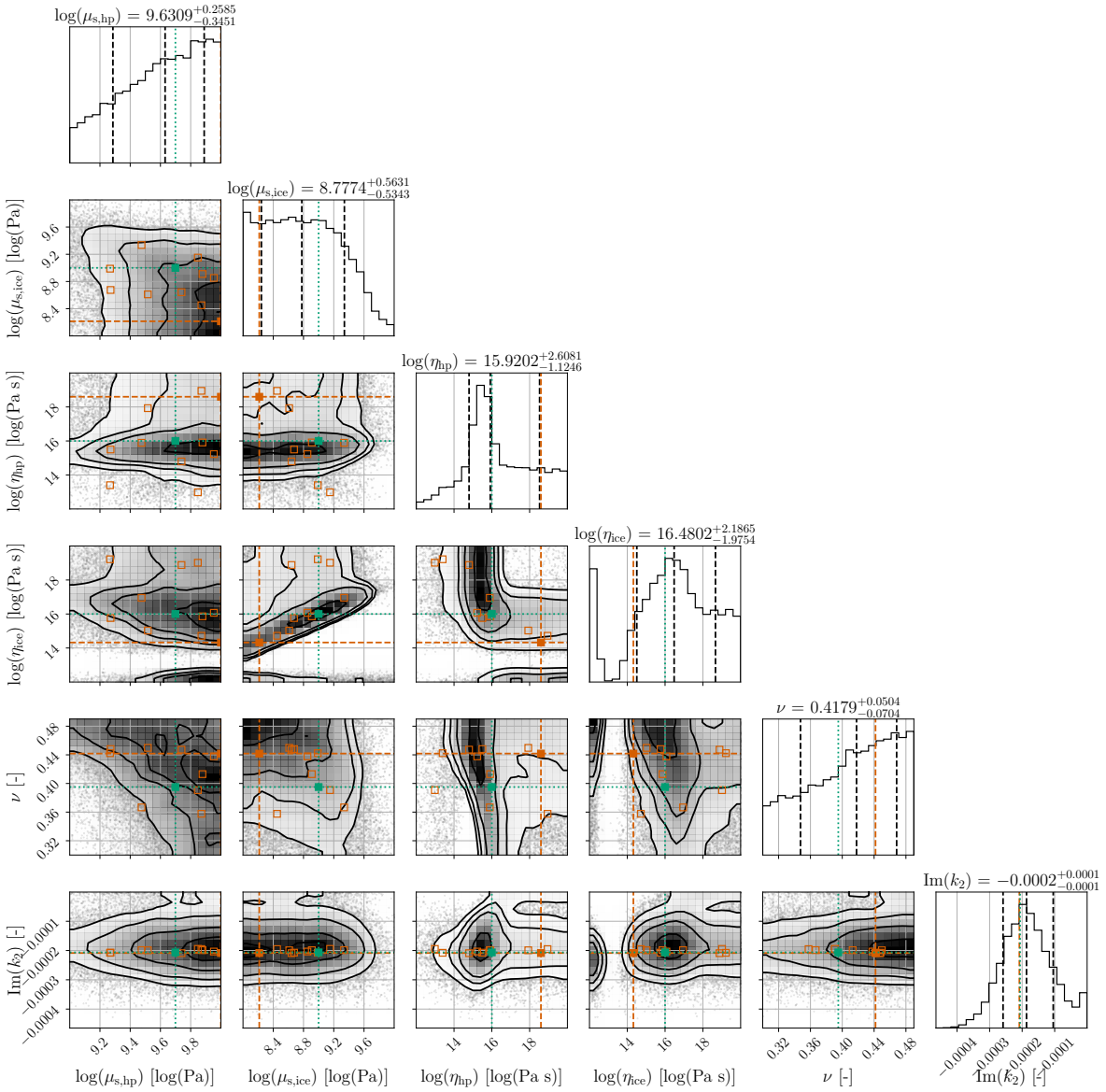

Figure E.6: Posterior probability distributions of the mechanical properties retrieved from "Inversion 4". The vertical dashed black lines and the annotations above the subplots indicate the 16th, 50th, and 84th percentiles. The full orange squares and the orange dashed lines indicate the parameters corresponding to the best-fitting sample, while the orange empty squares indicate the next nine best-fitting samples. The full green squares and dotted lines indicate the true values of the parameters used to generate the synthetic data.

E.5. Summary of the Inversion Results

Table E.1: Posterior estimates of the interior parameters retrieved from the different inversions, listed as the median value (50th percentile) with uncertainties corresponding to the 16th and 84th percentiles. Empty cells indicate that the corresponding parameter is not retrieved in that inversion. Results from additional inversions, mentioned in the main body and used to motivate choices or support the reasoning, are reported here below "Additional Inversions".

	Nominal Inversions				Additional Inversions		
Parameters	Inversion 1	Inversion 2	Inversion 3	Inversion 4	MoI, variable M	MoI + M in likelihood	MoI + induction, Undifferentiated
r_c [km]	$1255.59^{+256.89}_{-291.51}$	$770.73^{+156.52}_{-169.20}$	$753.69^{+159.84}_{-176.38}$	$746.75^{+154.15}_{-176.86}$	$1250.97^{+257.93}_{-292.81}$	$1253.30^{+255.72}_{-292.03}$	$1233.91^{+269.24}_{-277.84}$
r_{ma} [km]	$1676.17^{+165.83}_{-190.92}$	$1756.67^{+77.34}_{-82.40}$	$1775.60^{+73.60}_{-85.75}$	$1787.72^{+72.12}_{-87.69}$	$1671.48^{+168.09}_{-191.81}$	$1677.42^{+165.98}_{-189.59}$	$1656.52^{+188.46}_{-221.21}$
ρ_c [kg m^{-3}]	$4747.03^{+1391.51}_{-730.42}$	$6060.49^{+1101.42}_{-664.07}$	$6058.99^{+1127.86}_{-677.78}$	$6082.71^{+1115.26}_{-703.40}$	$4760.86^{+1400.14}_{-734.60}$	$4753.75^{+1375.21}_{-730.19}$	$4854.44^{+1495.71}_{-848.61}$
ρ_{ma} [kg m^{-3}]	$3091.09^{+836.68}_{-729.82}$	$3350.94^{+307.21}_{-237.94}$	$3323.68^{+311.14}_{-227.99}$	$3308.34^{+304.93}_{-216.52}$	$3097.90^{+842.80}_{-734.23}$	$3086.77^{+836.18}_{-724.91}$	$3119.20^{+910.85}_{-741.35}$
D_{ice} [km]	$70.48^{+46.43}_{-45.29}$	$110.47^{+17.21}_{-20.23}$	$106.88^{+21.46}_{-30.34}$	$102.81^{+23.08}_{-34.58}$	$70.88^{+46.39}_{-45.72}$	$70.55^{+46.12}_{-45.47}$	$110.30^{+18.16}_{-20.47}$
r_{hp} [km]	$2339.10^{+68.50}_{-66.54}$	$2398.92^{+51.32}_{-32.63}$	$2387.47^{+56.63}_{-39.85}$	$2382.79^{+54.57}_{-45.57}$	$2339.73^{+68.83}_{-67.14}$	$2339.10^{+67.70}_{-66.66}$	$2394.89^{+48.59}_{-31.13}$
r_o [km]	$2560.72^{+45.29}_{-46.43}$	$2520.73^{+20.23}_{-17.21}$	$2524.32^{+30.34}_{-21.46}$	$2528.39^{+34.58}_{-23.08}$	$2560.42^{+45.58}_{-46.59}$	$2560.64^{+45.54}_{-46.00}$	$2520.90^{+20.47}_{-18.16}$
ρ_{hp} [kg m^{-3}]	$1432.78^{+115.05}_{-158.35}$	$1315.34^{+59.65}_{-89.91}$	$1311.73^{+65.45}_{-99.90}$	$1294.00^{+78.24}_{-103.53}$	$1435.11^{+114.11}_{-159.05}$	$1432.18^{+114.65}_{-157.36}$	$1436.73^{+111.24}_{-160.48}$
ρ_o [kg m^{-3}]	$1159.77^{+33.05}_{-32.68}$	$1149.90^{+31.00}_{-27.43}$	$1133.79^{+30.81}_{-17.29}$	$1132.85^{+33.62}_{-16.81}$	$1159.88^{+32.85}_{-32.86}$	$1160.30^{+32.74}_{-32.89}$	$1148.19^{+31.80}_{-26.45}$
ρ_{ice} [kg m^{-3}]	$1025.21^{+84.56}_{-82.37}$	$1031.11^{+74.01}_{-79.12}$	$1004.44^{+69.53}_{-66.80}$	$1008.23^{+69.42}_{-66.83}$	$1025.63^{+85.17}_{-82.47}$	$1025.91^{+85.30}_{-82.48}$	$1013.72^{+78.12}_{-72.44}$
wt [%]	$5.43^{+3.07}_{-3.42}$	$5.02^{+3.25}_{-3.17}$	$3.17^{+3.47}_{-2.30}$	$2.98^{+3.79}_{-2.31}$	$5.43^{+3.07}_{-3.42}$	$5.47^{+3.05}_{-3.41}$	$4.81^{+3.33}_{-3.10}$
κ_o [S m^{-1}]	$1.75^{+0.72}_{-0.92}$	$1.65^{+0.77}_{-0.87}$	$1.18^{+0.86}_{-0.74}$	$1.12^{+0.95}_{-0.77}$	$1.75^{+0.72}_{-0.92}$	$1.76^{+0.71}_{-0.91}$	$1.60^{+0.79}_{-0.86}$
$\log(\mu_{s,hp})$ [log(Pa)]			$9.63^{+0.26}_{-0.35}$	$9.63^{+0.26}_{-0.35}$			
$\log(\mu_{s,ice})$ [log(Pa)]			$8.91^{+0.58}_{-0.60}$	$8.78^{+0.56}_{-0.53}$			
$\log(\eta_{hp})$ [log(Pa s)]				$15.92^{+2.61}_{-1.12}$			
$\log(\eta_{ice})$ [log(Pa s)]			$15.94^{+2.76}_{-2.59}$	$16.48^{+2.19}_{-1.98}$			
υ [-]			$0.42^{+0.05}_{-0.07}$	$0.42^{+0.05}_{-0.07}$			